Cracow University of Technology

Faculty of Civil Engineering

Doctoral Thesis

NUMERICAL MODELING OF CHEMO-HYDRO-MECHANICAL INTERACTION IN COHESIVE-FRICTIONAL MATERIALS

Modelowanie numeryczne chemo-hydro-mechanicznej interakcji w materiałach
z tarciem i kohezją

Author:

Piotr Przecherski, MSc

Supervisors:

Stanisław Pietruszczak, Prof.

Teresa Stryszewska, Prof. CUT

Cracow, 2023

NUMERICAL MODELING OF CHEMO-HYDRO-MECHANICAL INTERACTION IN COHESIVE-FRICTIONAL MATERIALS

By PIOTR PRZECHERSKI, B.Eng., M.Sc.

A Thesis
Submitted to the School of Graduate Studies
in Partial Fulfilment of the Requirements
for the Degree of
Doctor of Philosophy
in Civil Engineering

Cracow University of Technology

Abstract

This Ph.D. thesis is concerned with modeling the chemo-hydro-mechanical behavior of different types of geomaterials, including both natural and engineered materials used in construction. It addresses two significant issues related to specification of failure criteria, i.e. inherent anisotropy and degradation of properties caused by environmental damage. The research also examines the hydro-mechanical behavior in the presence of self-sealing and self-healing fractures. The main objective is to enhance our understanding of the mechanical response of structured geomaterials including multi-phase interactions (water-skeleton) and the evolution of strength and deformation properties. The study focuses on a class of inelastic quasi-brittle geomaterials, such as sedimentary and crystalline rocks, as well as components of structural masonry.

Inherent anisotropy in the microstructure is examined using a rock formation from the Carpathian Flysch Belt. The aim is to establish a continuum-based plasticity framework that incorporates an anisotropic failure criterion. This criterion employs the notion of a microstructure tensor and considers the directional dependence of properties as well as the volume fraction of constituents. The procedure for identification of material parameters/functions is based on mesoscale simulations conducted on a representative elementary volume.

Furthermore, the research investigates the chemo-hydro-mechanical interaction in fractured crystalline rocks, with a particular emphasis on studying the processes of self-sealing and self-healing of fractures. The work involves developing a general mathematical framework for describing the chemo-mechanical interaction. The approach utilizes a constitutive relation with embedded discontinuity, incorporating an internal scale parameter that affects both hydraulic and mechanical properties.

In addition, the research is focused on specification of conditions at failure and examining the time-dependent evolution of strength parameters in construction materials that experience environmental damage due to salt crystallization. The study involves a comprehensive experimental as well as numerical component. The evolution laws are expressed in terms of the degree of pore saturation with precipitated salt, which is subsequently employed in the development of governing constitutive equations that couple the mechanical response with salt crystallization phenomenon.

Overall, this thesis encompasses a broad and interdisciplinary scope, addressing anisotropy, presence of discontinuities, fracture sealing and healing, and degradation of properties caused by salt deposition in pores. The research findings have applications in various areas of Civil and Environmental Engineering.

Streszczenie

Przedstawiona praca doktorska dotyczy opisu zachowania chemo-hydro-mechanicznego szerokiej klasy geomateriałów, zarówno występujących naturalnie, jak i stosowanych w budownictwie. Porusza ona głównie dwie istotne kwestie związane ze sformułowaniem kryteriów zniszczenia, tzn. anizotropie wytrzymałości materiału oraz degradacje właściwości mechanicznych spowodowaną czynnikami środowiskowymi. Przedstawione rozważania zawierają również opis zachowania hydromechanicznego materiałów spękanych podlegających procesowi samouszczelnienia oraz samoleczenia. Głównym celem pracy jest rozszerzenie wiedzy na temat zachowania geomateriałów z wewnętrzna struktura, uwzględniając interakcje wielofazowe (woda-szkielet) oraz ewolucje właściwości wytrzymałościowych. Badania te koncentrują się na klasie materiałów niesprężystych quasi-kruchych, takich jak skały krystaliczne i osadowe, a także elementy konstrukcji murowych.

Naturalnie występująca anizotropia jest opisana na przykładzie fliszu karpackiego. Głównym celem jest tu sformułowanie makroskopowe w ramach teorii plastyczności, które wykorzystuje anizotropowe kryterium zniszczenia. Kryterium to jest oparte na pojęciu tensora mikrostruktury i uwzględnia kierunkową zależność właściwości oraz udział objętościowy składników. Procedura identyfikacji parametrów/funkcji materiału opiera się na symulacjach w skali mezo przeprowadzonych dla reprezentatywnej elementarnej objętości.

Ponadto badania dotyczą opisu chemo-hydro-mechanicznego zachowania spękanych skał krystalicznych, ze szczególnym naciskiem na badanie procesów samouszczelniania i samoleczenia pęknięć. Badania obejmują opracowanie modeli matematycznych uwzgledniających interakcje chemiczno-mechaniczna. Podejście to wykorzystuje związek konstytutywny z wbudowaną nieciągłością, który zawiera wewnętrzny parametr skali wpływający zarówno na właściwości hydrauliczne, jak i mechaniczne.

Badania również koncentrują się na określeniu warunków zniszczenia oraz zależnej od czasu ewolucji parametrów wytrzymałościowych w materiałach budowlanych, które poddane są degradacji środowiskowej związanej z krystalizacja soli. Badanie obejmuje kompleksową część eksperymentalną i numeryczną. Prawa ewolucji wyrażone są w funkcji stopnia nasycenia porów wytrąconą solą. Ten sam parametr jest następnie wykorzystywany do opracowania równań konstytutywnych łączących odpowiedź mechaniczną ze zjawiskiem krystalizacji soli.

Przedstawiona praca ma szeroki i interdyscyplinarny zakres, jako że uwzględnia anizotropie, obecność nieciągłości, uszczelnianie i leczenie spękań oraz degradacje właściwości spowodowaną akumulacja soli w porach. Wyniki badań mają zastosowanie w różnych obszarach Inżynierii Lądowej i Inżynierii Środowiska.

Acknowledgements

I would like to express my special appreciation and thanks to my doctoral advisor Professor Stanislaw Pietruszczak. You have been a tremendous mentor for me, and I thank you for your encouragement and countless support over the years. Your advice on both research as well as on my professional carrier has been priceless. Words cannot express how grateful I am for the help that I received in all my pursuits.

I would like to express my sincere gratitude to my doctoral advisor Teresa Stryszewska, prof. CUT. I'm grateful for her support of my PhD study, as well as for sharing her time and technical expertise at various stages of this research.

I would also like to express my sincere gratitude to Dr. Antoni Bojarski for his continuing support throughout my university carrier. His faith in my potential has given me the strength to persevere during challenging times and strive for excellence.

Lastly, I want to take this opportunity to acknowledge and appreciate the constant support of my family and friends. Their love, encouragement, and understanding have been the bedrock of my success throughout this demanding undertaking.

Thesis format

This thesis has the format of an integrated article-based dissertation and includes three journal papers that form separate chapters containing the main contributions in this study. The papers are as follows:

1. *Przecherski P, Pietruszczak S (2020). On specification of conditions at failure in interbedded sedimentary rock mass. Acta Geotech. 15: 365–374. https://doi.org/10.1007/s11440-019-00794-x*
2. *Pietruszczak S, Przecherski P (2021). On hydro-mechanical response of self-healing and self-sealing fractured geomaterials. Computers and Geotechnics. 134:104030. https://doi.org/10.1016/j.compgeo.2021.104030*
3. *Pietruszczak S, Przecherski P, Stryszewska T (2022). Impact of salt crystallization on the mechanical properties of structural masonry: An experimental and numerical study. Construction and Building Materials. 344: 128062. https://doi.org/10.1016/j.conbuildmat.2022.128062*

Co-Authorship

Based on the guidelines for an integrated article dissertation, the details of cooperation between authors of each paper are presented below. Authors' declaration confirming this statement is provided in the Appendix.

Article #1: On specification of conditions at failure in interbedded sedimentary rock mass (P. Przecherski and S. Pietruszczak)

Prof. S. Pietruszczak together with P. Przecherski developed a continuum-based framework for Carpathian flysch that incorporates an anisotropic failure criterion and considers the influence of the volume fraction of constituents. P. Przecherski incorporated this framework in an FE code and conducted, in consultation with Prof. S. Pietruszczak, a series of mesoscale simulations. A comprehensive set of 'virtual data' generated through this investigation has been employed to identify material functions appearing in the continuum framework. The latter was verified against a broad range of virtual data by P. Przecherski. The paper was drafted by Prof. S. Pietruszczak, reviewed and amended by P. Przecherski, and finalized by Prof. S. Pietruszczak.

Article #2: On hydro-mechanical response of self-healing and self-sealing fractured geomaterials (S. Pietruszczak and P. Przecherski)

Mathematical framework for describing the mechanical and hydraulic properties of fractured geomaterials undergoing self-healing (i.e. recovery of strength/stiffness) and self-sealing (i.e. reduction of permeability) was developed by Prof. S. Pietruszczak with an active engagement of P. Przecherski. Numerical examples involving the analysis of a discrete fracture network undergoing a transient flow under self-sealing conditions, as well as inelastic simulations for a specimen with pre-existing fractures undergoing a self-healing have been conducted by P. Przecherski. The paper was drafted by Prof. S. Pietruszczak, reviewed and amended by P. Przecherski, and finalized by Prof. S. Pietruszczak.

Article #3: Impact of salt crystallization on the mechanical properties of structural masonry: an experimental and numerical study (S. Pietruszczak, P. Przecherski and T. Stryszewska)

Experimental investigation and interpretation of the results on the variation of mechanical properties of primary constituents of structural masonry during the process of salt crystallization were performed by P. Przecherski. The microstructural imaging and porosity measurements of constituents were conducted by Prof. T. Stryszewska. The evolution laws embedded in specification of the conditions at failure were proposed by Prof. S. Pietruszczak and P. Przecherski, while the elastoplastic rate-dependent constitutive relations were developed by Prof. S. Pietruszczak. A draft of the paper was prepared by Prof. S. Pietruszczak. It was subsequently revised by P. Przecherski and finalized by Prof. S. Pietruszczak.

Table of contents

List of Figures

Chapter 2

Chapter 3

Chapter 4

Fig. 15. Evolution of free expansion with the number of contamination cycles; (a) individual components, (b) the volume change.

Fig. 16. (a) Average stress-strain characteristics for mortar subjected to uniaxial compression; (b) evolution of strength during the exposure to contamination.

Fig. 17. (a) Average stress-strain characteristics for mortar under axial tension; (b) evolution of tensile strength during the exposure to contamination.

Fig. 18. Average stress-strain characteristics for mortar in ‘triaxial’ tests.

Fig. 19. Failure envelopes for mortar (a) in the referential state and (b) after exposure to magnesium sulphate contamination.

Fig. 20. Variation of friction angle and cohesion with the number of contamination cycles.

Fig. 21. Results of direct shear tests on brick-mortar bond; shear stress – displacement characteristics; (a) at no confinement, (b) at σ=-0.55 MPa.

Fig. 22. Variation of friction angle and cohesion for brick-mortar bond with the number of contamination cycles.

Fig. 23. (a) Average tensile stress-strain characteristics for brick-mortar bond; (b) variation of tensile strength with the number of contamination cycles.

Fig. 24. Failure envelopes for brick-mortar bond (a) in the referential state and (b) after exposure to magnesium sulphate contamination.

Fig. 25. Simulations of axial compression tests at different stages of the exposure to contamination.

Fig. 26. Evolution of strength parameters with volume fraction of precipitated salt; quadratic approximation based on eq.(3).

Fig. 27. (a) Build up of axial strain with increase in salt contamination at a constant axial load of q=10, 15 and 20 MPa; (b) the corresponding evolution of the yield/ failure surfaces at axial load of 15 MPa.

List of Tables

Chapter 3

Chapter 4

Chapter 1

Introduction

This Ph.D. thesis deals with various aspects of modeling the chemo-hydro-mechanical response of geomaterials, both naturally occurring and those used in the construction industry. The considered materials may all be perceived as *cohesive-frictional*; their strength in compression regime is pressure dependent and is higher than that in tensile range. The research reported here addresses two important issues related to specification of conditions at failure, which include the case of inherent anisotropy and also the presence of degradation of properties triggered by environmental damage. In addition, the work also involves a description of chemo-hydro-mechanical interaction in the presence of self-sealing and self-healing fractures. Although the scope may appear to be somewhat diverse, the main motivation is to focus on a class of problems that are conceptually challenging and, at the same time, are of importance for safety assessment of various engineering structures, including those of strategic significance. The thesis is prepared in an integrated-article format and includes three papers, published in established international journals, in support of developing the current approach. In what follows, the motivation behind this research is provided followed by some general comments on the scope of this work.

1.1 Motivation and background

The main motivation behind the current research is to enhance our understanding of the mechanical behavior of structured geomaterials in relation to multi-phase (i.e. water - skeleton) interaction and evolution of strength/deformation properties. The research deals with a class of inelastic quasi-brittle materials; both naturally occurring (i.e., rocks) and man-made (i.e. components of structural masonry). The primary objective is the development and verification of mathematical frameworks for describing their mechanical response in dry as well as water saturated state. There are three basic aspects of the problem that will be addressed. They include the notion of structural anisotropy (sedimentary rocks), the evolution of hydro-mechanical properties in the presence of discrete fracture networks (crystalline rocks), as well as degradation of strength properties in construction materials (structural masonry) triggered by environmental effects associated with subflorescence of salts (i.e., crystallization within the pores).

The *sedimentary* rocks, such as claystone, siltstone, limestone, shale, etc., are inherently anisotropic and often heterogeneous [1, 2]. Anisotropy is due to stratification resulting from the sedimentation process, while heterogeneity originates from different mineral composition of fabric [3]. Over the last decades, a significant amount of research has been conducted on the evaluation of mechanical and hydraulic properties of sedimentary formations. The work involved a range of experimental tests, which included unconfined compression, triaxial and hollow cylinder compression, splitting tension, as well as hydraulic tests to estimate the permeability (cf. [4, 5]). Numerous references on the existing experimental data can be found in various published articles (e.g. [6, 7]); however, given the volume of data, a comprehensive review on this topic is difficult. The main conclusions deal with assessment of sensitivity of the failure mechanism, and the associated strength, to the orientation of the sample. In this regard, the failure mode in shales, for example, involves formation of macrocracks which are oriented either along the bedding planes or penetrate through the argillaceous matrix (cf. [8]). The minimum value of compressive strength is typically associated with sample orientations within the range of 30^0-60^0 and the strength reduction is of the order of 50%. The increase in confining pressure results in the corresponding increase in strength but, at the same time, the effects of anisotropy become less pronounced. Similar conclusions were reported in ref. [9] where the authors examined three types of rocks with distinct foliation, including shale, gneiss and schist. In general, most sedimentary rocks are considered as transversely isotropic with the preferred direction normal to bedding planes. However, as mentioned earlier, certain types of sedimentary rocks have a strongly inhomogeneous fabric (cf. [4], [10]). In this case, the experimental results display a significant scatter as well as an apparent size effect. This is mainly due to different volume fraction of constituents, e.g. argillaceous inclusions, in individual samples tested. For this reason, the quantification of anisotropy, in terms of directional dependence of strength and stiffness properties, is difficult and the conclusions emerging from different experimental programs are often conflicting.

In parallel with experimental work, a significant amount of research on sedimentary rock formations has focused on formulation of general failure criteria. Since the classical isotropic criteria are not adequate here, different methodologies have been employed to deal with the notion of anisotropy. A comprehensive review on this topic is provided in refs. [11, 12]. One of the first attempts, dating back to 1960s, was a criterion based on assessing the conditions at failure along a set of pre-existing weakness planes [13, 14]. Later, more general framework were introduced in ref. [15, 16] based on an extension of Hill's criterion. Apparently, the most rigorous approach is that based on the representation theorems for tensor-valued functions, which incorporates ten independent invariants of both the stress and a fabric tensor [17]. The latter approach, however, leads to a large number of material functions and parameters that cannot be uniquely identified. Other approaches for assessing the conditions at failure in sedimentary rocks employed discrete element methodology ([18], [19], [20]). In this case, the rock is represented by a dense packing of nonuniform circular or spherical particles that are bonded together at their contact points. Such an approach raises several concerns. First, the framework requires information on the contact properties that cannot be directly determined from any experimental tests. Also, the idealization of rock samples as an assemblage of bonded spherical particles, is not very realistic. Thus, the quantitative aspects may be seriously questioned.

In this thesis, the issue of inherent anisotropy in microstructure is addressed in the context of a rock formation that is representative of Carpathian Flysch Belt. The latter has a sequence of alternating deposits of claystone and sandstone with varying thickness. The objective is to derive a continuum-based plasticity framework that incorporates an anisotropic failure criterion. The latter is developed using the notion of a microstructure tensor (cf. [21]) and accounts not only for the effects of directional dependence of properties but also for the influence of volume fraction of constituents. The proposed methodology involves mesoscale simulations, the results of which allow the assessment of strength properties for different orientations of stratification relative to direction of loading. A comprehensive set of ‘virtual data’ generated through this investigation is then employed to identify material functions appearing in the continuum framework. This is a pragmatic approach that is particularly advantageous in the context of analysis of large-scale geotechnical problems that involve this type of rock formation.

The second major topic deals with *crystalline* igneous rock formations (e.g., granite, gabbro, rock salt). In general, the *intact* crystalline rocks are isotropic at the macroscale and there is no evidence of directional dependence of their properties. At the same time, however, the crystalline rock mass is known to contain multiple naturally occurring faults/macro fractures, which impact the hydromechanical properties. The majority of research in this area has been focused on granite and involved mainly the experimental component dealing with the evaluation of mechanical and hydraulic properties. The work comprised a range of standard material tests, which included unconfined axial compression, Brazilian splitting tests as well as triaxial compression (e.g., [22], [23], [24]). The experimental evidence in relation to *triaxial* tests shows that the behaviour under higher confinement is plastic-brittle and the post-peak response is often associated with a snap-back instability. The results also indicate that the failure envelopes are non-linear in the meridional sections. Thus, at higher confining pressures the linear approximation, based on Mohr-Coulomb criterion, is not accurate. This conclusion is evident from the data reported by several investigators (e.g., [25], [23]). In addition to the above-mentioned studies, some limited investigations on long-term evolution of strength [26], as well as the strain-rate sensitivity [27] have been conducted. Also, the issues related to identification of microcracks in multi-phase crystalline matrix, using X-ray CT imaging, have been addressed [28]. In general, at low confining pressures, the micro-fracturing initiates at 40%-60% of uniaxial compressive strength and as the load intensity increases, the microcracks start to coalesce which leads to strain localization [29].

In terms of modeling of mechanical response, both continuum and discrete approaches have been employed. The former commonly involve plasticity or damage-plasticity frameworks for isotropic geomaterials [30, 31]. The latter, i.e. discrete approaches, make use of a discrete element technique to generate deformable polygonal grain-like structure to simulate the rock fabric (cf. [32]). In relation to hydraulic properties, there were a few attempts to assess the damage-induced permeability variation using micromechanical approach (e.g., [33]). However, there have been no systematic studies on the assessment of average hydraulic conductivity within a domain containing low density discrete fractures. In general, the flow through a fractured rock mass is affected by the geometry of fracture network, i,e, orientation and spacing of individual fractures and their connectivity. These factors must be considered in assessing the hydraulic properties at the macroscale. The numerical analysis of flow is typically conducted by employing the Extended Finite Element Method (XFEM) (e.g., [34]). Although this approach is accurate, it is computationally very inefficient. The latter stems from incorporation of additional degrees of freedom that account for the presence of discontinuities, as well the need for partitioning of the domain with triangular sub-elements for the numerical integration. In addition to XFEM, other simplified methodologies have been used, which involve Oda's concept of permeability tensor [35, 36] as well as the so-called pipe network models [37, 38].

In this thesis, the chemo-hydro-mechanical interaction in fractured crystalline rocks is addressed in the context of an ongoing self-sealing and self-healing processes. The occurrence of these processes is of a particular importance in a class of materials that are being considered for use as storage repositories for radioactive waste, compressed gasses, crude oil, etc. The intrinsic self-healing mechanisms are typical of cementitious materials and are attributed to ongoing hydration of cement particles, as well as precipitation of calcium carbonate inside the cracks [39, 40, 41]. Similar effects are also present in various rock formations. For rock salt, for example, the experimental evidence indicates that nearly 80% of original strength can be regained through a mechanism which involves pressure induced creep of asperities along the fracture surface leading to formation of an interlocking network [42]. In terms of *self-sealing*, there is a considerable evidence that most fluid-conductive rock fractures will, with the passage of time, seal [43, 44]. The process occurs at different rates which depend on the site-specific conditions such as the type of rock minerals, degree of induration and chemistry of the porewater. In general, however, over a time span of one year, the permeability is typically reduced to 10^{-2} of its initial value. The work reported in this thesis involves development of a general mathematical framework for the description of crack sealing/healing processes. The approach employs a constitutive relation with embedded discontinuity which incorporates an internal scale parameter that affects both the hydraulic and mechanical properties [45]. Numerical examples are provided involving numerical analysis of a discrete fracture network undergoing a transient flow under self-sealing conditions, as well as an inelastic simulations of a specimen with pre-existing fractures undergoing a self-healing.

The last major topic addressed in this thesis deals with formulation of failure criteria, and their time-dependent evolution, in construction materials undergoing an environmental damage associated with subflorescence of salts (i.e., crystallization within the pores). The main focus is on *structural masonry* and its individual components. In natural conditions, as a result of capillary action, salts dissolved in water migrate inside the interconnected pores and then crystallize during the drying stage. When the evaporation rate is sufficiently high, salts crystallize directly in the pores (subflorescence). In this case, the crystallization pressure triggers the onset and propagation of micro-damage which results in degradation of mechanical properties at the macroscale. Over the last few decades, the research related to the effects of crystallization has focused on two aspects; one involving an experimental campaign on the quantification of damage, and the other dealing with formulation of the field equations governing the process of heat, moisture and salt transport combined with salt crystallization.

The laboratory experiments typically involve tests of continuous capillary rise or wetting/drying cycles. In the former case, the material is in contact at its base with a saline solution and an ongoing capillary rise compensates for the water evaporation [46, 47]. In accelerated tests, wetting cycles with saturated salt solutions are followed by drying in an oven [48, 49]. During the experiments, the effect of different parameters is examined, including the structure of precipitated salt, the evolution of pore size distribution, etc. However, these tests are seldom correlated with the evolution of strength/deformation parameters, which makes their relevance to assessment of durability of structures rather questionable. For this reason, the main focus in the research reported in this thesis is on establishing appropriate evolution laws which explicitly relate the variation in strength parameters to the volume fraction of salt precipitated in pores.

The mathematical framework for describing the crystallization process involves the field equations governing the heat, moisture and salt transport. The most general models take into account the material nonlinearities and mutual couplings between different mass transport processes [50, 51]. In addition, the kinetics of the salt phase is considered by postulating appropriate rate laws [52, 53]. Thus, the primary set of field equations involves water and dry air mass conservation, salt mass conservation, energy conservation, linear momentum conservation as well as an evolution law describing salt precipitation kinetics [50]. In general, the literature on numerical analysis of salt transport and crystallization is quite extensive (e.g., [54, 55]), however, there have been virtually no attempts to include and quantify the associated mechanical interaction. This interaction requires not only the specification of evolution laws governing the conditions at failure but also incorporation of additional terms in an inelastic type of constitutive relation which stem from time-dependent evolution of volume fraction of crystallized salt. The latter issue is directly addressed in the research reported here.

In this thesis, a comprehensive experimental study has been conducted examining the evolution of strength and deformation characteristics of primary constituents of masonry (i.e., bricks, mortar joints, and brick-mortar interfaces) during the process of salt crystallization. The evolution laws are phrased in terms of the degree of pore saturation with precipitated salt (i.e. volume of crystallized salt per volume of voids). The same parameter is subsequently employed in the development of the governing constitutive equations that couple the mechanical response with the salt transport and precipitation phenomena. The formulation is illustrated by some preliminary numerical examples. The latter deal with simulation of axial compression tests at different stages of the exposure to contamination, as well as tests involving the build up of axial strain associated with an increase in salt contamination at a constant axial load.

1.2 General scope

As mentioned earlier, this thesis contains three distinct journal papers integrated in the body of this work and forming Chapters 2-4. In what follows, a brief overview of each of these chapters is presented.

In **Chapter 2** a methodology for assessing the conditions at failure in interbedded sedimentary rocks is presented. The type of rock mass considered is representative of Carpathian Flysch Belt and has a sequence of interchanging claystone and sandstone layers with varying thickness. The approach involves generation of ‘virtual data’ through a mesoscale analysis that provides information on the strength properties for various orientations of stratification as well as various volume fractions of constituent layers. The data generated through this investigation is then employed to identify material functions that appear in a continuum framework. The performance of the proposed criterion is verified against a broad range of virtual data. It is demonstrated that the basic trends in the variation of strength, in terms of its spatial distribution as well as dependence on the volume fraction of constituents, can be predicted with a sufficient accuracy.

In **Chapter 3** a mathematical framework for describing the mechanical and hydraulic properties of fractured geomaterials undergoing self-healing (i.e. recovery of strength/stiffness) and self-sealing (i.e. reduction of permeability) is developed. Both these phenomena are described by introducing a scalar variable, which defines the kinetics of the process within the fractured zone. The evolution of this variable is time-dependent and may be affected by various external agencies, such as temperature, humidity, chemical/biological environment, etc. The effects of self-sealing are described using a variant of the embedded discontinuity framework incorporating a weak discontinuity in the fluid pressure [30]. The self-healing process is modeled by employing a hypoelastic-plastic idealization for the fractured zone in which the mechanical properties evolve in the course of healing. The upscaling from meso to macroscale employs again an embedded discontinuity approach. Some numerical examples are provided to illustrate the proposed methodology.

In **Chapter 4** the results of an experimental investigation on the variation of mechanical properties of primary constituents of structural masonry during the process of salt crystallization are provided. The interpretation of these results leads to specification of a set of evolution laws that describe the conditions at failure. A general form of an elastoplastic constitutive relation is discussed which relates the development of irreversible deformations to the volume fraction of crystallized salt. The framework was illustrated by some heuristic numerical examples assessing the mechanical response under sustained load in the presence of continuing salt contamination process.

Chapter 5 summarizes the main conclusions of the thesis, gives on overview of strength and limitations of the proposed approaches, and provides some suggestions for the future work.

1.3 References

[1]. Nasseri M.H.B, Rao K.S, Ramamurthy T (2003). Anisotropic strength and deformational behavior of Himalayan schists. Intern. Journ. Rock Mech. Min. Sci. 40: 3-23.

[2]. Ghazvinian E, Diederichs M.S, Labrie D, Martin C (2015). An investigation on the fabric type dependency of the crack damage thresholds in brittle rocks. Geotech Geol. Eng. 33: 1409–1429.

[3]. Selvadurai A.P.S, Najari M (2017). The thermo-hydro-mechanical behavior of the argillaceous Cobourg limestone. J. Geophys. Res. Solid Earth. 122: 4157– 4171.

[4]. Nanji J.H, Sushanta K.M, Madhu V (2012). Estimation of permeability heterogeneity in limestone outcrop by pressure measurements: Experiments and numerical simulation. Exp. Therm. Fluid Sci. 40: 177-184.

[5]. Selvadurai A.P.S, Głowacki A (2018). Estimates for the local permeability of the Cobourg limestone. Journ. Rock Mech. Geotech. Eng.10: 1009-1019.

[6]. Wild K.M, Barla M, Turinetti G, Amann F (2017). A multi-stage triaxial testing procedure for low permeable geomaterials applied to Opalinus Clay. Journ. Rock Mech. Geotech. Eng. 9: 519-530.

[7]. Minardi A, Giger S.B, Ewy R.T, Stankovic R, Stenebråten J, Soldal M, Rosone M, Ferrari A, Laloui L (2021). Benchmark study of undrained triaxial testing of Opalinus Clay shale: Results and implications for robust testing. Geomech. Energy Environ. 25: 100210.

[8]. Niandou H, Shao J.F, Henry J.P, Fourmaintraux D (1997). Laboratory investigation of the mechanical behaviour of Tournemire shale. Intern. Journ. Rock Mech. Min. Sci. 34: 3-16.

[9]. Cho J-W & Kim H, & Jeon S & Min K-B. (2012). Deformation and strength anisotropy of Asan gneiss, Boryeong shale, and Yeoncheon schist. Intern. Journ. Rock Mech. Min. Sci. 50: 158-169.

[10]. Pietruszczak S, Pakdel P (2022). On the mechanical anisotropy of argillaceous Cobourg limestone: fabric tensor approach. Intern. Journ. Rock Mech. Min. Sci. 150: 104953.

[11]. Duveau, G, Shao, J.F, Henry, J.P. (1998) Assessment of some failure criteria for strongly anisotropic geomaterials. Mech. Cohes. Frict. Mater. 3: 1-26.

[12]. Kwasniewski M.A (1993). Mechanical behavior of anisotropic rocks. In: *Comprehensive Rock Engineering*. Pergamon Press. 1: 285-312.

[13]. Jaeger J.C (1960). Shear failure of anisotropic rocks. Geol. Mag. 97: 65-72.

[14]. Nova R (1980). The failure of transversely isotropic rocks in triaxial compression. Intern. Journ. Rock Mech. Min. Sci. 17: 325–332.

[15]. Pariseau W.G (1968). Plasticity theory for anisotropic rocks and soil. In: Proceedings 10th US Symp. Rock Mech. 68: 0267.

[16]. Tsai S.W, Wu E. M (1971). A General Theory of Strength for Anisotropic Materials. Journ. Compos. Mater. 5: 58-80.

[17]. Boehler J.P, Sawczuk A (1977). On yielding of oriented solids. Acta Mech. 27: 185–204.

[18]. Zhang Y, Shao J, Liu Z, Shi C, Saxcé G.D (2019). Effects of confining pressure and loading path on deformation and strength of cohesive granular materials: a three-dimensional DEM analysis. Acta Geotech. 14: 443-460.

[19]. Duan K, Kwok C.Y, Pierce M (2016). Discrete element method modeling of inherently anisotropic rocks under uniaxial compression loading. Int. J. Numer. Anal. Meth. Geomech. 40: 1150– 1183.

[20]. Liakas S, O'Sullivan C, Saroglou C (2017). Influence of heterogeneity on rock strength and stiffness using discrete element method and parallel bond model. Journ. Rock Mech. Geotech. Eng. 9: 575-584.

[21]. Pietruszczak S, Mroz Z (2001). On failure criteria for anisotropic cohesive-frictional materials. Intern. Journ. Numer. Anal. Meth. Geomech. 25: 509–524.

[22]. Liu W, Zhang X, Li H, Chen J (2020). Investigation on the Deformation and Strength Characteristics of Rock Salt Under Different Confining Pressures. Geotech Geol Eng. 38: 5703–5717.

[23]. Duevel B, Haimson B (1997). Mechanical characterization of pink Lac du Bonnet granite: Evidence of nonlinearity and anisotropy. Intern. Journ. Rock Mech. Min. Sci. 34: 117.e1.

[24]. Eberhardt E, Stead D, Stimpson B (1999). Quantifying progressive pre-peak brittle fracture damage in rock during uniaxial compression. Intern. Journ. Rock Mech. Min. Sci. 36: 361-380.

[25]. Lau J.S.O, Jackson R, Gorski B (1991). The post failure behaviour of Lac du Bonnet granite, CANMET divisional report MRL 91-079 (TR), Dept. Energy, Mines and Resources, Ottawa.

[26]. Innocente J.C, Paraskevopoulou C, Diederichs M.S (2021). Estimating the long-term strength and time-to-failure of brittle rocks from laboratory testing. Intern. Journ. Rock Mech. Min. Sci. 147: 104900.

[27]. Lajtai E.Z, Duncan E.J.S, Carter B.J (1991). The effect of strain rate on rock strength. Rock Mech Rock Engng. 24: 99–109.

[28]. Behnsen J, Blake O, Cernik R, Withers P (2014). Identifying microcracks in multi-phase crystalline rocks by X-rayCT. Industrial Computed Tomography (iCT) Conference, e-Journal of Non-destructive Testing. 19: 25-28.

[29]. Bieniawski Z.T (1967). Mechanism of brittle fracture of rock. Part I: Theory of fracture process. Part II: Experimental studies. Part III: Fracture in tension and under long term loading. Intern. Journ. Rock Mech. Min. Sci. 4: 395-430.

[30]. Jameei A.A, Pietruszczak S (2023). Coupled hydromechanical analysis of sparsely fractured crystalline rocks. Comput. Geotech. 159: 105478.

[31]. Unteregger D, Fuchs B, Hofstetter G (2015). A damage plasticity model for different types of intact rock. Intern. Journ. Rock Mech. Min. Sci. 80: 402-411.

[32]. Lan H, Martin C.D, Hu B (2010). Effect of heterogeneity of brittle rock on micromechanical extensile behavior during compression loading. Journ. Geophys. Res. 115: 01202.

[33]. Chen Y, Hu S, Zhou C, Jing L (2013). Micromechanical Modeling of Anisotropic Damage-Induced Permeability Variation in Crystalline Rocks. Rock Mech. Rock Eng. 47.

[34]. Gordeliy E, Peirce A (2013). Coupling schemes for modeling hydraulic fracture propagation using the XFEM. Comp. Methods Appl. Mech. Eng. 253: 305–322.

[35]. Oda M, Hatsuyama Y, Ohnishi Y (1987). Numerical experiments on permeability tensor and its application to jointed granite at Stripa Mine, Sweden. J. Geophys. Res. 92: 8037–8048.

[36]. Lei G, Dong P, Mo S, Yang S, Wu Z, Gai S (2015). Calculation of full permeability tensor for fractured anisotropic media. J Petrol Explor Prod Technol 5: 167–176.

[37]. Xu W, Zhang Y, Li X, Wang X, Zhang P (2019). Study on three-dimensional fracture network connectivity path of rock mass and seepage characteristics based on equivalent pipe network. Environ Earth Sci. 78: 516.

[38]. Xu C, Fidelibus C, Dowd P (2014). Realistic pipe models for flow modelling in Discrete Fracture Networks. 1st International Discrete Fracture Network Engineering Conference, Vancouver, Canada: DFNE 2014 – 132.

[39]. Aliko-Benitez A, Doblare M, Sanz-Herrera J.A (2015). Chemical-diffusive modeling of the self-healing behaviour in concrete. Intern. Journ. Solids & Struct. 69-70: 392-402.

[40]. Van Tittelboom K, De Belie N. (2013). Self-healing in cementitious materials – a review. Materials. 6: 2182-2217.

[41]. Granger S, Loukili A, Pijaudier-Cabot G, Chanvillard G (2007). Experimental characterization of the self-healing cracks in an ultra high performance cementitious material: mechanical tests and acoustic emission analysis. Cem. Concr. Res. 37:519-527.

[42]. Costin L.S, Wawersik W.R (1980). Creep healing of fractures in rock salt. Sandia National Lab. Rep. 80: 1375.

[43]. Elkhoury J.E, Detwile R.L, Ameli P (2015). Can a fracture caprock self-heal? Earth Plant. Sci. Lett. 417: 99-106.

[44]. Renard F, Gratier J.P, Jamtveit B (2000). Kinetics of crack-sealing, intergranular pressure solution, and compaction around active faults. Journ. Struct. Geol. 22: 1395–1407.

[45]. Jameei A.A, Pietruszczak S (2020). Embedded discontinuity approach for coupled hydromechanical analysis of fractured porous media. Int J Numer Anal Methods Geomech. 44: 1880– 1902.

[46]. Charola A.E, Bläuer C (2015). Salts in masonry: an overview of the problem. Restoration of Buildings and Monuments. 21: 119-135.

[47]. Flatt R, Aly Mohamed N, Caruso F, Derluyn H, Desarnaud J, Lubelli B, Espinosa Marzal R.M, Pel L, Rodriguez-Navarro C, Scherer G.W, Shahidzadeh N, Steiger M (2017). Predicting salt damage in practice: a theoretical insight into laboratory tests. RILEM Tech Lett. 2: 108-118.

[48]. Stryszewska T, Kańka S (2014). Microstructure of ceramic brick contaminated by magnesium sulphate. Advances in Science and Technology. 92: 203-208.

[49]. Bompa D.V, Elghazouli A.Y (2021). Mechanical properties of hydraulic lime mortars and fired clay bricks subjected to dry-wet cycles. Constr. Build. Mater. 303: 124458.

[50]. Koniorczyk M, Gawin D, Schrefler B.A (2018). Multiphysics model for spalling prediction of brick due to in-pore salt crystallization. Comp. Struct. 196: 233-245.

[51]. Abed A.A, Sołowski W.T, Romero E, Gens A (2018). Inclusion of chemical effect in a fully coupled THM finite element code. International Conference on Unsaturated Soils. 2: 827-832.

[52]. Desarnaud J, Bertrand F, Shahidzadeh-Bonn N (2013). Impact of the kinetics of salt crystallization on stone damage during rewetting/drying and humidity cycling. ASME. J. Appl. Mech. 80: 020911.

[53]. Espinosa R.M, Franke L, Deckelmann G (2008). Phase changes of salts in porous materials: crystallization, hydration and deliquescence. Construction and Building Materials, 22: 1758-1773.

[54]. Gentilini C, D'Altri A, Amato M, Zanotti P, Favaro F, Miranda S (2017). Salt attack effects on the shear behavior of masonry: preliminary results of an experimental campaign. Key Engineering Materials. 747: 512–517.

[55]. Grementieri L, Daghia F, Molari L, Castellazzi G, Derluyn H, Cnudde V, Miranda S (2017). A multi-scale approach for the analysis of the mechanical effects of salt crystallisation in porous media. Intern Journ. Solids Struct. 126–127: 225-239.

Chapter 2

On specification of conditions at failure in interbedded sedimentary rock mass

Przecherski P, Pietruszczak S (2020). On specification of conditions at failure in interbedded sedimentary rock mass. Acta Geotech. 15: 365–374. https://doi.org/10.1007/s11440-019-00794-x

On specification of conditions at failure in interbedded sedimentary rock mass

P. Przecherski (1) and S. Pietruszczak(1), (2)

(1) *Cracow University of Technology, Cracow, Poland*

(2) *McMaster University, Hamilton, Ont., Canada*

Abstract

This paper presents a methodology for assessing the conditions at failure in interbedded sedimentary rocks. The type of rock mass considered here is representative of Carpathian Flysch Belt and has a sequence of alternating deposits of claystone and sandstone with varying thickness. The approach involves a numerical investigation at the mesoscale that allows the assessment of strength properties for different orientations of stratification. A comprehensive set of data generated through this investigation is then employed to identify material functions in a continuum framework that accounts for the effects of inherent anisotropy at the macroscale. The conditions at failure in both compression and tension regimes are addressed and the performance of the macroscopic criterion is verified for different stress trajectories. A simplified procedure for incorporating the influence of volume fraction of constituents within the proposed macroscopic formulation is also suggested.

Keywords: Carpathian Flysch, Mesoscale analysis, Inherent anisotropy, Failure criterion

1. Introduction

The geological formation studied in this work is known as Flysch. It is a sequence of sedimentary rock layers that is formed in a low-energetic depositional environment. The structure of the material examined here is typical of the Carpathian Flysch Belt and has an arrangement of alternating marine deposits of claystones and sandstones with varying thickness. For this type of rock formation, the strength properties strongly depend on the orientation of bedding planes and the volume fractions of constituents. An adequate description of these effects is of a significant importance due to the widespread applications of sedimentary rocks in many types of geo-engineering projects, including construction of underground structures, design of slopes/excavations, deep geological disposal of radioactive waste, etc.

The modeling of mechanical behaviour of stratified rocks requires, first of all, the specification of conditions at failure under an arbitrary stress state. Over the last few decades, a significant effort has been devoted to both theoretical and experimental research dealing with the notion of anisotropy at the macroscale. The experimental works focused mainly on the correlation of axial strength, at different confinements, with orientation of the sedimentary layers. An overview is provided for example in Refs. [1, 17] The results generally indicate that the maximum compressive strength is associated with horizontal or vertical layering, relative to the direction of loading, while the minimum strength has been observed for orientations between 30 and 60 degrees [14, 15, 24]. In the tensile regime, the strength for tension perpendicular to the layering is significantly lower than that for tension along the sedimentary layers [4, 6, 11]. In the presence of heterogeneous deposits, like Flysch, the quantitative results are strongly affected by the volume fraction of constituents.

In parallel with experimental investigations, a significant amount of research has been done on formulation of anisotropic failure criteria. A comprehensive review on this topic, examining different approaches, is provided for example in Refs. [2, 7]. In general, the existing criteria are based on either an empirical approach or a more rigorous continuum framework that incorporates some measures of microstructure. Examples of the former include extensions of Hoek-Brown or other isotropic failure criteria to account for strength anisotropy (e.g. [22, 23]). For the continuum formulations, one of the first attempts was an extension of Hill’s criterion [8], as reported by Pariseau [18]. Later, a more general framework was developed that incorporated the basic and mixed invariants of stress and microstructure tensors (cf. [5, 16]). Although mathematically rigorous, the latter approach has never been applied to any practical engineering problem in view of complexities associated with identification of material functions employed. In addition to continuum frameworks, some failure criteria postulating the existence of discrete weakness plane(s) have also been proposed. Those include the early work of Jaeger [10] and its subsequent enhancements (e.g. [28]).

The present work builds on a pragmatic continuum approach outlined by Pietruszczak & Mroz [19], which incorporates a scalar anisotropy parameter. The latter defines the strength properties as a function of orientation of the sample relative to the loading direction and can be explicitly identified with a mixed invariant of stress and structure-orientation tensors. Given the inherent difficulties associated with a large-scale testing of interbedded rock mass, a different methodology is proposed here whereby the strength properties for various orientations of stratification are assessed based on a numerical analysis that is carried out at the mesoscale. A comprehensive set of ‘virtual data’ generated through this investigation is then employed to identify material functions in the continuum framework. In the next section, the formulation of the problem is outlined, and the results of FE simulations are provided. The conditions at failure in both compression and tension regimes are addressed. Subsequently, the procedure for specification of material functions, including their dependence on the volume fraction of constituents, is proposed and the performance of the macroscopic criterion is examined for different loading histories. The last section provides the final remarks and conclusions emerging from this study.

2. Assessment of conditions at failure; mesoscale approach

There are inherent difficulties associated with testing of interbedded sedimentary formations. Laboratory testing poses significant restrictions on the sample size; the largest dimension is typically within the range of 10-50 cm which is much smaller than that associated with REV. Thus, these tests are suitable to define the properties of constituents but cannot be relied on in terms of assessing the properties at the macroscale. The in-situ tests, although more representative, are expensive, employ quite limited loading paths and the results display a strong size effect. In view of those difficulties, the approach advocated here involves a simple computational assessment of strength based on properties of constituents and their respective volume fractions. Given this set of ‘virtual data’, a macroscopic criterion can be formulated accounting for the effects of anisotropy, and the associated material functions can be identified. The performance of the phenomenological criterion can then be verified in a broad range of loading trajectories and the results compared with those of mesoscale simulations. The details of the proposed methodology are described in sections 2.1-3.2 below.

2.1 Formulation: failure criteria for constituents

Fig.1 shows schematically the structure considered at the mesoscale. The constituent materials are the sandstone and claystone with given strength properties and the volumetric fractions μ_1 and $\mu_2 = 1 - \mu_1$, respectively. Assume that the conditions at failure for both these materials can be approximated using the classical Mohr-Coulomb criterion with Rankine’s cut-off in the tensile regime. Thus,

$$F = \max(F_1, F_2) = 0; \quad F_1 = \sqrt{3}\bar{\sigma} - \eta_f g(\theta)(\sigma_m + C); \quad F_2 = \max_{n_i}\left(\sigma_{ij} n_i n_j - f_t(n_i)\right) \quad (1)$$

where, $\bar{\sigma} = (J_2)^{1/2}$; $\sigma_m = -\frac{1}{3} I_1$; $\theta = \frac{1}{3}\sin^{-1}\left(\frac{-3\sqrt{3}}{2}\frac{J_3}{\bar{\sigma}^3}\right)$ and

$$g(\theta) = \frac{3 - \sin\phi}{2\sqrt{3}\cos\theta - 2\sin\theta\sin\phi}; \qquad \eta_f = \frac{6\sin\phi}{3 - \sin\phi}; \qquad C = c\cot\phi \qquad (2)$$

In the expressions above, I_1 is the first stress invariant, while J_2, J_3 are the basic invariants of the stress deviator. Moreover, θ is the Lode's angle, ϕ and c are the angle of friction and cohesion, respectively. For the tension cut-off criterion, i.e. the third equation in (1), n_i defines the unit normal to the plane, while f_t is the corresponding tensile strength. Note that, for an isotropic material, $f_t = const.$ so that the Lagrangian function becomes

$$G = \sigma_{ij} n_i n_j - f_t - \lambda(n_i n_i - 1) \qquad (3)$$

where λ is the Lagrangian multiplier. Imposing the stationary condition of G with respect to n_i leads to an eigenvalue problem

$$\frac{\partial G}{\partial n_i} = 0 \rightarrow \left(\sigma_{ij} - \lambda\delta_{ij}\right) n_j = 0 \qquad (4)$$

which implies that the failure plane is orthogonal to the direction of maximum tensile stress σ_3 , i.e. $n_i = e_i^{(3)}$. Thus, for an isotropic material, the tensile failure criterion is equivalent to $F_2 = \sigma_3 - f_t = 0$.

The macroscale representation of conditions at failure, as discussed later in Section 3, will employ the same functional form (1) enhanced by incorporating the notion of structural anisotropy through the dependence of strength properties (viz. η_f and f_t) on the relative orientation of principal stress and material axes.

2.2 Numerical simulations

The assessment of strength at the macroscale is based now on standard FE analysis that incorporates the microstructure shown in Fig.1. The simulations employ an elastic–perfectly plastic idealization and involve a series of tests performed at different confining pressures, different orientations of the sedimentary layers relative to the direction of loading and different volume fractions of constituents. The material parameters were assigned the values which are typical for both constituents [12], i.e

Sandstone: $\phi = 39^0$, $c = 14$ MPa, f_t = 13.3 MPa, E = 11.9 GPa, ν= 0.2

Claystone: $\phi = 32^0$, $c = 4$ MPa, f_t = 4.4 MPa, E = 6.3 GPa, ν= 0.17

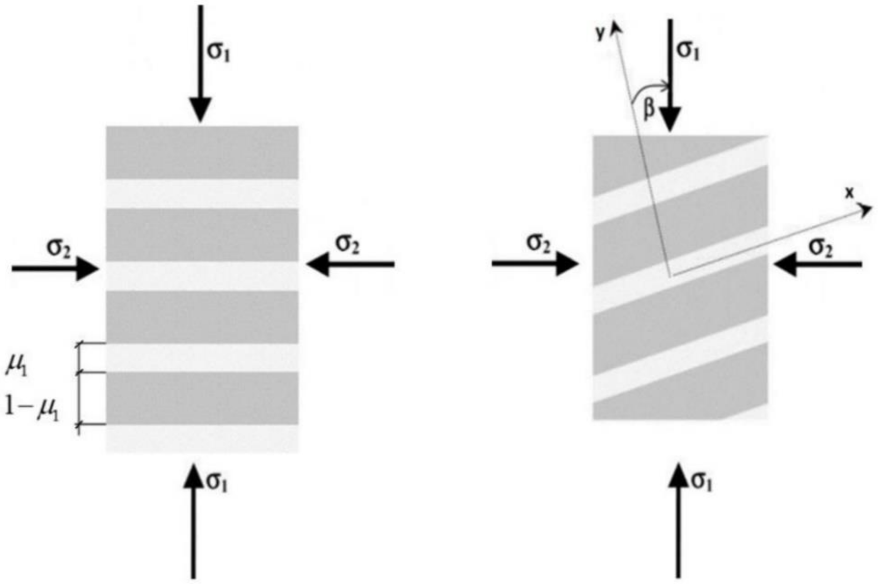

Fig 1. Geometry of the microstructure and definition of the angle β

Note that, since the objective is to define the magnitude of surface traction at failure, with no reference to deformation, the stiffness properties are of no significance here. The testing configuration was simulated by employing a three-dimensional mesh of 8-noded solid elements. An example of the FE discretization, which corresponds to volume fraction of sandstone equal to 20%, i.e. $\mu_1 = 0.2$, is shown in Fig.2. Here, the sample has the dimensions 1m x 2m, while the layer spacing is 0.1m. It needs to be pointed out that there is no unique criterion for choosing the sample size. The main requirements are that it should be representative of the rock mass at the engineering scale of the problem and the layer spacing should be small compared to its dimensions.

The loading setup was assumed to be force-controlled, i.e. uniform tractions were imposed along the boundaries while the nodes located at the centroid of the specimen were fixed. The tests involving different orientation of layers were simulated by maintaining the same FE mesh and transforming the boundary tractions to the principal material system. The loading histories that were simulated involved axial compression at different confinements, ranging from 0-20

MPa, as well as uniaxial tension. The analysis was conducted for different orientations of layering (in 15° intervals) and different volume fractions of constituents (in 20% intervals).

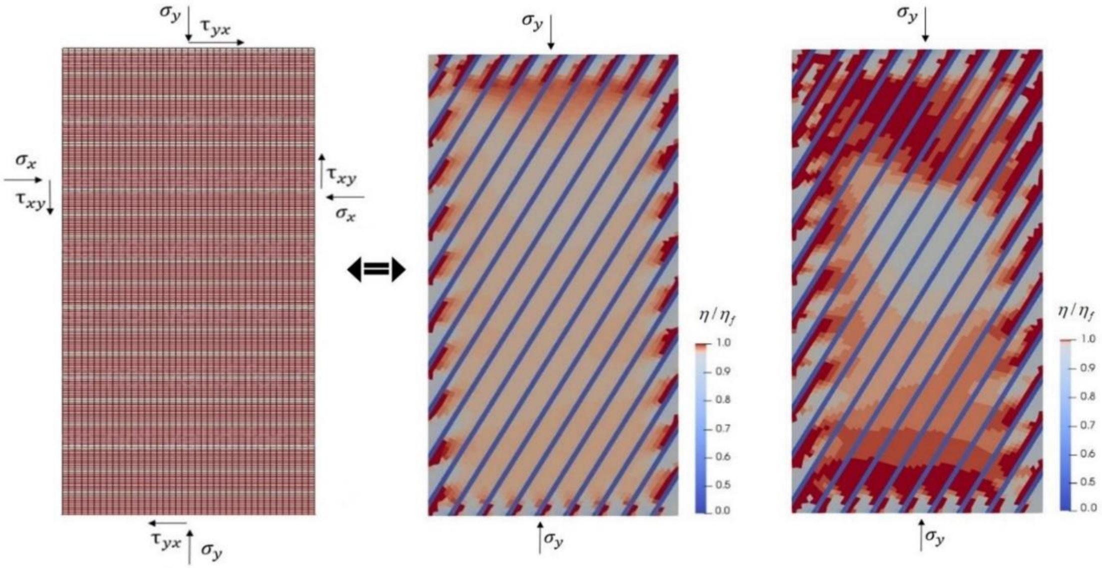

Fig 2. Finite element discretization and evolution of damage factor $\eta/\eta_f = \sqrt{3}\bar{\sigma}/\,g(\theta)\left(\sigma_m + C\right)$

The main results of the simulations are presented in Fig.3. The figure shows the evolution of axial *compressive* strength with the inclination angle (β) for different volume fractions of sandstone. The results correspond to different initial confining pressures, which are within a relatively narrow range of 0-20MPa, The latter stems from limitations of the linear form of the Mohr-Coulomb criterion (1). Apparently, for rock-like materials subjected to high confining stress a non-linear approximation in the meridional space ($\bar{\sigma} - \sigma_m$) is required, as evidenced by the experimental data (e.g. [3, 9]). The results obtained here show that the compressive strength increases with the increase in confinement as well as the volume fraction of sandstone. It can be noted that the anisotropy effects are progressively reduced as the percentage of claystone fraction increases. It is also evident that the strength is almost the same for horizontal and vertical samples, while the minimum strength is attained at approx. $\beta = 60^\circ$. In the latter case, the failure is localized in claystone layers, which are the weakest link, so that the axial strength is virtually independent of the volume fraction of sandstone.

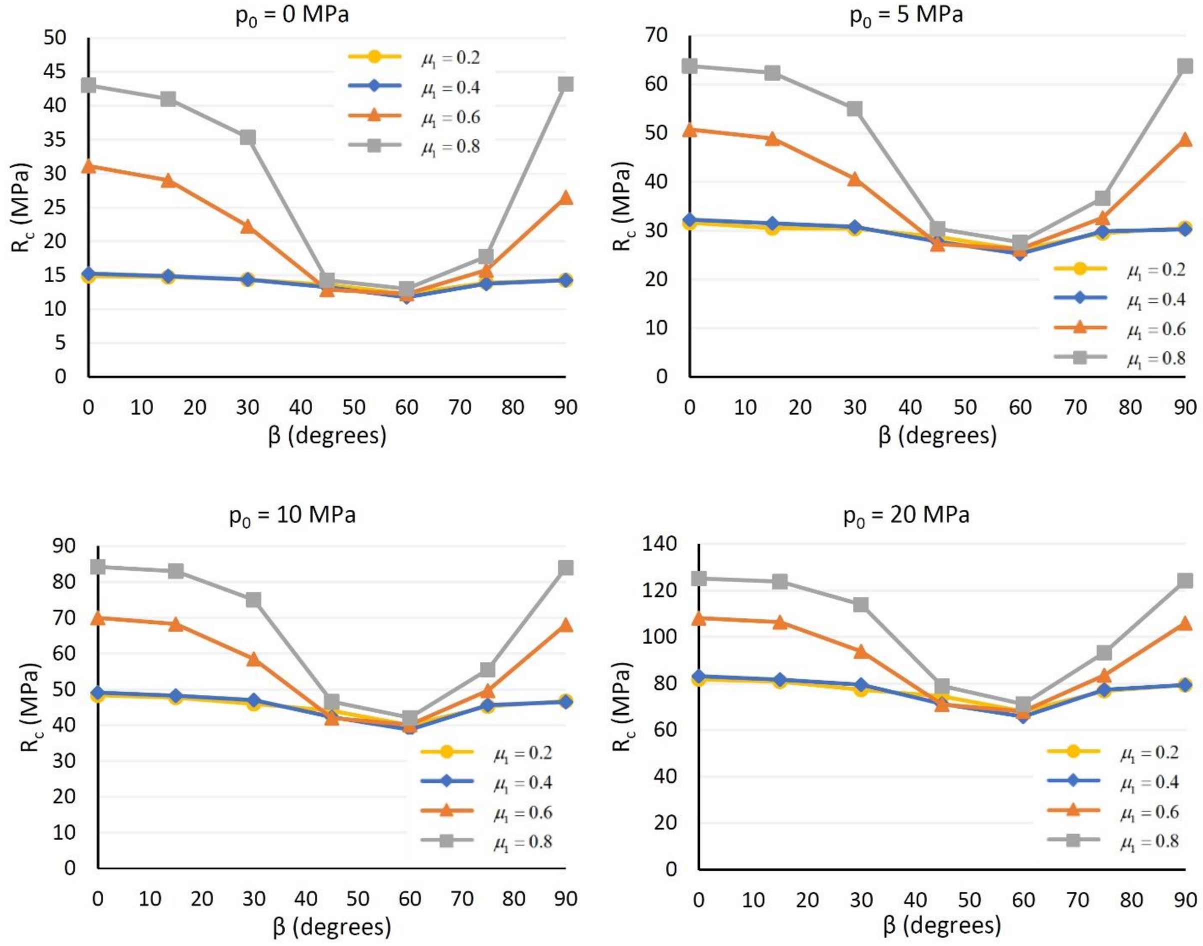

Fig 3. Evolution of axial compressive strength R_c with the inclination angle β for different volume fractions and confining pressures p_o

As mentioned earlier, the simulations have been carried out assuming an elastic perfectly-plastic response. Since the problem is solved as load-controlled, the loss of stability is typically associated with divergence of the Newton-Raphson iterative scheme. Note that the assessment of the ultimate load can also be based on monitoring the evolution of the second rate of work. In this case, it is convenient to define a stability factor [21]

$$SF = \int_V \dot{\sigma}_{ij}\dot{\varepsilon}_{ij}\, dV \Big/ \int_V \dot{\sigma}^e_{ij}\dot{\varepsilon}_{ij}\, dV \qquad (5)$$

Here, the denominator represents the second rate of work in an elastic continuum; σ_{ij} is the actual stress rate, σ^e_{ij} is the elastic stress rate, while the integration is carried out over the entire domain. It should be noted that in the elastic range there is SF=1, whereas at the onset of instability SF becomes equal to zero. In general, SF>0 requires the *global* stiffness operator to be positive definite. Apparently, all of the eigenvalues of a positive definite matrix are positive so that such matrix is invertible. Thus, when SF=0 a structure becomes unstable as its stiffness matrix will have one (or more) eigenvalue(s) equal to zero. As an illustration, Fig.4a shows the load-displacement curve for one of the cases considered, viz. $p_0 = 0\,\text{MPa}$, $\mu_1 = 0.6$, $\beta = 0^\circ$, while Fig.4b shows the corresponding evolution of the stability factor. It is evident that when the ultimate load is approached there is $\text{SF} \rightarrow 0$. In general, the notion of assessing stability by monitoring the evolution of the second rate of work is typically invoked in the dynamic analysis [21]. It can, however, be very useful for static considerations as well, for example in evaluation of stability of geotechnical structures where the triggering factor is either the self-weight or the environmental load (e.g., rain infiltration).

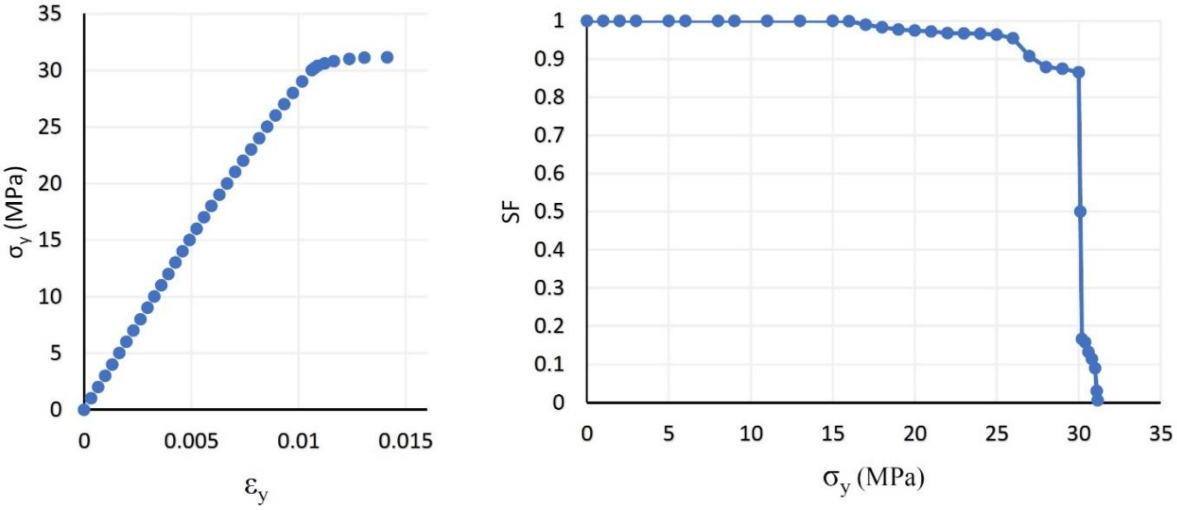

Fig 4. Evolution of stability factor Eq. (5) for uniaxial compression

It is also worth noting that, given the periodic nature of the mesostructural arrangement of Flysch, the numerical analysis may be conducted by considering a unit cell of representative elementary volume (REV) subjected to periodic boundary conditions (e.g. [25, 27]). However, for a simple perfectly-plastic idealization as employed here, the execution time associated with analysis of the entire sample is very fast so that the question of numerical efficiency is not a major issue. In general, both types of analyses (i.e. entire sample vs periodic unit cell) impose some constraints on the displacement field. Furthermore, the notion of unit cell of REV may be questioned in case of localized deformation.

Finally, a set of simulations has also been conducted for uniaxial *tension* at different orientation of the sedimentary layers. The analysis incorporated the Rankine's failure function

F_2 , eq. (1). The main results are presented in Fig.5, which shows the directional variation of the tensile strength. Apparently, the strength is the highest for tension along the bedding while the minimum value is associated with tension in the direction of deposition. The results presented here correspond to the volume fractions of sandstone $\mu_1 = 0.2$ and $\mu_1 = 0.8$. In general, for tension perpendicular to bedding planes the failure occurs in the weak layers and the strength is the same as that of the claystone. Therefore, the solution is independent of the volume fraction in a lower range of bedding planes orientations.

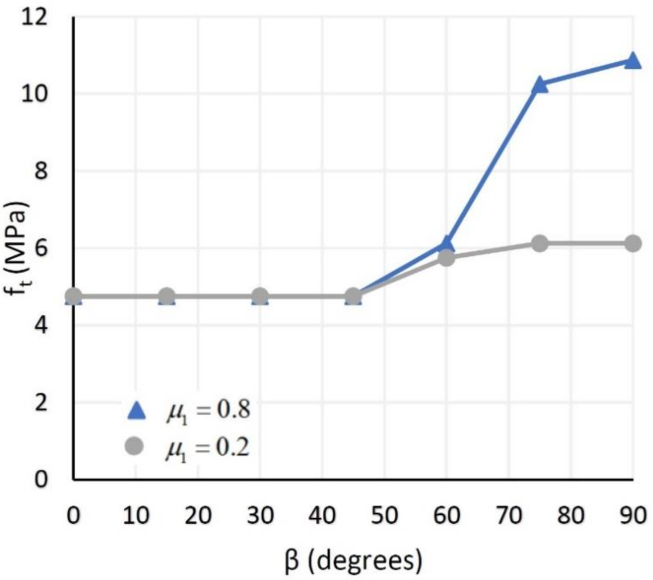

Fig.5 Variation of tensile strength with bedding planes orientation β

The outcome of numerical simulations described above, viz. tests in compression and tension regimes, provides now a set of ‘virtual data’ which can be employed to define a macroscopic failure criterion that accounts for the effects of volume fraction of constituents as well as the anisotropy in the strength characteristics. Using this set of data, the associated material functions/parameters can be explicitly identified.

3. Assessment of conditions at failure; a continuum approach

The macroscopic failure criterion is obtained by preserving the functional form consistent with representation (1) and postulating that the respective strength parameters depend on the orientation of the sample relative to the loading direction. In particular, in compression regime, the formulation incorporating the microstructure tensor is employed and is subsequently extended to incorporate the influence of volume fraction of constituents.

3.1 Formulation and identification of material functions

Referring to the functional form (1)-(2), assume that the values of the strength parameters (viz. η_f, C and f_t) depend on the relative orientation of principal axes of stress and the microstructure. Note that, in the context of the Mohr-Coulomb criterion, i.e. the failure function F_1, the parameter C is associated with a hydrostatic stress state. For the latter, the behaviour is invariant with respect to orientation of the sample, so that the effects of anisotropy can be primarily attributed to spatial variation in the strength descriptor η_f. Following the methodology outlined in Ref. [19], the anisotropy function is expressed in the form

$$\eta_f = \hat{\eta}_f \left(1 + A_{ij} l_i l_j + a_1 (A_{ij} l_i l_j)^2 + a_2 (A_{ij} l_i l_j)^3 + \cdots\right); \qquad C = const. \tag{6}$$

Here, l_i represents a versor along a generalized *loading vector* L_i, that is defined as

$$l_i = \frac{L_i}{(L_k L_k)^{1/2}}; \quad L_i = L_j e_i^{(j)}; \quad L_j = (\sigma_{j1}^2 + \sigma_{j2}^2 + \sigma_{j3}^2)^{1/2} \tag{7}$$

Thus, the components of L_i are the magnitudes of tractions on planes normal to the principal material axes $e_i^{(\alpha)}, \alpha = 1,2,3$. The latter are defined by the eigenvectors of the operator A_{ij}, which is a traceless second-order tensor. Note that for the interbedded structure, typical of Flysch, representation (6) does not require a specific definition of the fabric measure. This is because of the strong inherent anisotropy; i.e. the principal material directions are known *a priori* and do not change in the course of deformation.

The dependence of the strength properties on the volume fraction of constituents can, in general, involve an assumption that the eigenvalues of A_{ij}, as well as the approximation coefficients are function of μ_1, i.e.

$$\eta_f = \eta_f(l_i, \mu_1) \Rightarrow \hat{\eta}_f = \hat{\eta}_f(\mu_1); \; A_{ij} = A_{ij}(\mu_1); \; a_1 = a_1(\mu_1); \; a_2 = a_2(\mu_1) \ldots \tag{8}$$

Note that, since Flysch is transversely-isotropic on the macroscale, the problem can be referred to the coordinate system attached to material axes, Fig.1. In this case

$$A_{ij}l_il_j = A_1(1-3l_2^2) \;\Rightarrow\; \eta_f = \hat{\eta}_f\left(1+A_1(1-3l_2^2)+a_1A_1^2(1-3l_2^2)^2+a_2A_1^3(1-3l_2^2)^3+\cdots\right) \quad (9)$$

where $\hat{\eta}_f, A_1, a_1, a_2 ...$ are assumed to depend on μ_1.

For failure in tension regime, Rankine's failure criterion F_2=0 , eq. (1), can be expressed as

$$F_2 = \max_{n_i}\left(\sigma_{ij}n_in_j - f_t(n_i)\right)=0; \quad f_t = \hat{f}_t\left(1+\Omega_{ij}n_in_j+b_1(\Omega_{ij}n_in_j)^2+b_2(\Omega_{ij}n_in_j)^3+\cdots\right) \quad (10)$$

Here, Ω_{ij} is again a symmetric traceless tensor which describes the bias in the spatial distribution of tensile strength f_t and $b_1, b_2 \ldots$ are the coefficients of approximation. In this case, the Lagrangian function becomes

$$G = \sigma_{ij}n_in_j - \hat{f}_t(1+\Omega_{ij}n_in_j+b_1(\Omega_{ij}n_in_j)^2+b_2(\Omega_{ij}n_in_j)^3+\cdots)-\lambda_1(n_in_i-1) \qquad (11)$$

It should be noted for a linear approximation, i.e. $b_1=b_2=...=0$, the stationary condition of *G* with respect to n_i leads to an eigenvalue problem

$$\frac{\partial G}{\partial n_i}=0 \;\rightarrow (B_{ij}-\lambda\delta_{ij})n_j=0; \quad B_{ij}=\sigma_{ij}-\hat{f}_t\,\Omega_{ij} \qquad (12)$$

which implies that the failure plane is no longer orthogonal to the direction of maximum tensile stress σ_3 (cf. eq.(4)).

Apparently, if the problem is referred to the coordinate system attached to material axes, Fig.1, there is

$$\Omega_{ij}n_in_j = \Omega_1(1-3n_2^2) \;\Rightarrow\; f_t = \hat{f}_t\left(1+\Omega_1(1-3n_2^2)+b_1\Omega_1^2(1-3n_2^2)^2+b_2\Omega_1^3(1-3n_2^2)^3+\cdots\right) \quad (13)$$

where coefficients $\hat{f}_t, \Omega_1, b_1, b_2 ...$ may again be assumed to depend on the volume fraction μ_1.

Let us focus now on the identification of material functions employed in the formulation of the macroscopic failure criterion. Consider first the specification of the function $\eta_f = \eta_f(l_i)$, eq.(6), for a fixed volume fraction of sandstone, selected here as $\mu_1 = 0.6$. The identification process is based on the results of the series of axial compression tests presented in Fig.3. The first step is the assessment of the value of the parameter *C*, eqs.(1)-(2). For this purpose, the conditions at failure for different inclination angles (β) have been projected on the 'triaxial'

(p,q)-plane and approximated with a linear form of Mohr-Coulomb envelope, as shown in Fig.6. The parameter C, which is defined as the intercept with the p-axis, has been estimated using the orientation average for all tests. For the assumed value of $\mu_1 = 0.6$, this resulted in $C = 8.52\,\text{MPa}$.

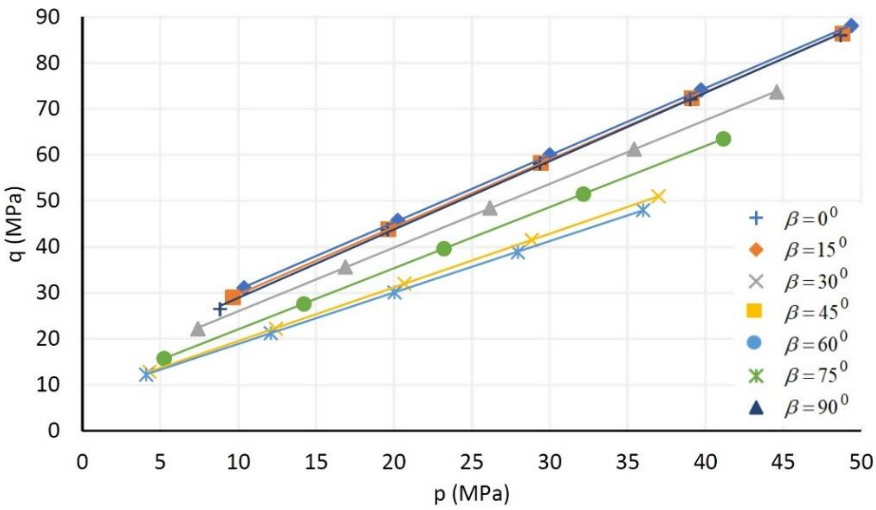

Fig 6. Approximation of conditions at failure for different sample orientations;
$p = (\sigma_1 + 2\sigma_3)/3, \quad q = \sigma_1 - \sigma_3$

Given this value, the material function $\eta_f = \eta_f(l_i)$ has been identified. In this case, for each specific orientation of the sample and the given confining pressure, the value of η_f satisfying $F_1 = 0$ (viz. eq.(1)) was determined, together with the corresponding loading direction. The results generated a set of data in the affine plane $\eta_f - l_2$, which was then approximated using the best-fit (i.e. least-square) procedure employing representation (9). This is shown in Fig.7, which presents the fifth-order approximation resulting in

$$\hat{\eta}_f = 1.65, \quad A_1 = -0.013, \quad a_1 = 7.19, \quad a_2 = 22.98, \quad a_3 = 26.18, \quad a_4 = 9.57$$

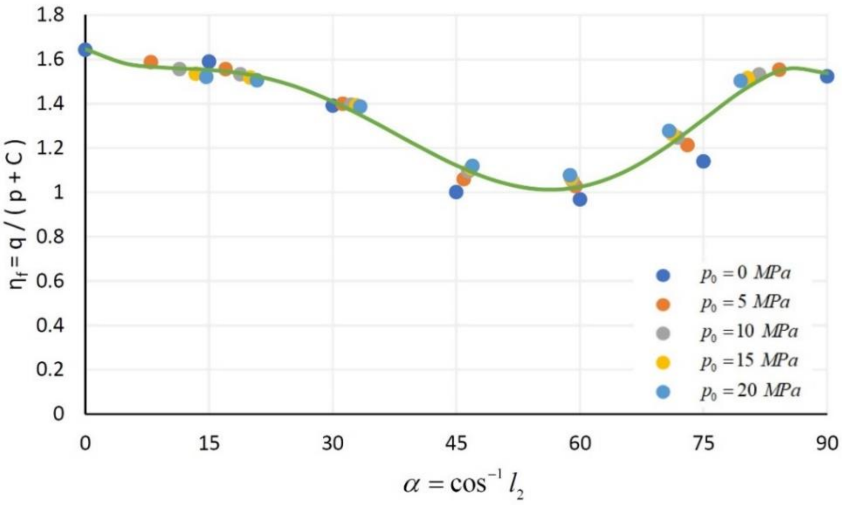

Fig 7. Variation of parameter η_f with the loading angle α

Given the above values of the approximation coefficients, the performance of the framework can now be verified against the complete set of 'virtual data'. The results of numerical simulations, corresponding to the selected value of $\mu_1 = 0.6$, are presented in Fig.8. It is seen that the predictions of axial strength are fairly reasonable over the entire range of $\beta \subset (0^\circ, 90^\circ)$

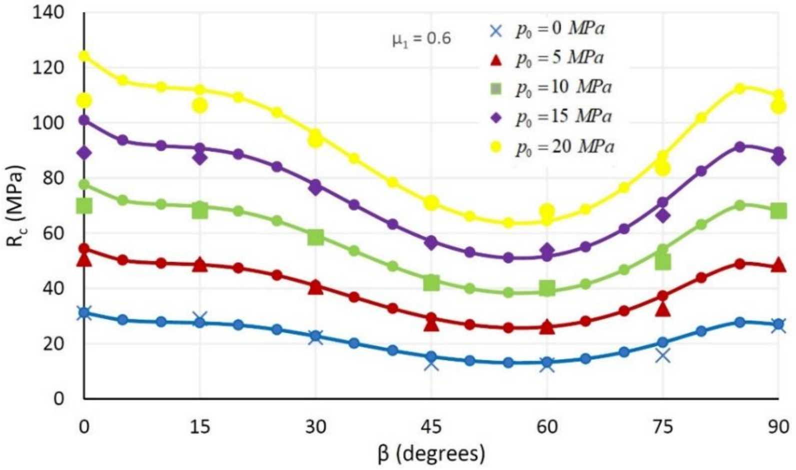

Fig 8. Predicted evolution of compressive strength R_c ($\mu_1 = 0.6$) for different orientations β and different confining pressures

Consider now the assessment of strength in the tensile regime based on the criterion (10). Fig.9 shows the predictions for the volume fraction of sandstone $\mu_1 = 0.8$ (cf. Fig.5), based on a fourth order approximation to $f_t(n_i)$, eq.(13). In this case, the coefficients of approximation have been determined explicitly by assuming the values of f_t for a number of discrete orientations (viz. $\beta = 0^\circ, 45^\circ, 60^\circ, 75^\circ, 90^\circ$), as reported in Fig.5, and solving the corresponding set of algebraic equations. This resulted in

$$\hat{f}_t = 8.12\,\text{MPa},\ \ \Omega_1 = 0.074,\ \ b_1 = -16.97,\ \ b_2 = 579.89,\ \ b_3 = 4.13 * 10^3$$

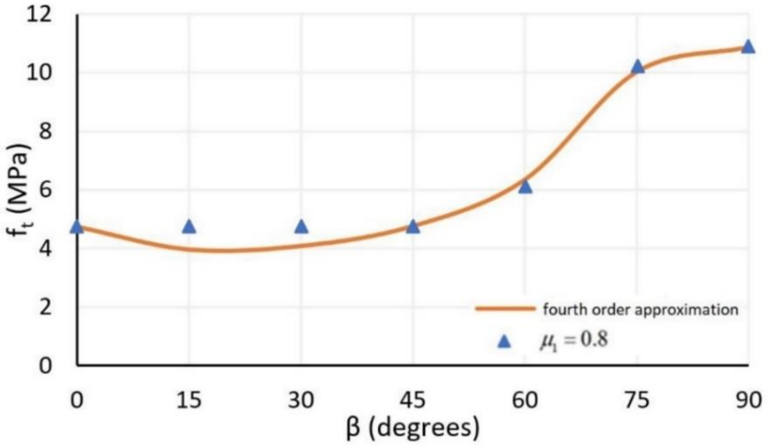

Fig 9. Variation of tensile strength with bedding planes orientation β (fourth order approximation)

It is evident from Fig.9 that such approximation is quite accurate. Obviously, lower order representation may be employed, which will be less precise. The simplest is the linear form (i.e. $b_1 = b_2 = ... = 0$) for which the approximation coefficients can be determined based on the values of f_t corresponding to $\beta = 0^\circ, 90^\circ$. In this case, there is

$$\hat{f}_t = \left(f_t(0^\circ) + 2 f_t(90^\circ) \right) / 3; \quad \Omega_1 = f_t(90^\circ) / f_t(0^\circ) - 1$$

while the orientation of the critical plane is obtained by solving the eigenvalue problem (12).

3.2 Simplified identification procedure for different volume fractions of constituents

The last issue to be addressed is the extension of the framework to account for variation in the volume fraction of constituent materials. The most accurate approach involves identification of coefficients of approximation for all discrete values of μ_1 (cf. results in Fig.3), using the procedure described in the previous section. For each of those coefficients a best fit approximation, employing for example a polynomial representation, can then be established relating its value to the volume fraction μ_1. This is the most general procedure that will optimize the performance in broad range of values of μ_1; it is, however, rather time consuming. Therefore, a simplified approach is suggested here as described below.

The proposed procedure makes use of the results of *uniaxial* compression (i.e. at no confinement). In this case, the loading direction can be identified with the orientation of the sedimentary layers, i.e. $l_2 = \cos\beta$, so that representation (9) simplifies to

$$\eta_f = \hat{\eta}_f \left(1 + A_1(1-3\cos^2\beta) + a_1 A_1^2(1-3\cos^2\beta)^2 + a_2 A_1^3(1-3\cos^2\beta)^3 + \cdots\right) \tag{14}$$

Given now the results of uniaxial compression tests (Fig. 3a), the relation between the strength parameter η_f and the volume fraction of sandstone μ_1 can be established for different orientations β. This is shown in Fig.10a, where the 'virtual data' is indicated by dots. Thus, for an arbitrary volume fraction μ_1, a discrete set of values of η_f can be obtained as an explicit function of β. As an illustration, Fig.10b presents the relation η_f vs. β for μ_1=0.6. The best-fit curve can now be constructed using representation (14), which will yield the corresponding values of the approximation coefficients. Here, a third-order approximation is shown for which

$$\hat{\eta}_f = 1.66, \quad A_1 = 0.0013, \quad a_1 = -0.0059, \quad a_2 = 0.00001$$

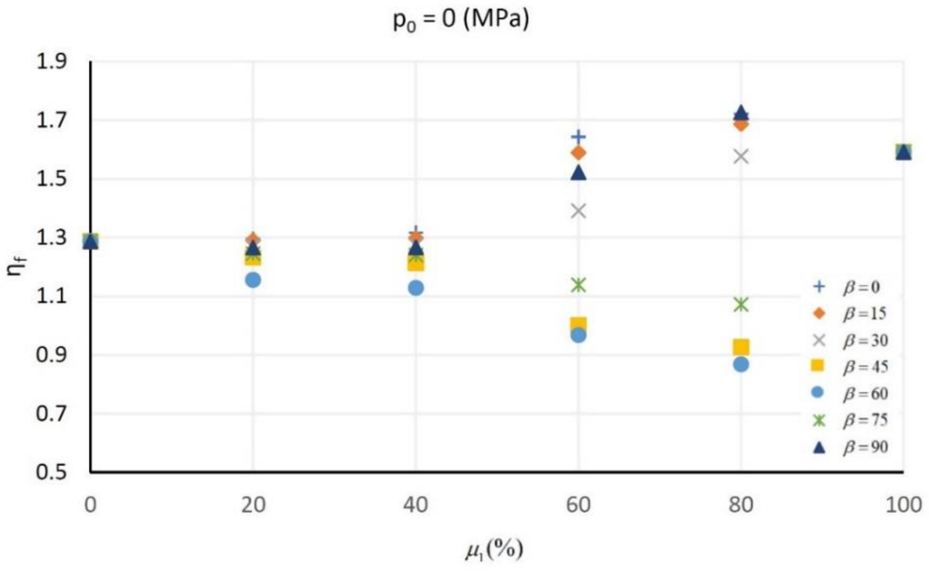

Fig 10a. Relation between the strength parameter η_f and the volume fraction μ_1 for different orientations β

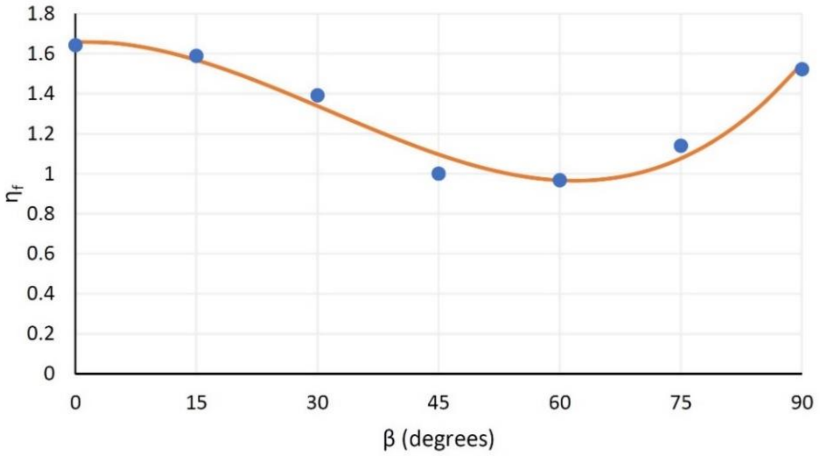

Fig 10b. Relation between the strength parameter η_f and β for μ_1 = 0.6 (third order approximation)

The proposed identification scheme can now be verified by examining the predictions of axial compressive strength at different confining pressures. Fig.11 shows the results for the confinements of (0, 5, 10, 15) MPa. The results correspond to μ_1 =0.6 and employ the third-order approximation with the set of coefficients as defined above. It is evident that the predictions are fairly consistent with the set of 'virtual data'. Again, a more accurate estimates can be obtained using a higher order approximation.

Finally, it should be pointed out that a conceptually similar methodology can be adopted for the purpose of identification of the dependence of spatial distribution of tensile strength f_t , eq.(13), on the volume fraction of constituents.

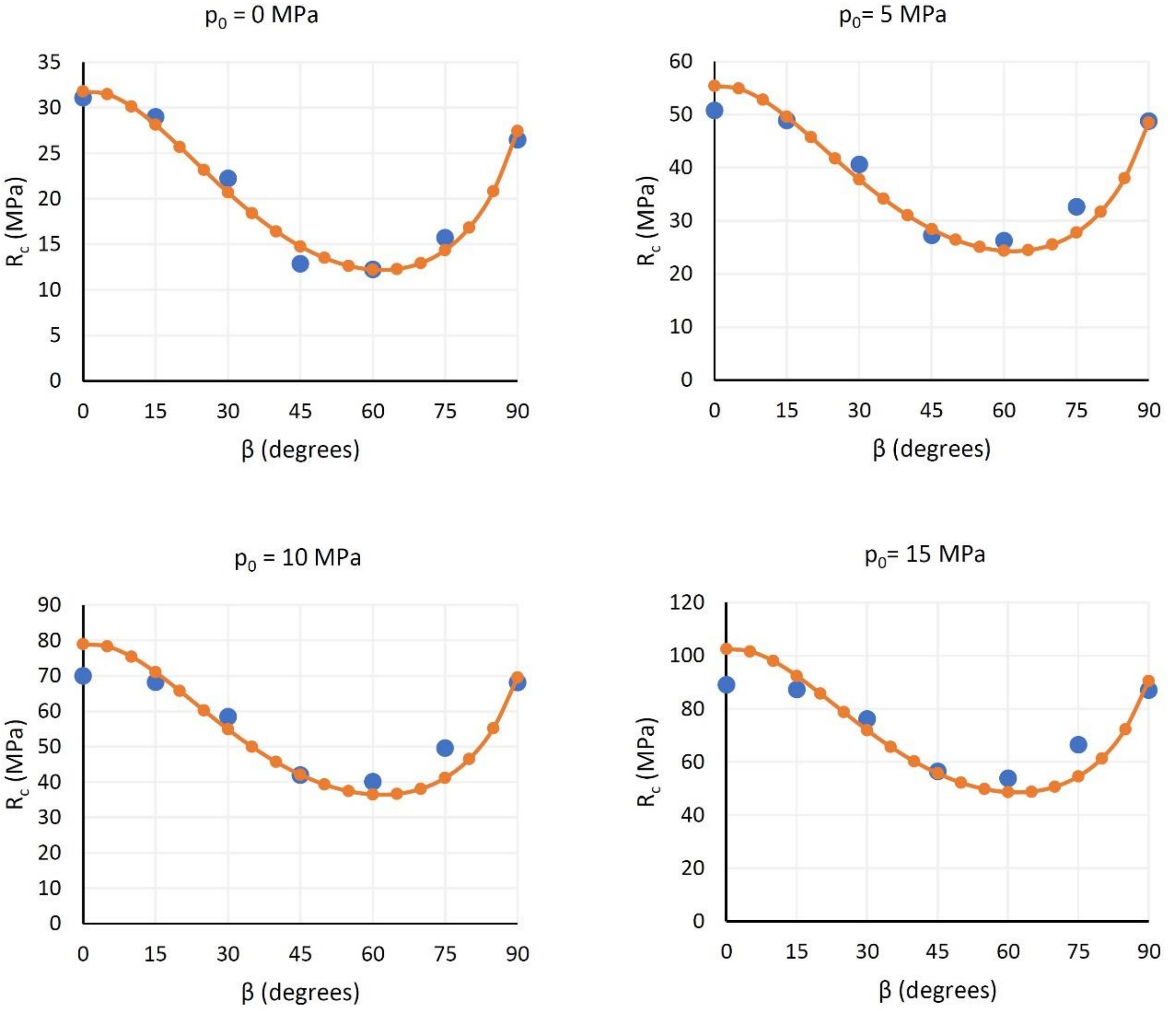

Fig 11. Variation of compressive strength R_c with bedding planes orientation β at different confining pressures (blue dots represent 'virtual data'; $\mu_1 = 0.6$)

4. Final remarks

This paper provides a framework for describing the conditions at failure in interbedded sedimentary rocks. The specific type of rock considered here is the Carpathian Flysch that consists of interchanging layers of claystone and sandstone with varying thickness. The large-scale analysis of such a rock formation requires a macroscopic approach which accounts for the inherent anisotropy of strength properties and their dependence on the volume fraction of constituent materials. It should be pointed that although the main focus here is on rocks, the proposed general methodology can also be applied to other stratified materials, such as wood and/or some multi-layered composites. There is a large volume of research in relation to development of failure criteria for laminated composites and an overview on this topic can be found, for example, in Ref.[13].

The formulation provided here employs the same functional form of the failure criteria at both meso and macroscale, the latter enhanced by incorporating the directional dependence of the strength parameters. In general, the identification of material functions/parameters requires a specifically designed experimental program that cannot be easily carried out given the limitations of the laboratory equipment in terms of the size of the sample as well as the imposed boundary conditions. Given those restrictions, the approach pursued here involves generation of a set of 'virtual data' obtained from FE analyses that provides the assessment of strength based on properties of constituents and their respective volume fractions. The mesoscale simulations conducted in this work incorporate an elastic-perfectly plastic idealization. Apparently, a more accurate representation of conditions at failure may be obtained by accounting for the onset and propagation of localized failure in both compression and tension regimes. At the same time, other simplified approaches may also be employed including, for example, a lower bound assessment [12]. It should be mentioned that the analysis carried out here incorporates an assumption of a perfect bonding between the constituents. Although the latter is rather restrictive, it seems that in case of Flysch the interfacial properties may not play a critical role in the evolution of damage. This is evidenced by laboratory tests which indicate that the failure pattern involves propagation of macrocracks through the entire specimen (e.g., [26]). This is contrast to the delamination mode which is typical for composite materials made from two or more constituents which have significantly different physical properties.

Given the set of data generated through mesoscale analysis, the material functions appearing in the continuum approach can be identified in a systematic manner. The procedure proposed here relies on the results of axial compression tests performed at different confining pressures, different orientation of sedimentary layers as well as different volume fractions of constituents. The 'virtual tests' in compression regime are supplemented by the simulations involving uniaxial tension. The specification of the strength descriptor $\eta_f(l_i)$, eq.(6), for a given value of volume fraction μ_1, involves a best-fit approximation that incorporates the results of all tests performed at various confinements. In case of rock formations with varying thickness of the interbedded sediments, a simplified procedure is proposed that employs only the results of *uniaxial* compression at different volume fractions and orientation of the layering.

The proposed continuum representation of the failure criterion as well as the methodology suggested for identification of the material functions have been verified against a broad range of the generated 'virtual data'. It has been demonstrated the basic trends in the variation of strength, in terms of spatial distribution as well as dependence on the volume fraction of constituents, can be predicted satisfactorily. Also, the quantitative aspects of these prediction appear to be quite reasonable.

Further research is required to examine the performance of the proposed phenomenological criterion for complex loading trajectories as well as its implementation in the analysis of practical geotechnical problems. The latter requires a constitutive relation that will address the evolution of deformation process. While in tension regime, the behaviour may be perceived as elastic-brittle, in compression range an inelastic framework (e.g. plasticity) should, in general, be employed. It is noted that the macroscopic failure criterion proposed here incorporates a standard invariant representation, so that the extension to plasticity is quite straightforward (cf. [20]).

References

1. Amadei B (1983). Rock anisotropy and the theory of stress measurements. Springer-Verlag, Berlin
2. Ambrose J (2014). Failure of anisotropic shales under triaxial stress conditions. PhD thesis, Imperial College London: Department of Earth Science and Engineering
3. Aubertin M, Li L, Simon R (2000). A multiaxial stress criterion for short- and long-term strength of isotropic rock media. Intern. Journ. Rock Mech. Min. Sci. 37: 1169-1193
4. Barla G (1974) Rock anisotropy - theory and laboratory testing. In: Mueller L. (ed) Rock Mechanics, Springer, Wien, pp. 131- 169
5. Boehler J.P, Sawczuk A (1977). On yielding of oriented solids. Acta Mech. 27: 185–204
6. Chen C.S, Pan E, Amadei B (1998). Determination of deformability and tensile strength of anisotropic rock using Brazilian tests. Intern. Journ. Rock Mech. Min. Sci. 35: 43-61
7. Duveau G, Shao J.F, Henry J.P (1998). Assessment of some failure criteria for strongly anisotropic geomaterials. Mech. Coh.-Frict. Mat. 3: 1–26
8. Hill R (1950). The mathematical theory of plasticity. Oxford University Press.
9. Hoek E, Brown E (1980). Empirical strength criterion for rock masses. Journ. Geotech. Eng. Div. ASCE. 106:1013–1035
10. Jaeger J.C (1960). Shear failure of anisotropic rocks. Geol. Mag. 97: 65-72
11. Liao J.J, Yang M.T, Hsieh H.Y (1997). Direct tensile behavior of a transversely isotropic rock, Intern. Journ. Rock Mech. Min. Sci. 34: 837-849

12. Lydzba D, Pietruszczak S, Shao J.F (2003). On anisotropy of stratified rocks: homogenization and fabric tensor approach. Computers and Geotechnics 30: 289–302
13. Matthews, F, Davies, G, Hitchings, D, Soutis, C (2000). Finite element modelling of composite materials and structures. Boca Raton: CRC Press
14. Nasseri M.H.B, Rao K.S, Ramamurthy T (2003). Anisotropic strength and deformational behavior of Himalayan schists. Intern. Journ. Rock Mech. Min. Sci. 40: 3-23
15. Niandou H, Shao J.F, Henry J.P, Fourmaintraux D (1997). Laboratory investigation of the mechanical behaviour of Tournemire shale. Intern. Journ. Rock Mech. Min. Sci. 34: 3-16
16. Nova R (1980). The failure of transversely isotropic rocks in triaxial compression. Intern. Journ. Rock Mech. Min. Sci. 17: 325–332
17. Paterson M.S, Wong T.F (2005). Experimental rock deformation – the brittle field. Springer-Verlag, Berlin
18. Pariseau W.G (1968). Plasticity theory for anisotropic rocks and soil. In: Proceedings 10th US Symp. Rock Mech., ARMA 68-0267
19. Pietruszczak S, Mroz Z (2001). On failure criteria for anisotropic cohesive-frictional materials. Intern. Journ. Numer. Anal. Meth. Geomech. 25: 509–524
20. Pietruszczak S, Lydzba D, Shao J.F (2002). Modelling of inherent anisotropy in sedimentary rocks. Intern. Journ. Solids Struct. 39: 637-648
21. Pietruszczak S, Oulapour M (1999). Assessment of dynamic stability of foundations on saturated sandy soils, Journ. Geotech. Eng. 125: 576-582
22. Saeidi O, Rasouli V, Vaneghi R.G, Gholami R, Torabi S.R (2014). A modified failure criterion for transversely isotropic rocks. Geosci. Frontiers 5: 215-225
23. Saroglou H, Tsiambaos G (2008). A modified Hoeke Brown failure criterion for transversely isotropic intact rock. Intern. Journ. Rock Mech. Min. Sci. 45: 223-234
24. Tien Y.M, Kuo M.C, Lu Xia-Ting Y.C (2017). Failure criteria for transversely isotropic rock. Rock Mech. Eng. 1: 451-477
25. Tyrus J.M, Gosz M, DeSantiago E (2007). A local finite element implementation for imposing periodic boundary conditions on composite micromechanical models. Intern. Journ. Solids Struct. 44: 2972-2989
26. Tziallas G.P, Saroglou H, Tsiabaos G (2013). Determination of mechanical properties of flysch using laboratory methods. Eng. Geology. 166: 81-89

27. Xia Z, Zhang Y, Ellyin F (2003). A unified periodical boundary conditions for representative volume elements of composites and applications. Intern. Journ. Solids Struct. 40: 1907-1921
28. Zhang G (2009). Rock failure with weak planes by self-locking concept. Intern. Journ. Rock Mech. Min. Sci. 46: 974-982

Chapter 3

On hydro-mechanical response of self-healing and self-sealing fractured geomaterials

Pietruszczak S, Przecherski P (2021). On hydro-mechanical response of self-healing and self-sealing fractured geomaterials. Computers and Geotechnics. 134:104030.

https://doi.org/10.1016/j.compgeo.2021.104030

On hydro-mechanical response of self-healing and self-sealing fractured geomaterials

S. Pietruszczak [1] & P. Przecherski [2]

[1] McMaster University, Hamilton, Ont., Canada

[2] Krakow University of Technology, Krakow, Poland

Abstract: The paper presents a methodology for describing the mechanical and hydraulic response of fractured geomaterials undergoing self-healing (i.e. recovery of strength/stiffness) and self-sealing (i.e. reduction of permeability). Regaining of strength and decrease in fracture transmissivity are particularly desirable in host rock as well as engineered barrier systems of deep geological repositories for disposal of low and intermediate-level nuclear waste. In this work, an enhanced continuum formulation is provided for describing the effects of fracture healing/sealing processes. Numerical examples are also given that illustrate both hydraulic and mechanical aspects of the proposed approach.

Keywords: embedded discontinuity, fracture, localization, self-healing

1. Introduction

The occurrence of self-sealing and self-healing processes is of a significant importance in geomechanics. This is particularly evident in the context of materials that are being considered for use as storage repositories for radioactive waste, compressed gasses, crude oil, etc. Self-sealing is the reduction of fracture permeability by any hydro-chemo-mechanical, or hydro-biochemical type of process. On the other hand, the self-healing typically refers to fracture sealing that is coupled with regaining of the material strength.

Self-healing is very common in cementitious materials. In this case, the widely studied mechanisms involve intrinsic self-healing attributed to ongoing hydration of cement particles, as well as precipitation of calcium carbonate inside the cracks [1,2,3,4]. Apart from autogenous healing, some engineered approaches have been implemented that include capsule based self-healing and/or vascular based healing. These techniques involve a release of healing agent in the region of damage, from either discrete capsules or through vascular channel systems [5,6]. Intrinsic self-healing effects are also present in various rock formations. For rock salt, for example, the damage healing characteristics have been extensively studied under different environmental and loading conditions (cf. [7]). The experimental evidence shows that 70-80% of original strength can be regained through a mechanism which involves pressure induced creep of asperities along the fracture surface leading to formation of an interlocking network [8]. The autogenous self-healing was also studied in argillaceous rocks, where a partial healing was typically observed (e.g. in Opalinus and Boom clay [9]). In general, there is no direct evidence of self-healing in crystalline rocks. However, the long-term heating may lead to formation of clay minerals in fractures, thereby clogging them [10]. Also, chemical processes and bacterial activities have the potential of decreasing permeability due to clogging of transported particles.

In terms of *self-sealing*, there is a considerable direct and indirect evidence that fluid-conductive rock fractures will, with the passage of time, seal [11, 12, 13, 14]. The autogenous self-sealing associated with reduction of fracture transmissivity, with no significant impact on strength, is fairly common in a wide variety of argillaceous soils and rocks (cf. [9, 15]). The process occurs at different rates which depend on the site-specific conditions such as the type of clay minerals, degree of induration and chemistry of the porewater. Typically, over a time span of one year, the permeability is reduced to 10^{-2} of its initial value. In general, the sealing process involving pressure solution and reprecipitation has been observed to be quite fast, i.e. of short duration relative to the repository performance period. At the same time, the creep related fracture sealing is much slower; it takes a number of decades for the permeability to recover to intact rock value and after that time the fracture traces can still be seen [10].

In addition to extensive laboratory and field investigations, the research has also been focused on numerical modeling of self-healing process. A comprehensive review of different methodologies is provided in refs. [16,17]. The majority of existing approaches involve extensions of classical continuum damage mechanics [18,19] to account for material’s ability to retrieve part of its mechanical properties during healing. Most of them are phenomenologically based and deal with different materials, like concrete [20], reinforced concrete [21], bone tissue [22], ceramics [23], asphalt mixtures [24], etc. Some of these approaches focus on a non-autogenous healing mechanism [25], whereas others deal with a specific type of autogenous healing process [21]. The research on modeling of self-healing in fractured rock formations is rather limited. Again, the main framework is that of continuum damage mechanics and the focus is primarily on the rock salt [26, 27].

The main limitation of the classical damage mechanics is its inability to deal with the effect of localized deformation. The framework can predict the onset of strain localization; however, it does not incorporate any internal length scale, which leads to a pathological mesh-dependency of the finite element solution. In order to remedy this, non-local approaches have been incorporated (cf. [28]). Although, numerically efficient, these approaches are rather ambiguous in terms of quantifying the notion of internal length; the latter is loosely interpreted as the 'size of material inhomogeneities' or that of 'the fracture process zone'. Furthermore, even the enhanced framework remains strictly phenomenological, i.e. it does not distinguish between the properties of the fractured and intact regions, which are significantly different. Alternative approaches for modeling of localized damage involve the use of interface elements as well as Extended Finite Element Method (XFEM) (cf. [29,30,31]). The interface elements are suitable for geometries involving pre-existing fractures; however, they cannot efficiently deal with propagation of damage. The XFEM approach, on the other hand, is very promising and has attracted increasing attention in various areas of engineering mechanics. Its main limitation is the computational inefficiency resulting from incorporation of additional degrees of freedom that account for the presence of discontinuities. A more in-depth review of different numerical strategies for dealing with discrete damage propagation can be found, for example, in ref. [32]).

In this work, the localized damage is described in terms of an embedded discontinuity approach, which incorporates volume averaging in order to define representative homogenized properties. The latter depend on properties of both constituents (i.e. in intact and fractured zone) and their geometric arrangement. As a result, an internal scale parameter is explicitly introduced that is defined as the ratio of the referential volume to the surface area of discontinuity (macrocrack) contained within this volume. The self-healing and self-sealing are described by introducing a scalar variable, which defines the kinetics of the process within the fractured zone. This variable is subsequently incorporated in a general continuum framework governing the mechanical/ hydraulic response at the macroscale.

2. Methodology

2.1. *Description of mechanics of self-healing fractured geomaterials*

The crack healing/sealing may be attained by an autogenous mechanism or by using biological, polymeric or chemical components. Assume that the progress in the underlying physical process is represented by a scalar parameter ζ which evolves with time (t) in such a way that $\zeta \to \bar{\zeta}$ for $t \to \infty$, where $\bar{\zeta}$ corresponds to a stationary state associated with thermodynamic equilibrium. The latter is typically considered as a function of confining pressure and the mathematical representation is chosen in such a way that $\bar{\zeta} \subset \langle 0,1 \rangle$, which implies $\zeta \subset \langle 0, \bar{\zeta} \rangle$. The kinetics of the process may be assumed in a linear form (cf. [28,33])

$$\dot{\zeta} = \gamma\left(\bar{\zeta} - \zeta\right) \;\Rightarrow\; \zeta = \bar{\zeta}\left(1 - \exp(-\gamma t)\right) \tag{1}$$

where γ is a parameter that defines the rate of the kinetics. It is noted that the latter may be affected by various external agencies a_α $(\alpha = 1,2...)$, such as temperature, humidity, etc. This can be accounted for by invoking the notion of a 'reaction time' t' that can be defined in the form $dt' = \varphi(a_\alpha)\, dt$, where $\varphi \in [0,1]$ and $\varphi = 1$ refers to ambient conditions.

It should be pointed out that the interpretation of parameter ζ will depend on the specific type of the physicochemical interaction involved. In this context, the evolution law (1) may be established by micromechanical considerations. An example of such an approach can be found in refs.[33,34], where a representation similar to eq.(1) was employed in the context of intergranular pressure solution (IPS) process in chalk that involves a dissolution at the intergranular contacts and a slow diffusion of the dissolved material. In that case ζ was interpreted as the normalized solid contact area of grains contained within a representative volume of the material. Thus, in general, the specific form of an evolution law (1) will depend on the underlying type of self-healing/sealing mechanism and the associated physical processes that occur within the pre-existing fracture.

In order to describe the mechanical interaction, assume that the constitutive law for the macrocrack relates the traction vector t_i to the displacement discontinuity g_i, while the material properties depend on ζ. Thus, in the elastic range there is

$$g_i = C^e_{ij} t_j \quad \Rightarrow \quad \dot{g}_i = C^e_{ij} \dot{t}_j + t_j \frac{\partial}{\partial \zeta} C^e_{ij} \dot{\zeta} \tag{2}$$

where C_{ij}^{e} is the compliance operator. Consider now the rate of energy due to self-healing continuing under a sustained load, i.e.

$$t_i \dot{g}_i = t_i \frac{\partial}{\partial \zeta} C_{ij}^{e} t_j \dot{\zeta} \tag{3}$$

Since $\dot{\zeta} > 0$ and $\frac{\partial}{\partial \zeta} C_{ij}^{e}$ is a *negative* definite operator, there is $t_i \dot{g}_i < 0$, i.e. the rate of energy dissipation becomes negative, which is not admissible in an irreversible process. Therefore, the formulation of the problem is assumed to invoke a *hypoelastic*-plastic idealization. In this case, in the *plastic* range there is

$$\dot{t}_i = K_{ij}^{e}\left(\dot{g}_j - \dot{g}_j^{p}\right); \qquad K_{ij}^{e} = K_{ij}^{e}(\zeta) \tag{4}$$

where

$$\dot{g}_i^{p} = \dot{\lambda} \frac{\partial Q}{\partial t_i}; \quad Q = Q(t_i, \zeta) = const; \quad f = \bar{f}(t_i, \zeta) + h(g_i^{p}) \tag{5}$$

while f and Q are the yield and plastic potential functions, respectively. The consistency condition now reads

$$\dot{f} = \frac{\partial f}{\partial t_i} \dot{t}_i + \frac{\partial f}{\partial g_i^{p}} \dot{\lambda} \frac{\partial Q}{\partial t_i} + \frac{\partial f}{\partial \zeta} \dot{\zeta} = 0 \tag{6}$$

so that

$$\dot{\lambda} = \frac{1}{H_p}\left(\frac{\partial f}{\partial t_i} \dot{t}_i + \frac{\partial f}{\partial \zeta} \dot{\zeta}\right); \qquad H_p = -\frac{\partial f}{\partial g_i^{p}} \frac{\partial Q}{\partial t_i} \tag{7}$$

In the equation above, H_p is the plastic modulus. It is noted that the irreversible deformation along the crack is associated with strain-softening, so that $H_p < 0$. In this case, the loading-unloading criteria can be postulated in the general form

$$\begin{aligned} &\text{Active loading:} \quad f = 0 \wedge \dot{\bar{f}}^{*} > 0; \quad \dot{\bar{f}}^{*} = \frac{\partial f}{\partial t_i} K_{ij}^{e} \dot{g}_j + \frac{\partial f}{\partial \zeta} \dot{\zeta} \\ &\text{Unloading:} \qquad f < 0 \ \text{ or } \ f = 0 \wedge \dot{\bar{f}}^{*} < 0 \end{aligned} \tag{8}$$

which is an extension of that discussed in ref. [35]. Apparently, when $\dot{\zeta} \to 0$, the classical loading condition for a strain-softening material is recovered. On the other hand, when the load is stationary (i.e. $f = 0,\ \dot{t}_i = 0$), there is $\dot{\bar{f}}^* < 0$ which implies an elastic response under self-healing conditions. In general, however, the loading-unloading criterion is affected by both the rate of kinetics of self-healing and the induced stress rate.

For an active loading case, when the velocity discontinuities are prescribed, substitution of eq. (4) into eq.(7), gives

$$\dot{\lambda} = \frac{1}{H}\left(\frac{\partial f}{\partial t_i} K^e_{ij} \dot{g}_j + \frac{\partial f}{\partial \zeta}\dot{\zeta}\right); \qquad H = H_e + H_p\,,\ H_e = \frac{\partial f}{\partial t_i} K^e_{ij} \frac{\partial Q}{\partial t_j} \tag{9}$$

which leads to the constitutive relation in the form

$$\dot{t}_i = K_{ij}\,\dot{g}_j - b_i\,\dot{\zeta}\,; \qquad K_{ij} = K^e_{ij} - \frac{1}{H} K^e_{ip} \frac{\partial Q}{\partial t_p} \frac{\partial f}{\partial t_q} K^e_{qj}\,; \quad b_i = \frac{1}{H} K^e_{ij} \frac{\partial Q}{\partial t_j} \frac{\partial f}{\partial \zeta} \tag{10}$$

where K_{ij} is the elastoplastic stiffness operator.

Consider now the mechanical behaviour within a referential volume $\Delta\Omega$ adjacent to the fractured region with the surface area $\Delta\Gamma$. Following the embedded discontinuity approach, as introduced in ref. [36], the average strain rate in a domain intercepted by a discrete fracture can be defined as

$$\dot{\varepsilon}_{ij} = \dot{\varepsilon}^{(1)}_{ij} + \chi\left(e^{(n)}_i \dot{g}_j\right)^s; \quad \chi = \Delta\Gamma/\Delta\Omega\,, \quad \left(e^{(n)}_i \dot{g}_j\right)^s = \left(e^{(n)}_i \dot{g}_j + e^{(n)}_j \dot{g}_i\right)/2 \tag{11}$$

where χ^{-1} is an internal scale parameter, $e^{(n)}_i$ is the unit normal to the fracture and the superscript (1) refers to the intact domain. Imposing the continuity of traction, i.e.

$$\dot{t}_i = \dot{\sigma}^{(1)}_{ij} e^{(n)}_i\,; \quad \dot{\sigma}^{(1)}_{ij} \simeq \dot{\sigma}_{ij} = D_{ijkl}\dot{\varepsilon}^{(1)}_{kl} \tag{12}$$

and invoking the constitutive relation (10) leads, after some algebraic manipulation, to the localization law in the form

$$\dot{g}_i = E_{ip} D_{pqjk} e^{(n)}_q \dot{\varepsilon}_{jk} + E_{ij} b_j \dot{\zeta}\,; \qquad E_{ij} = \left(K_{ij} + \chi D^e_{ipqj} e^{(n)}_p e^{(n)}_q\right)^{-1} \tag{13}$$

Given now the representation above, the macroscopic stress rate can be defined as

$$\dot{\sigma}_{ij} = D^H_{ijkl}\dot{\varepsilon}_{kl} - \chi D_{ijkl}\, e^{(n)}_k E_{lp} b_p \dot{\zeta}\,; \qquad D^H_{ijkl} = D_{ijpq}\left(\delta_{pk}\delta_{ql} - \chi e^{(n)}_p E_{qr} D_{rjkl} e^{(n)}_j\right) \tag{14}$$

The above equation represents the constitutive law with embedded discontinuity (CLED), which defines the mechanical response of a material intercepted by a macrocrack that undergoes a progressive healing in the course of loading. Apparently, when $\dot{\zeta} \to 0$, the CLED formulation presented in refs. [32,36] is recovered.

2.2. Description of flow in self-sealing geomaterials

The approach employed here is an extension of the methodology recently proposed in ref. [37]. The main assumption is that the presence of fracture results in a weak discontinuity in the fluid pressure p. In this case, the average value of the pressure gradient in the referential volume $\Delta\Omega$ is defined as

$$p_{,i} = (1-\mu)\, p_{,i}^{(1)} + \mu p_{,i}^{(2)} \;;\quad \mu = \chi t_d \tag{15}$$

subject to constraints

$$e_i^{(t)} p_{,i}^{(1)} = e_i^{(t)} p_{,i}^{(2)}, \quad e_i^{(s)} p_{,i}^{(1)} = e_i^{(s)} p_{,i}^{(2)} \tag{16}$$

where $e_i^{(t)}$, $e_i^{(s)}$ are the base vectors along the fracture and t_d is the fracture aperture.

The average superficial velocity of fluid flow w_i in both constituents is governed by Darcy's law, so that

$$w_i^{(\alpha)} = \frac{1}{\rho_f \mathrm{g}} k_{ij}^{(\alpha)} \left(-p_{,j}^{(\alpha)} + \rho_f \mathrm{g}_j \right) = \frac{1}{\rho_f \mathrm{g}} k_{ij}^{(\alpha)} h_j^{(\alpha)} \;;\quad \alpha = 1,2\,,\quad k_{ij}^{(2)} = k_{ij}^{(2)}(\zeta) \tag{17}$$

where ρ_f is the fluid's intrinsic density, g is the acceleration due to gravity and $k_{ij}^{(1)}$, $k_{ij}^{(2)}$ are the hydraulic conductivity tensors in the intact and fractured regions, respectively. The autogenous self-sealing in fault systems in rocks is usually associated with chemical action, i.e. dissolution of minerals and their precipitation in veins. The kinetics of sealing may again be described by a linear form analogous to eq.(1), in which the rate of the process is said to be affected by the temperature, solubility and the diffusion properties. Within the framework presented here, the effect of self-sealing is embedded in the evolution law for the hydraulic conductivity tensor appearing in eq. (17), i.e. $k_{ij}^{(2)} = k_{ij}^{(2)}(\zeta)$.

By subtracting the body force $\rho_f g_i$ from both sides of eq.(15), the operator h_i, which is proportional to the average hydraulic gradient, can now be expressed in a functional form similar to that of representation (15)-(16), i.e.

$$h_i = (1-\mu)\, h_i^{(1)} + \mu\, h_i^{(2)}, \qquad s.\,t. \quad e_i^{(t)} h_i^{(1)} = e_i^{(t)} h_i^{(2)}, \quad e_i^{(s)} h_i^{(1)} = e_i^{(s)} h_i^{(2)} \tag{18}$$

A similar approximation may be obtained for the average flow velocity w_i. Thus,

$$w_i = (1-\mu)\, w_i^{(1)} + \mu\, w_i^{(2)}, \qquad s.\,t. \quad e_i^{(n)} w_i^{(1)} = e_i^{(n)} w_i^{(2)} \tag{19}$$

It is noted that the constraints in eqs. (18) and (19) are analogous to those used for describing the flow through a layered porous medium. They imply the existence of discontinuity in the normal component of hydraulic gradient as well in the tangential components of superficial velocity.

Combining now the constraints in eqs. (18) and (19) with Darcy's law leads to)

$$h_i^{(2)} = c_{ij}\, h_i^{(1)}\ ; \qquad c_{ij} = \begin{bmatrix} e_i^{(t)} \\ k_{ij}^{(2)} e_j^{(n)} \\ e_i^{(s)} \end{bmatrix}^{-1} \begin{bmatrix} e_i^{(t)} \\ k_{ij}^{(1)} e_j^{(n)} \\ e_i^{(s)} \end{bmatrix} \tag{20}$$

so that, after rearranging, the following localization law is obtained

$$h_i^{(1)} = S_{ij}\, h_j\ ; \qquad S_{ij} = \left[\delta_{ij} + \mu\left(c_{ij} - \delta_{ij}\right)\right]^{-1} \tag{21}$$

Finally, given eqs. (17), (19) and (21) an enriched form of Darcy's law, which incorporates the internal scale parameter, is obtained, viz.

$$w_i = \frac{1}{\rho_f g} \bar{k}_{ij}\left(-p_{,j} + \rho_f g_j\right); \qquad \bar{k}_{ij} = \bar{k}_{ij}(\zeta) = \left((1-\mu)\, k_{iq}^{(1)} + \mu\, k_{ip}^{(2)}\, c_{pq}\right) S_{qj} \tag{22}$$

As shown in ref.[37], since both $k_{ij}^{(1)}$ and $k_{ij}^{(2)}$ are symmetric operators, $\bar{k}_{ij}$ is also a *symmetric* second-order tensor.

The hydraulic conductivity tensor $k_{ij}^{(2)} = k_{ij}^{(2)}(\zeta)$, may be defined using its spectral decomposition, i.e.

$$k_{ij}^{(2)} = k_{tt} e_i^{(t)} e_j^{(t)} + k_{nn} e_i^{(n)} e_j^{(n)} + k_{tt} e_i^{(s)} e_j^{(s)} \tag{23}$$

where k_{tt}, k_{nn} are the eigenvalues of $k_{ij}^{(2)}$. For the fracture region, the most commonly used approximation involves the assumption of laminar flow in which the longitudinal transmissivity k_{tt} is defined as an explicit function of the aperture t_d [38]. Thus, the self-sealing is described here through a simple linear approximation

$$k_{tt} = (1-\zeta)\frac{g}{12\vartheta}t_d^2, \qquad k_{nn} = const. \tag{24}$$

where $k_{nn} \ll k_{tt}\big|_{\zeta=0}$.

The evolution law for the equivalent conductivity tensor $\bar{k}_{ij}$ may now be expressed in the form

$$\dot{\bar{k}}_{ij} = \frac{\partial}{\partial\zeta}\bar{k}_{ij}\dot{\zeta} \tag{25}$$

In order to evaluate the term $\partial\bar{k}_{ij} / \partial\zeta$ note that both $k_{ij}^{(1)}$ as well as the normal component of hydraulic conductivity in the fractured zone, i.e. $e_i^{(n)}e_j^{(n)}k_{ij}^{(2)}$, are independent of ζ, eq. (24). Thus, $\partial c_{ij} / \partial\zeta = 0$ and, in view of eq.(22), there is

$$\frac{\partial}{\partial\zeta}\bar{k}_{ij} = \mu\, c_{pq}\, S_{qj}\,\frac{\partial}{\partial\zeta}k_{ip}^{(2)} \tag{26}$$

where, according to the spectral decomposition (23)

$$\frac{\partial}{\partial\zeta}k_{ij}^{(2)} = \frac{\partial}{\partial\zeta}k_{tt}\left(e_i^{(t)}e_j^{(t)} + e_i^{(s)}e_j^{(s)}\right) = -\left(\frac{g}{12\vartheta}t_d^2\right)\left(\delta_{ij} - e_i^{(n)}e_j^{(n)}\right) \tag{27}$$

Thus, the final form of the evolution law becomes

$$\dot{\bar{k}}_{ij} = -\left(\frac{g}{12\vartheta}t_d^2\right)c_{pq}\, S_{qj}\left(\delta_{ip} - e_i^{(n)}e_p^{(n)}\right)\dot{\zeta} \tag{28}$$

The above equation describes the time-dependent reduction in the equivalent conductivity resulting from the ongoing self-sealing process within the fractured region.

3. Numerical examples

3.2. Self-sealing capacity of a macro-fractured sample of Opalinus Clay

An illustrative example provided here involves simulation of a fluid flow through a rock sample which contains a pre-defined discrete fracture network. The example is heuristic; however, the hydraulic properties are representative of Opalinus Clay specimens from Mont Terri. The hydraulic conductivity of the intact rock is in the range of 10^{-13} m/s, while that derived from flow measurements just after the fracturing is about 10^{-8} m/s (cf. ref. [39]). The latter is consistent with the values reported in the excavation-disturbed zone at Mont Terri [40]. Based on the experimental evidence, there is a slow autogenous fracture sealing in Opalinus Clay, with the kinetics of the process affected by the interstitial water chemistry. The results of the long-term in situ sealing experiments indicate that a complete hydraulic sealing can in fact be achieved [39].

The geometry of the problem is shown in Fig.1. The 2D flow region $1\times1\mathrm{m}$ contains a discrete fracture network in which some of the cracks penetrate the external boundaries. The boundary conditions are defined in terms of the fluid pressure. The top and bottom surfaces have a constant pressure of p=10MPa and p=0, respectively, while the vertical boundaries are subjected to a linear variation of fluid pressure from 10 MPa to zero. Thus, for a homogeneous material the hydraulic gradient is constant within the domain and it is coaxial with vertical y-axis, which implies a vertical flow. However, for the fractured region the flow is two-dimensional and strongly depends on the geometry of the fractures.

The finite element discretization of the domain is shown in Fig. 1b. Since the proposed approach explicitly incorporates an internal scale parameter χ^{-1}, the solution does not display a pathological mesh dependency [37]. In view of this, a simple *structured* mesh has been employed consisting of 10,000 quadrilateral isoparametric elements. The elements containing a pre-existing fracture have been assigned the enriched form of Darcy's law, eq.(22). The corresponding values of χ in these elements were determined based on the geometry of mesh and the fracture network. In elements comprising intersecting fractures, a two- stage homogenization has been employed. In this case, the equivalent hydraulic conductivity operator $\overline{k}_{ij}$ was evaluated first for a single fracture and then identified with $k_{ij}^{(1)}$ for the second-stage averaging based on eq. (22).

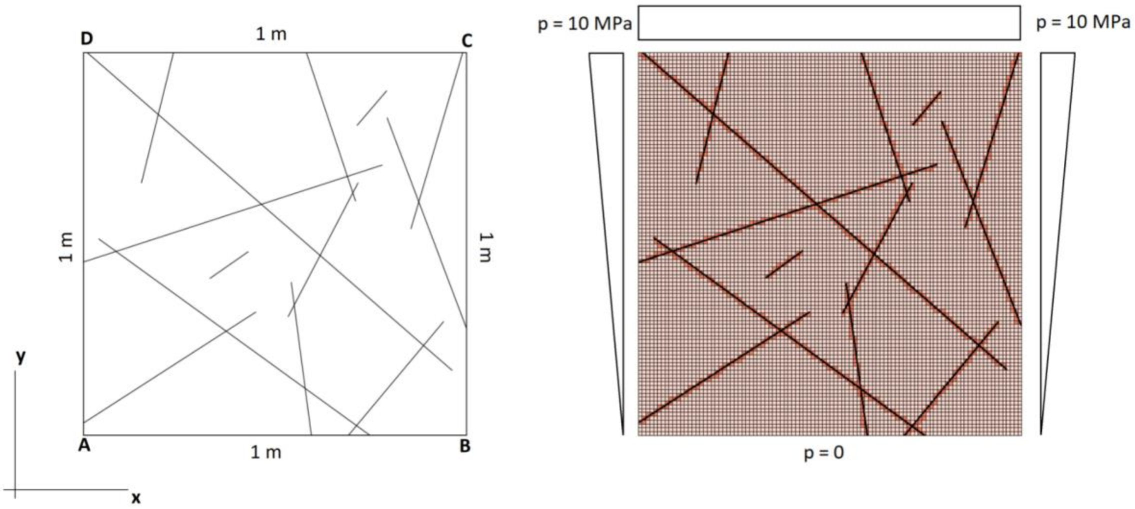

Fig.1. Geometry of the flow domain and the finite element discretization

Fig.2 presents a time history of the hydraulic conductivity in Opalinus clay specimens as reported in ref. [39]. The experiments included an assessment of the long-term sealing capacity of the fractures. For the intact sample, the average value of hydraulic conductivity is approx. 10^{-13}m/s. Immediately after a localized tensile fracturing of the sample, a significant increase in the volume of flow is observed and the conductivity increases by several orders of magnitude (up to approx. 10^{-8} m/s). During the autogenous self-sealing, under a constant confinement, the fracture transmissivity progressively decreases. The laboratory measurements are shown by the blue dots in Fig.2. As indicated in this figure, after approx. 240 days the reported hydraulic conductivity reduces to approx. 10^{-11} m/s.

Given the information in Fig.2, the parameter γ governing the rate of kinetics, eq.(1), may be estimated. Noting that the increase in conductivity after the onset of fracture is primarily due to the flow through the crack, the fracture aperture was evaluated directly from eq.(24), as t_d $\approx 12\mu$m. At the same time, the linear approximation (in logarithmic scale) to experimental data in Fig.2 yields $\gamma = 0.025$ (1/day).

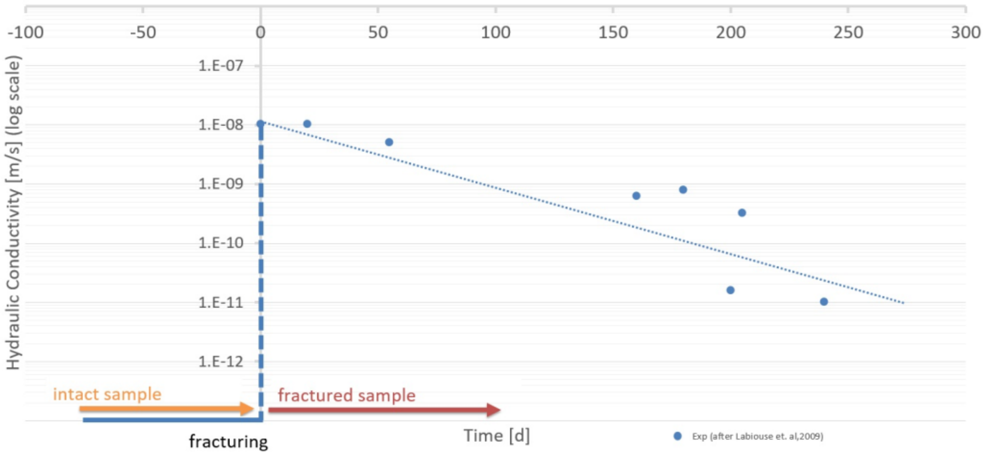

Fig.2. Evolution of hydraulic conductivity with time in fractured Opalinus Clay samples (experimental data after ref. [39])

The main results of numerical simulations are provided in Fig. 3-4. Fig.3 shows the fluid velocity distribution within the fractured domain at different time intervals. The latter include t=0 (prior to self-sealing), t = 275 days (conductivity of 10^{-11} m/s in the numerical approximation) and $t \rightarrow \infty$, i.e. when cracks are completely sealed. It is evident that initially the primary mechanism is the transport through the fractures, which evolves as the self-sealing progresses. When fractures become completely sealed, the flow occurs through the intact rock and it is concentrated near the vertical boundaries. Fig. 3 also includes the surface profiles of the normal component of Darcy's velocity. The evolution of the volume of flow is given in Table 1. In the intact sample the flow is vertical, and the rate of discharge is very low (10^{-8} (m^2/s)/m). For the fractured sample, at (t=0), the volume of flow increases by several orders of magnitude and has a similar intensity along all boundaries. As the self-sealing commences, the out-flow progressively decreases. When the fractures are completely sealed, the volume of flow is an order of magnitude smaller than that in the virgin (intact) sample.

(a)

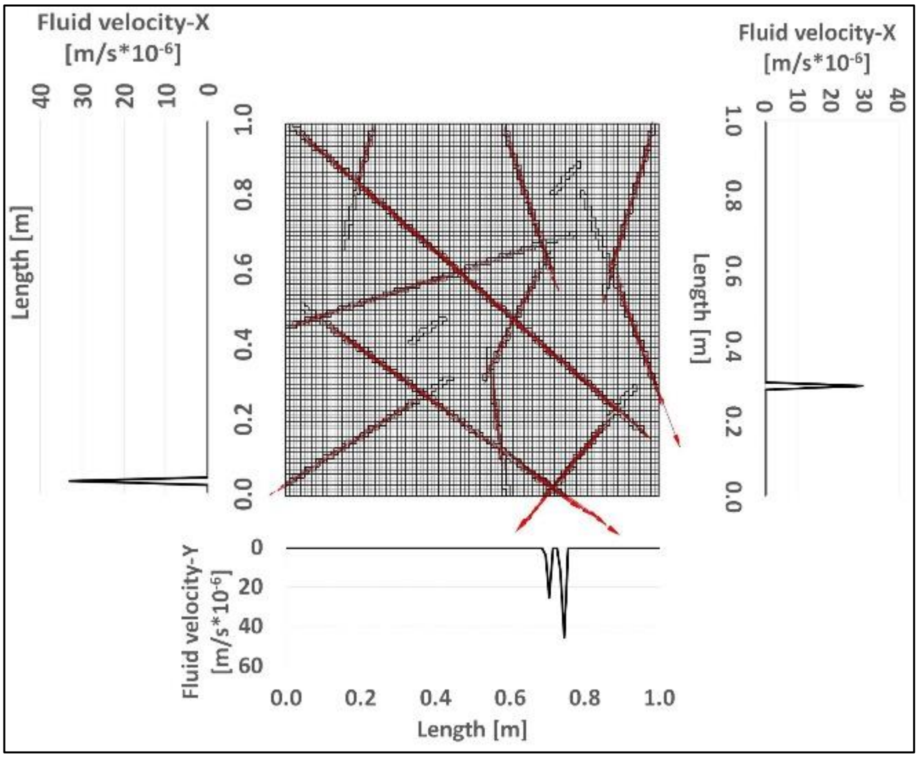
Fluid velocity-X
[m/s*10-6]
40
30
20
10
0
Length [m]
0.0
0.2
0.4
0.6
0.8
1.0
Fluid velocity-X
[m/s*10-6]
0
10
20
30
40
1.0
0.8
0.6
0.4
0.2
0.0
Length [m]
Fluid velocity-Y
[m/s*10-6]
0
20
40
60
0.0
0.2
0.4
0.6
0.8
1.0
Length [m]

(b)

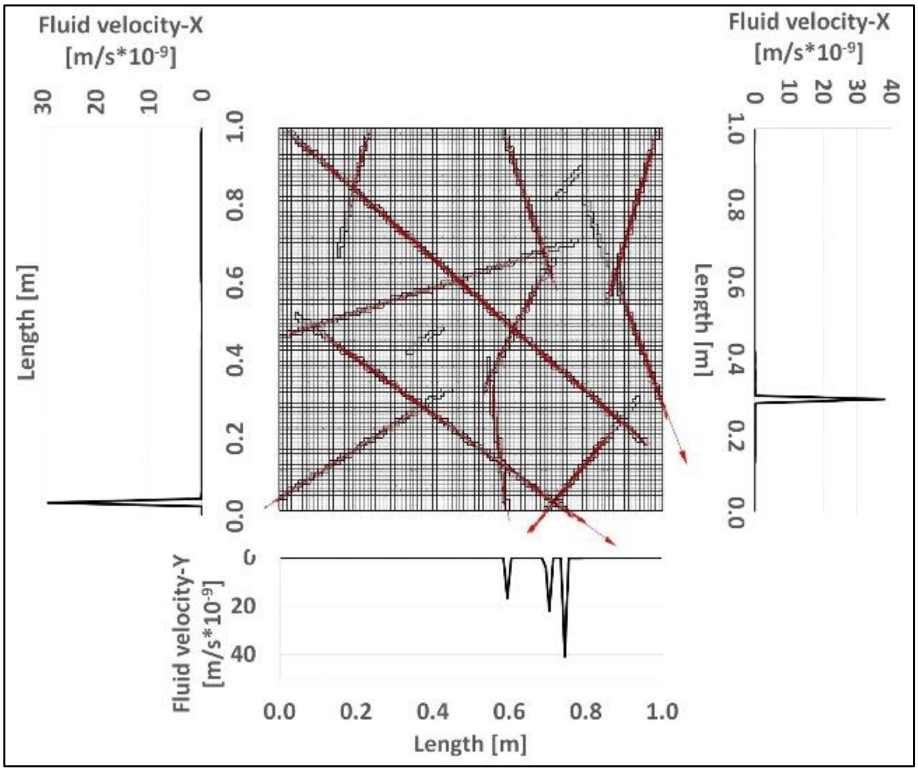
Fluid velocity-X
[m/s*10-9]
30
20
10
0
Length [m]
0.0
0.2
0.4
0.6
0.8
1.0
Fluid velocity-X
[m/s*10-9]
0
10
20
30
40
1.0
0.8
0.6
0.4
0.2
0.0
Length [m]
Fluid velocity-Y
[m/s*10-9]
0
20
40
0.0
0.2
0.4
0.6
0.8
1.0
Length [m]

(c)

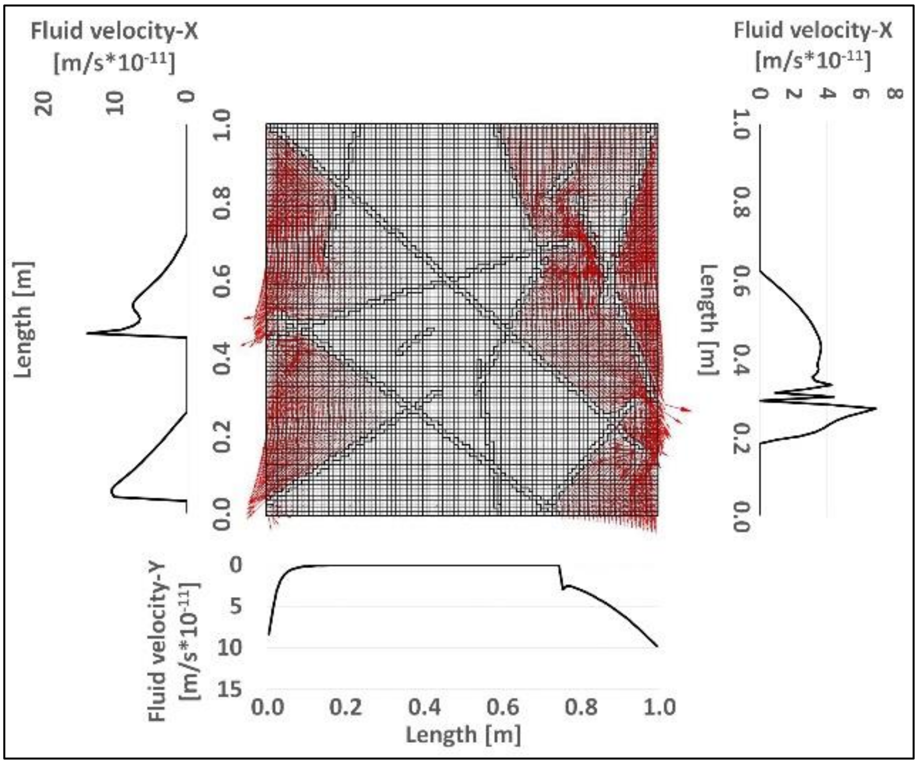

Fig. 3. Velocity field within the fractured domain (including the surface profiles) at different time intervals: (a) $t = 0$, (b) $t = 275$ days, (c) $t \rightarrow \infty$

Table 1. Evolution of the out-flow discharge from external boundaries

Volume of flow (Q) $[m^2/s]/m$	Bottom boundary AB	Right boundary BC	Left boundary AD
Intact sample	1.00E-08	-	-
Q($t = 0$)	6.83E-05	1.13E-06	3.76E-05
Q($t = 275\ days$)	8.92E-08	4.84E-09	5.12E-08
Q($t \rightarrow \infty$)	1.57E-09	1.28E-09	2.54E-09

Finally, Fig. 4 shows the distribution of fluid pressure within the domain. Again, for the intact sample a classical one-dimensional solution is obtained. As the self-sealing continues, the distribution progressively evolves and for sealed cracks the highest fluid pressures occur near the top and vertical boundaries.

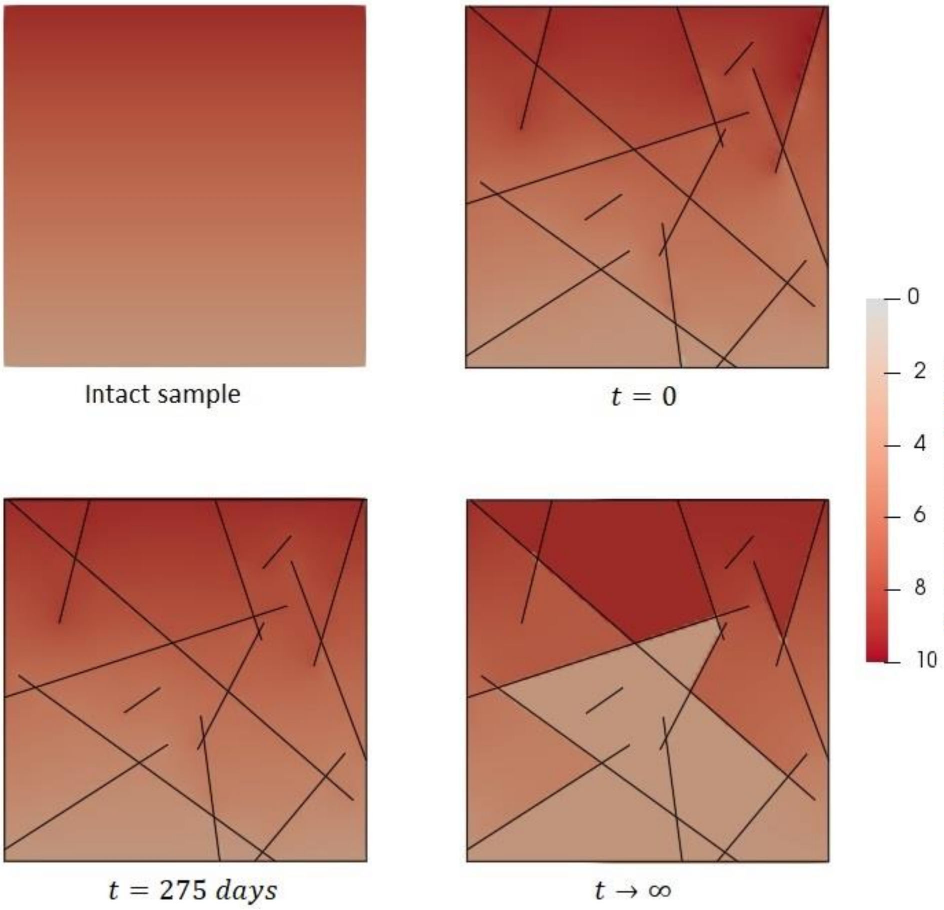

Fig. 4. Pore-fluid pressure distribution in the intact and fractured material at different stages of the self-sealing process

The example provided above, although purely exploratory, shows the ability of the proposed framework to model the basic trends in the hydraulic response in the presence of a self-sealing fracture network. The approach is numerically very efficient and can be easily implemented in a standard FE code. The analysis does not require any special type of elements (e.g. interface elements) and can be conducted using a simple structured mesh.

3.2. Self-healing in geomaterials with pre-existing fractures

The example provided in this section involves simulation of mechanical response of a sample of cohesive-frictional geomaterial containing pre-existing fractures subjected to self-healing process. The experimental data pertaining to assessment of strength in the absence of self-healing is taken from ref. [41]. The synthetic rock samples tested in that work were a mixture of Portland cement (approx. 30% by weight), dry river sand (60%) and water. The joints were formed during the sample preparation procedure, prior to curing the mixture. The numerical simulations reported here were conducted for one specific fracture pattern involving the presence of two cracks, one with 30^0 and the other with 60^0 dip angles with respect to horizontal.

Fig. 5a shows the geometry of the problem and the finite element discretization. Once again, a simple structured mesh was employed, which incorporated 8-noded hexahedral elements. The bottom surface was fixed in the vertical direction, and the out-of-plane nodes along the centre line of this surface were also constrained against the horizontal movement. The loading process consisted of applying the vertical displacements at the top surface. The intact material was assumed to be elastic with the conditions at failure governed by the standard Mohr-Coulomb criterion. For the elements containing the pre-existing cracks, the constitutive relation (14) was employed, in which the response along the crack was described using an elastoplastic strain-softening idealization. In this case, referring the problem to a local coordinate system attached to the crack surface, the yield function was taken as

$$f=\tau+\eta\sigma-c=0;\quad \eta=\eta(\kappa,\zeta),\quad c=c(\zeta) \tag{29}$$

The softening parameter κ was identified with the tangential component of plastic part of velocity discontinuity and the material functions η, c were selected as

$$\eta=\eta_r+(\bar{\eta}-\eta_r)e^{-\beta\kappa};\ \ \bar{\eta}=\eta_0(1+a_1\zeta);\ \ c=c_0(1+a_2\zeta) \tag{30}$$

Here, η_0, c_0 are the values of the friction coefficient and cohesion at which the transition to softening occurs, η_r is the residual value of η, and β, a_1, a_2 are material constants which govern the stiffness in the softening regime and the kinetics of the self-healing, respectively. Based on the information provided in ref. [41], the following mechanical properties were assigned

Fractured region: $K_n=20\,\text{GPa/m},\ K_t=5\,\text{GPa/m},\ \eta_0=0.73,\ \eta_r=0.40,\ c=3.2\,\text{MPa},\ \beta=100\,\text{m}^{-1}$

Intact material: $E=20\,\text{GPa},\ \nu=0.2,\ \eta_0=0.84,\ c_0=11\,MPa$

where K_n, K_t are the elastic stiffness coefficients. Furthermore, the time-scale for the kinetics of the self-healing was assumed to be within a range of 365 days, while the parameters a_1, a_2 were selected in such a way that for $\zeta\rightarrow 1$, the friction coefficient and cohesion approach the values assigned to the intact material. Thus,

$$\gamma=\ 0.01\,(1/\text{day}),\ a_1=0.15\,,\ a_2=2.40$$

Finally, both elastic stiffness moduli K_n, K_t were assumed to increase by a factor of 10 in the course of self-healing.

The main results of the numerical analysis are presented in Figs. 5-8. The first stage of analysis involved simulation of an axial compression test conducted prior to the onset of the fracture healing. The predicted failure mode, Fig. 5b, includes activation of the fracture with the 60^0 dip angle (shown in dark red) without engaging the other pre-existing crack. Fig.6 shows the predicted average stress-strain curve. The ultimate stress is in the range of 13 MPa, which is significantly lower than the strength of the intact material (approx. 47 MPa).

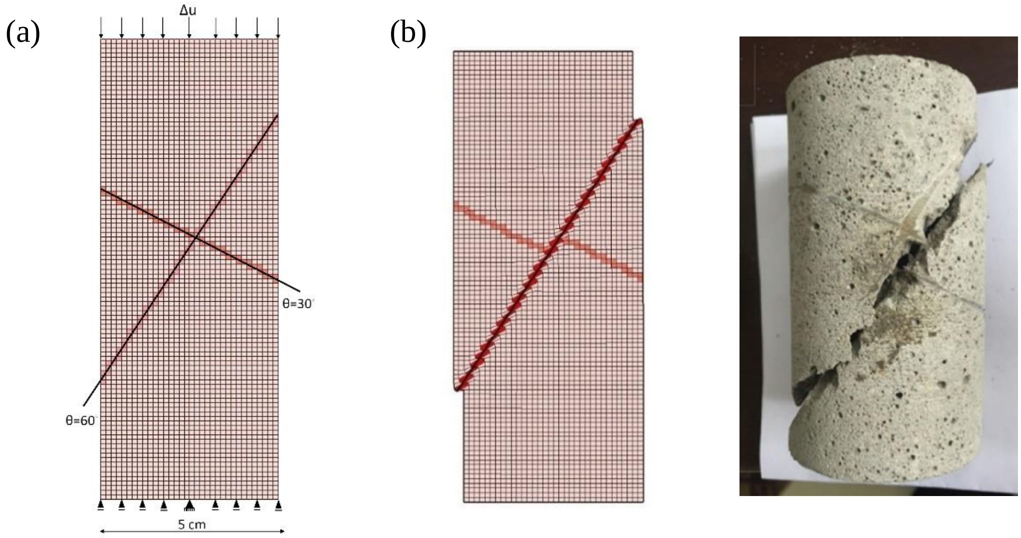

Fig. 5. (a) Geometry and finite element discretization; (b) comparison of fracture mode with experimental data [41]

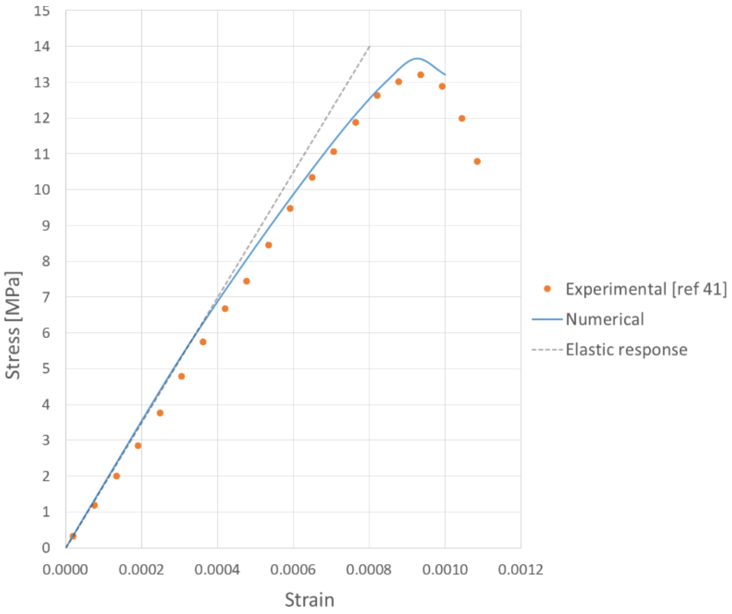

Fig. 6. Average stress-strain curve for axial compression

The subsequent figure, i.e. Fig. 7, depicts the effect of self-healing. The loading history involves an increase in vertical displacement up to a stage when the entire crack experiences irreversible deformation (average axial stress of 12.8 MPa). This is followed be a period of self-healing (100 days and 365 days) at the sustained load, after which the imposed displacement is further increased up to failure. Fig. 7a shows the time history of the resultant force for both healing scenarios, while Fig. 7b gives the corresponding average stress-strain curve. It is evident that the strength progressively increases with the healing time; after 365 days of continuing healing the ultimate stress reaches over 42 MPa. It needs to be pointed out that the example given here is largely illustrative, as there is no experimental data available; however, the qualitative trends appear to be rational.

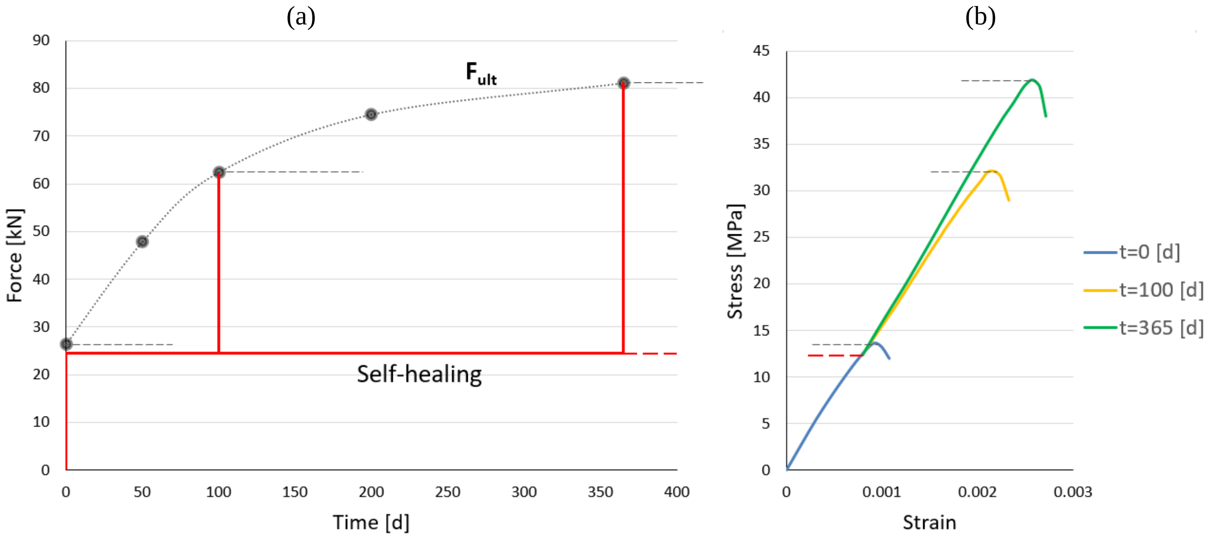

Fig. 7. (a) Time history of the resultant force; (b) the corresponding average stress-strain diagrams

Finally, Fig.8 shows the results for the scenario when the fracture-healing is coupled with continuing mechanical loading. The first stage of the loading sequence is analogous to that considered before, i.e. an instantaneous (compared to the time-scale of self-healing) increase in vertical displacement is applied up to 0.12mm, which generates average axial stress of 12.8 MPa. Subsequently, different average axial strain rates are imposed ranging from $0.9*10^{-5}$/day up to $0.2*10^{-3}$/day. In this case, the rates of loading are sufficiently low so that both phenomena, i.e. irreversible deformation and self-healing, can occur simultaneously. Fig. 8a shows the history of imposed vertical displacement u(mm) in relation to the evolution of parameter ζ that governs the kinetics of healing, eq.(1). At the same time, Fig. 8b depicts the average stress-strain characteristics for different strain rates. It is evident that at very low rates, e.g. $0.9*10^{-5}$/day, the healing process is dominant resulting in a significant increase in compressive strength and ductility. On the other hand, for faster loading rates the healing action is slower, implying a reduction in strength and a more brittle response.

Again, the numerical examples provided in Figs. 7-8 above are largely exploratory; however, they demonstrate the ability of the proposed framework to model the mechanical effects of continuing self-healing. The predicted qualitative trends are rational; however, the quantitative assessment requires an appropriate experimental verification.

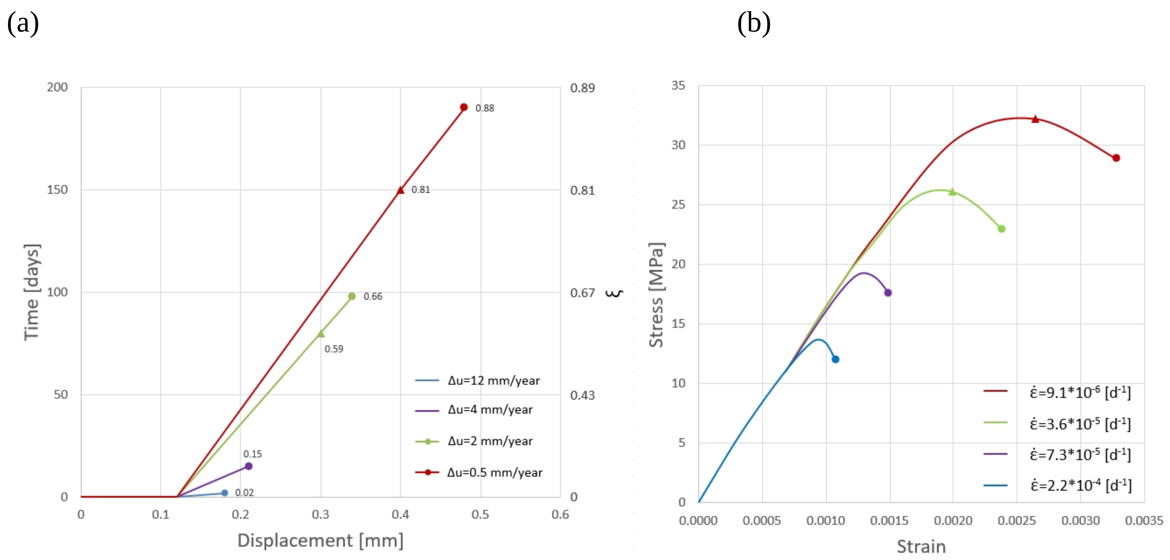

Fig. 8. (a) Time history of prescribed displacements; (b) the corresponding average stress-strain curves for different loading rates

4. Concluding remarks

The work presented here focussed on development of methodologies for describing the effects of self-sealing and self-healing in geomaterials. The kinetics of the process has been defined by invoking a scalar parameter, whose evolution is time-dependent and may be affected by various external agencies, such as temperature, humidity, chemical/biological environment, etc. The self-healing process was described by employing a hypoelastic-plastic idealization for the fractured zone in which the mechanical properties evolve in the course of continuing healing. The upscaling from meso to macroscale employed an embedded discontinuity approach incorporating an internal scale parameter associated with the presence of discontinuities. The effects of self-healing phenomenon were described using a variant of the embedded discontinuity framework incorporating a weak discontinuity in the fluid pressure. Within this methodology, an enriched form of Darcy's law is derived which employs an equivalent hydraulic conductivity, which is a symmetric second order tensor [37]. The effect of self-healing was embedded in the evolution law for the hydraulic properties within the fracture region. The proposed approach incorporated a spectral decomposition of the fracture transmissivity operator and related its evolution to the variable governing the kinetics of the process.

Two numerical examples have been provided to illustrate the proposed methodology. The first involved simulation of fluid flow through a sample comprising an intact material and a discrete fracture network. The hydraulic properties, including the rate of kinetics of self-sealing, were representative of Opalinus clay. The qualitative trends, in terms of evolution of fluid-velocity field and the out-flow discharge, were predicted in a quite rational way. However, in order to assess the quantitative response, further studies are required which would involve a verification against the actual experimental data. Unfortunately, to authors' knowledge, there is no comprehensive study in this respect currently available in the literature. The second example that was provided illustrated the mechanical response of a specimen subjected to self-healing process. Again, this was a heuristic example that depicted the qualitative trends in the time-dependent evolution of strength. The only experimental data available and used here was that pertaining to the average stress-strain response in the absence of healing.

It should be emphasized that this is a preliminary work which was focused on proposing a methodology for describing the mechanical/hydraulic effects of self-healing and self-sealing processes. The illustrative examples given did not involve the coupled conditions. For this reason, no details regarding the formulation for direct hydro-mechanical coupling in porous media have been provided. The latter, together with the weak form of balance equations and their discretization, are given in ref. [37]. While the preliminary results of simulations are promising, further research is needed for verification of the quantitative performance of the proposed approach. This will require the identification of the law of kinetics for a specific physicochemical process associated with fracture healing/sealing and the implementation of the framework in a boundary value problem that could serve as a benchmark.

References

1. Aliko-Benitez A, Doblare M, Sanz-Herrera J.A. Chemical-diffusive modeling of the self-healing behaviour in concrete. *Intern. Journ. Solids & Struct.* **2015**, *69-70*, 392-402.
2. Van Tittelboom K, De Belie N. Self-healing in cementitious materials – a review. *Materials*. **2013**, *6*, 2182-2217.
3. Neville A. Autogenous healing – a concrete miracle? *Concr. Intern.* **2002**, *24*, 76-82.
4. Granger S, Loukili A, Pijaudier-Cabot G, Chanvillard G. Experimental characterization of the self-healing cracks in an utra high performance cementitious material: mechanical tests and acoustic emission analysis. *Cem. Concr. Res.* **2007**, 37, 519-527.
5. Qureshi T.S, Kanellopoulos A, Al-Tabbaa A. Encapsulation of expansive powder minerals within a concentric glass capsule system for self-healing concrete. *Constr. & Build. Materials*. **2016**, *121*, 629-643.
6. Joseph C, Jefferson A.D, Isaacs B, Lark R.J, Gardner D.R. Experimental investigation of adhesive-based self-healing of cementitious materials. *Mag. Concr. Res.* **2010**, *62*, 831–843.
7. Chen J, Ren S, Yang C, Jiang D, Li L. Self-healing characteristics of damaged rock salt under different healing conditions. *Materials*. **2013**, *6*, 3438-3450.
8. Costin L.S, Wawersik W.R. Creep healing of fractures in rock salt. *Sandia National Lab. Rep. SAND80-1375.* Albuquerque. **1981**.
9. Bastiaens W, Bernier F, Xiang L.L. SELFRAC: Experiments and conclusions on fracturing, self-healing, and self-sealing processes in clays. *Phys. Chem. Earth*. **2007**, *32*, 600–615.
10. Tsang C, Bernier F, Davies C. Geohydromechanical processes in the Excavation Damaged Zone in crystalline rock, rock salt, and indurated and plastic clays—in the context of radioactive waste disposal. *Intern. Journ. Rock Mech. Min. Sci.* **2005**, *42*, 109-125.
11. Elkhoury J.E, Detwile, R.L, Ameli P. Can a fracture caprock self-heal? *Earth Plant. Sci. Lett.* **2015**, *417*, 99-106.
12. Renard F, Gratier J.P, Jamtveit B. Kinetics of crack-sealing, intergranular pressure solution, and compaction around active faults. *Journ. Struct. Geol.* **2000**, *22*, 1395–1407.
13. Zhang S.Q, Paterson M.S, Cox S.F. Microcrack growth and healing in deformed calcite aggregates. *Tectonophysics* **2001**, *335*, 7–36.

14. Zhang C.L. Experimental evidence of self-sealing of fractures in claystone. *Phys. Chem. Earth*. **2011**, *36*, 1972-1980.

15. Auvray C, Moriot C, Fourreau E, Talandier C. X-ray tomography applied to self-healing experiments on argillites. Proceedings of ISRM 13, International Congress of Rock Mechanics. Montreal, Canada. **2015**.

16. Arson C. Micro-macro mechanics of damage and healing in rocks. *Open Geomech.* **2020**, *2*, 1-41.

17. Mauludin L.M, Oucif C. Modeling of self healing concrete: a review. *Journ. Appl. Comput. Mech.* **2019**, *5*, 526-539.

18. Kachanov M. Continuum model of medium with cracks. *Journ. Eng. Mech. Div.* **1980**, *106*, 1039-1051.

19. Lemaitre, J, Chaboche J.L. *Mechanics of solid materials*; Cambridge University Press: Cambridge, U.K. **1990**.

20. Jacobsen S, Marchand J, Boisvert L. Effect of cracking and healing on chloride transport in OPC concrete. *Cem. Concr. Res*. **1996**, *26*, 869-881.

21. Ramm W, Biscoping M. Autogenous healing and reinforcement corrosion of water-penetrated separation cracks in reinforced concrete. *Nucl. Eng. Des*. **1998**, *179*, 191-200.

22. Adam J.A. A simplified model of wound healing (with particular reference to the critical size defect). *Math. Comput. Model*. **1999**, *30*, 23-32.

23. Ando K, Chu M.C, Tsuji K, Hirasawa T, Kobayashi Y, Sato S. Crack healing behaviour and high-temperature strength of mullite/sic composite ceramics. *Journ. Eur. Ceram. Soc*. **2002**, *22*, 1313-1319.

24. Little D.N, Bhasin A. Exploring mechanisms of healing in asphalt mixtures and quantifying its impact. In: van der Zwaag. S. (Ed.), Self- Healing Materials. Springer. **2007**, 205-218.

25. Barbero E.J, Greco F, Lonetti. P. Continuum damage-healing mechanics with application to self-healing composites. *Int. Journ. Damage Mech*. **2005**, *14*, 51-81.

26. Miao S, Wang M.L, Schreyer H.L. Constitutive models for healing of materials with application to compaction of crushed rock-salt. *J. Eng. Mech*. **1995**, *121*, 1122-1129.

27. Zhu C, Arson C. (2015). A model of damage and healing coupling halite thermo-mechanical behavior to microstructure evolution. *Geotech. Geolog. Eng.* **2015**, *33*, 389–410.

28. Pietruszczak S, Ushaksaraei R, Gocevski V. Modeling of the effects of alkali-aggregate reaction in reinforced concrete structures. *Comp. Concr.* **2013**, *12,* 627-650.

29. Belytschko T, Black T. Elastic crack growth in finite elements with minimal remeshing. Int. Journ. Numer. Meth. Engng. 1999, 45, 601–20.

30. Moës N, Dolbow J, Belytschko T. A finite element method for crack growth without remeshing. Int. Journ. Numer. Meth. Engng. 1999, 46,131–50.

31. Sukumar N, Moës N, Moran B, Belytschko T. Extended finite element method for three-dimensional crack modelling. Int. Journ. Numer. Meth. Engng. 2000, 48, 1549–70.

32. Haghighat E, Pietruszczak S. On modeling of discrete propagation of localized damage in cohesive-frictional materials. *Int. Journ. Num. Anal. Meth. Geomech.* **2015,** *39,* 1774-1790.

33. Pietruszczak S, Lydzba D., Shao J.F. Modeling of deformation response and chemo-mechanical coupling in chalk. Int. Journ. Numer. Meth. Engng. 2006, 10, 997-1018.

34. Lydzba D., Pietruszczak S, Shao J.F. Intergranular pressure solution in chalk; a multiscale approach. Comp. & Geotech. 2007, 34, 291-305.

35. Wang G, Lu D, Du X, Zhou X, Cao S. A true 3D frictional hardening elastoplastic constitutive model of concrete based on a unified hardening/softening function. *Journ. Mech. Phys. Solids* **2018**, *119*, 250-273.

36. Pietruszczak S. On homogeneous and localized deformation in water-infiltrated soils. *Int. Journ. Damage Mech.* **1999**, *8,* 233-253.

37. Jameei A.A, Pietruszczak S. Embedded discontinuity approach for coupled hydro-mechanical analysis of fractured porous media. *Int. Journ. Num. Anal. Meth. Geomech.* **2020**, DOI: 10.1002/nag.3112.

38. Coussy O. *Poromechanics*; John Wiley & Sons: Chichester, England. **2004**.

39. Labiouse V, Escoffie S, Gastaldo L, Mathier J.F. Self-sealing od localised craks in Boom and Opalinus Clay hollow cylinders. Proceedings of European Commission TIMODAZ-THERESA Intern. Conference, Luxemburg. **2009**.

40. Martin C.D, Lanyon G.W. EDZ in clay shale. *Mont Terri Tech. Report. TR-2001-01.* **2002**.

41. Liu J, Sun S, Sun S, Yue L, Wei J, Wu J. Mechanical and failure charactreristics of rock-like material with multiple crossed joint sets under uniaxial compression. *Adv. Mech. Eng.* **2017**, *9*, 1-18.

Chapter 4

Impact of salt crystallization on the mechanical properties of structural masonry: an experimental and numerical study

Pietruszczak S, Przecherski P, Stryszewska T (2022). Impact of salt crystallization on the mechanical properties of structural masonry: An experimental and numerical study. Construction and Building Materials. 344: 128062.

https://doi.org/10.1016/j.conbuildmat.2022.128062

Impact of salt crystallization on the mechanical properties of structural masonry: an experimental and numerical study

S. Pietruszczak (1), P. Przecherski (2) and T. Stryszewska(2)

(1) Department of Civil Engineering, McMaster University, Hamilton, Ontario, Canada

(2) Department of Civil Engineering, Cracow University of Technology, Cracow, Poland

Abstract: This paper provides the results of an experimental study examining the evolution of mechanical properties of primary constituents of structural masonry (i.e., brick units, mortar and brick-mortar interfaces) during the process of salt crystallization. The precipitated salt changes the pore structure. At the early stages, the porosity decreases which enhances the mechanical performance. However, as the concentration of precipitated salt increases further, the internal damage within the porous matrix leads to a progressive degradation of mechanical properties. The aim of this research is to assesses the impact of salt crystallization on the conditions at failure and the stiffness characteristics of the constituent materials. The evolution laws are expressed in terms of a parameter which represents the degree of accumulation of salt precipitated in pore space. The general form of an elastoplastic constitutive relation, employing this parameter, is briefly discussed and the results of some preliminary numerical simulations are given.

Keywords: masonry, salt crystallization, mechanical degradation, microstructure

1. Introduction and motivation

Salt crystallization has long been recognized as a major source of damage in masonry structures (cf. ref. [1]). Salts and salt-forming elements can be naturally present within masonry construction materials or may come from external sources. For example, Portland cement may contain sodium and potassium hydroxides and sulfates, while bricks may also contain sodium sulfate [2], all of which are water soluble. External sources include capillary absorption of groundwater containing salts, salts carried by the wind from the sea or salts from air polluted rain [1, 3, 4]. In addition, the road salt and other de-icing activities are also a contributing factor.

Salt crystallization may occur at different sites depending on the rate of saturation and rate of drying. In the conditions of high humidity, when the evaporation rate is low, salt crystal growth occurs primarily near the surface, which is referred to as efflorescence. This process is relatively harmless to the material itself. However, when the evaporation rate is high, salt crystallizes in the pores of the material. Such phenomenon is referred to as sub-florescence. In this case, the growth of crystals can lead to a significant degradation of hydro-mechanical properties at the macroscale [5-8].

Over the last few decades, a substantial amount of research has been devoted to investigation of the damage attributed to sub-florescence, not only in masonry but in other commonly used construction materials such as concrete and natural stone [4, 9-12]. The crystallization process itself is affected by several factors including the salt type, the solution properties and the characteristics of the porous network, viz. the pore size distribution and pore shape [13-14]. The nucleation of salt crystals occurs when the solution becomes supersaturated. The crystal growth generates internal forces within the matrix leading to stress concentrations which trigger formation of tensile microcracks that propagate and coalescence. The effect can be very pronounced as porous materials have, in general, a low tensile strength. The value of crystallization pressure depends primarily on the degree of supersaturation of the solution and the geometry of pore microstructure [6, 15-16]. In recent years several authors have attempted to evaluate the build up of stress generated by salt crystallization [7,15]. The results of these studies provide a valuable insight into the physics of the problem, in particular the influence of thermodynamic and kinetic factors. At the same time however, a precise quantification is difficult in view of numerous simplifications that need to be employed in relation to microstructural arrangement and the assessment of mechanical properties at microscale. In addition, the kinetics of sub-florescence crystallization is still not completely understood [17]. There are several open issues concerning the description of the nucleation process, its location within the pore network, and the rate of crystals growth. Furthermore, the prediction of mechanical effects induced by crystallization still poses significant difficulties due to complex couplings between different physical phenomena.

The *experimental* work dealing with damage mechanism associated with salt precipitation involves either the cycles of immersion in salt solution and drying or a permanent contact with a solution to allow for a continuous capillary rise. The literature on this topic is quite extensive and comprehensive reviews are provided, for example, in refs. [18-19]. The primary focus in that research has been on the aspects dealing with salt transport and crystallization in various construction materials [12, 20-23]. This also included investigations into the effect of salt on the degradation of physico-mechanical properties [24- 26]. For structural masonry, the experimental research on coupling the effects crystallization with mechanical response has been rather limited and concentrated primarily on the shear behaviour of masonry walls/triplets [27-29]. In addition to the above-mentioned work, there has also been a significant number of experimental studies on mitigation of damage resulting from salt crystallization. Examples include research on alleviation of salt damage in cement-based materials [30], in lime mortar [31] as well as in porous limestones widely used in historic architecture [32].

The assessment of long-term damage scenarios in large scale structures requires the use of *numerical* analysis of the coupled effects of kinetics of sub-florescence. However, as mentioned earlier, the description of hygro-thermal-chemical-mechanical (HTCM) coupling is very challenging. In fact, the hygro-thermal behaviour alone is quite complex as the diffusion and crystallization of salt depends not only on the transport of water and salt in the form of gas, solid and liquid, but also on the phase transition between them. The macroscopic formulation is typically an extension of the heat and moisture transport models (e.g., [33-36]) to account for the presence of salts, viz. diffusion and crystallization [37-40]. Coupled modeling of salt transport and damage due to crystallization has been addressed within a rather limited scope, mainly in the context of poroelasticity [5, 39].

The present study provides the results of an experimental investigation that examines the evolution of strength and deformation characteristics of primary constituents of masonry (i.e., bricks, mortar joints, and brick-mortar interfaces) during the process of salt crystallization. It needs to be pointed out that the salt transport process, and thus the kinetics of evolution of properties, is time dependent implying that the classical approaches, such as elasticity or plasticity, need to be enhanced to incorporate this effect. The latter has not, to the authors' knowledge, been accounted for in the existing formulations. The motivation of this work is to phrase the evolution laws in terms of the degree of pore saturation with precipitated salt (i.e. volume of crystallized salt per volume of voids). Such a parameter may then be conveniently employed in the development of the governing constitutive equations that couple the mechanical response with the salt transport and precipitation phenomena. In this work an elastoplastic approach is briefly discussed, and the results of some preliminary numerical simulations are given. The details on a general formulation of the governing constitutive relations, which includes the notion of localized deformation, will be presented separately.

2. Materials and methods

The experimental tests were conducted on samples of ceramic bricks, cement mortar and samples containing the brick-mortar interface, all contaminated with magnesium sulfate. The main focus was on investigation of the evolution of mechanical properties, although the primary physical properties were also examined. The tests were designed so that to provide information on the specification of failure criteria and their evolution with the degree of saturation of pores with precipitated salt. The obtained experimental evidence was also used in an attempt to formulate the inelastic constitutive relations governing the deformation process in constituent materials in the course of accumulation of crystallized salt.

The masonry units used for testing were solid clay bricks burnt at temperature of 870^0C. The X-ray diffraction studies indicate that the brick material contains quartz, sanidine, hematite and the amorphous phase that was also visible in scanning electron microscope images. It is noted that the same bricks were used in a previous study of one of the co-authors and the detailed characteristics are provided in ref. [25]. The mortar comprised Portland cement and quartz fillers, with the ratio of binder to fillers of 1:3. The material complied with BS EN 998-2:2016 standards.

For the experimental work, 30 bricks with uniform texture and no noticeable defects were selected from a stack by a visual examination. Out of these, a number of units were randomly chosen from which samples were extracted. The *mechanical* tests on brick material were carried out on cylindrical specimens with diameter of 50mm and the height of 100mm. The specimens of cement mortar had the same dimensions and were prepared in casting molds. The total of 45 brick samples and 45 mortar samples were tested. In addition, 45 specimens containing the brick-mortar bond were prepared. The samples had the dimensions of 210x60x60 mm and comprised three brick cubes (60x60x60 mm) interspersed with mortar joints of thickness 15 mm. For *physical* testing, viz. evaluation of density of solids and pore size distribution, small cylindrical samples of brick and mortar (diameter 25 mm and height of 50 mm) were used. The assessment of volume change due to crystallization involved additional cubic samples 60x60x60 mm. Overall, over 150 samples were prepared and tested.

The specimens were saturated for 2 days in $MgSO_4$ solution with sulphate ion concentration of $100g/dm^3$, and subsequently dried for 5 days at the room temperature of 22±1°C and the relative humidity of 35±5%. Note that the conditions of exposure to salinity employed here were analogous to those adopted in previous research [25]. The selection of salt, i.e. magnesium sulfate, was based on the fact that it forms hydrates, has a high ability to fill pores during exposure and is quite aggressive, thereby triggering a significant degradation of mechanical properties. The experimental program included a total of 20 cycles of saturation and drying. The mass of each sample was measured every 24hrs. while the mechanical as well as the physical tests were carried out at an interval of 5 cycles.

2.1. The scope of experimental investigation

A schematic diagram, which outlines the scope of the testing program, is provided in Fig. 1 below.

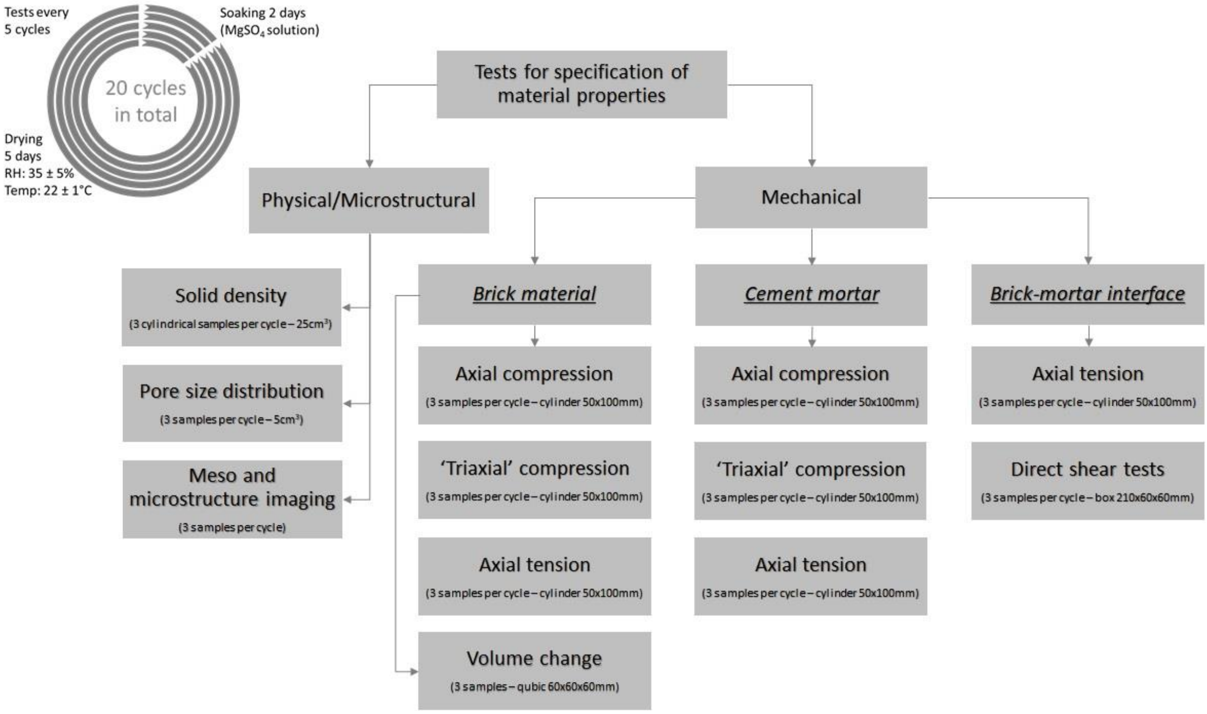

Fig. 1. Schematic diagram of the testing program.

The physical tests, which were complementary to the mechanical component, included measurements of bulk density as well as density of solid particles for both constituent materials, i.e. bricks and cement mortar. The measurements of density of solids were obtained using the gas pycnometer Ultrapyc 1200e. In this case, the volume of solids was assessed after every 5 cycles of saturation and drying. In addition, the evolution of porosity and pore size distribution was examined. The latter was investigated by mercury intrusion porosimetry using Nova 1000e porosimeter (Quantachrome Corp.).

The density and porosity measurements were supplemented by the examination of the structure of the material at both the meso and microlevel. The *mesoscale* investigations utilized the optical microscope Zeiss Discovery v20. The *microstructure* investigations were conducted using a scanning electron microscope (Zeiss EVO MA10). The imaging employed detection of backscattered as well as secondary electrons, the latter providing a more detailed surface information. In addition, the element mapping was conducted using the energy dispersive x-ray spectroscopy with the XFlash 6-30 detector. The content of selected elements, in particular magnesium and sulphur, after 15 cycles of exposure was determined. The latter is indicative of the presence of magnesium sulphate crystals.

The mechanical tests performed on brick and cement mortar samples included axial compression, axial tension and triaxial compression. All tests complied with EN standards. The tests under uniaxial conditions were carried out using Zwick/Roell Z100 testing machine. The applied loading rate was 0.1 MPa/s and a minimum of 3 samples were tested after every 5 cycles of saturation and drying. The specimens for tensile tests had an initial imperfection, i.e. a very shallow notch in the mid-height circumference. This ensured that the fracture took place in the central part of the specimen, away from the grips.

The triaxial tests were carried out using MTS 815 Rock Mechanics Triaxial Testing System. The samples were tested at the confining pressure corresponding to approx. 50% of compressive strength. Thus, the range of confinement was 7.5-12 MPa for the brick samples and 8.5-20 MPa for cement mortar samples. All tests were load-controlled and were carried out at room temperature.

The mechanical tests on brick samples were supplemented by examining the evolution of free (unconstrained) expansion due to crystallization. This information is, in general, required in formulating the constitutive relations. The volume change was assessed by measuring the linear deformation in three orthogonal directions along the specimens' axes. These measurements were carried out using demountable strain gauges manufactured by Mayes Instruments Ltd.

The experiments on brick-mortar bond included direct shear tests at normal stress of zero (no confinement) and 0.55 MPa. A schematic diagram of the test setup is shown in Fig. 2. The tests were conducted using the same equipment as for axial compression/tension, i.e. the Zwick/Roell Z100 testing machine. Here, the vertical load was applied to the middle brick unit at the rate of 0.1 MPa/s. For tests with confining stress, the lateral load of 2 kN was applied to outer brick cubes through rigid steel plates. Again, a minimum of 3 samples were tested after every 5 saturation/drying cycles.

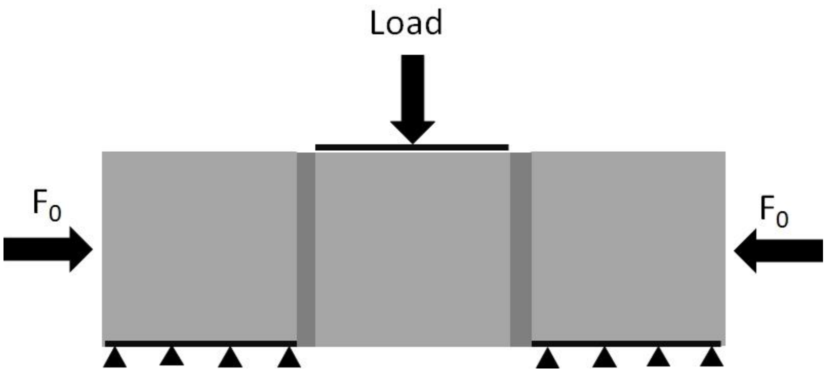

Fig. 2. Schematic diagram of the shear test setup (dark gray denotes the mortar joint).

2.2. *Methodology for interpretation of mechanical tests: formulation of a general form of failure criterion*

The mechanical tests were focused on the assessment of strength and deformation properties in constituent materials (i.e. bricks, mortar and the brick-mortar interface) at different stages of exposure to magnesium sulphate contamination. The objective of this testing program was to identify the evolution of strength parameters that govern the conditions at failure.

For brick material and mortar, the simplest form of the failure criterion is the Mohr-Coulomb representation with Rankine's cut-off in the tensile regime. Such a criterion can be expressed in terms of stress invariants as (cf. ref. [41])

$$F = \max(F_1, F_2) = 0; \quad F_1 = q - \eta_f g(\theta)(p + C); \quad F_2 = g_1(\theta)q - (p + \sigma_t) \tag{1}$$

where $q = \sqrt{3}\,(J_2)^{\frac{1}{2}}$, $p = -I_1/3$, $\theta = \frac{1}{3} sin^{-1}[-J_3/(2q^3)]$ and

$$g(\theta) = \frac{3 - sin\phi}{2\sqrt{3}cos\theta - 2sin\theta\, sin\phi}; \; \eta_f = \frac{6sin\phi}{3 - sin\phi}; \; C = c\, cot\phi\,; \qquad g_1(\theta) = \frac{2}{3}\sin\left(\theta + \frac{2\pi}{3}\right) \tag{2}$$

Here, I_1, J_2, J_3, are the basic invariants of stress tensor/deviator, θ is the Lode's angle, while ϕ, c and σ_t represent the angle of friction, cohesion and the tensile strength, respectively. In case when the pore water contains dissolved salts, the strength parameters will undergo a progressive evolution that can be related to the degree of pore filling with crystallized salt $S_{\boldsymbol{c}}$. Thus, $\phi = \phi(S_{\boldsymbol{c}}),\ c = c(S_{\boldsymbol{c}})$ and $\sigma_t = \sigma_t(S_{\boldsymbol{c}})$. The evolution laws for these parameters may be assumed in a polynomial form

$$\sigma_t = \sigma_{t0}\,(1 + a_1 S_{\boldsymbol{c}} + a_2 S_{\boldsymbol{c}}^2 + a_3 S_{\boldsymbol{c}}^3 + \ldots) = \sigma_{t0}\big(1 + \textstyle\sum_{n=1}^{m} a_n S_{\boldsymbol{c}}^n\,\big)\,;$$

$$\phi = \phi_0\big(1 + \textstyle\sum_{n=1}^{m} b_n S_{\boldsymbol{c}}^n\big)\,;\quad c = c_0\big(1 + \textstyle\sum_{n=1}^{m} c_n S_{\boldsymbol{c}}^n\big) \tag{3}$$

where the subscript 0 refers to the referential state and a_n, b_n, c_n are the coefficients of approximation. The specification of material parameters that are embedded in the general form of the evolution laws (3) requires a specific methodology that is described in Section 3.2.

For the brick-mortar bond, the functional form similar to that of eq.(1) may be employed for the description of conditions at failure. In this case, however, the failure criterion needs to be phrased in terms of components of traction vector, rather than the stress invariants. The details of this representation are discussed later in Section 3.2(iii).

3. Experimental results

This section presents the results of experimental study. First, the evolution of basic physical properties of brick material and mortar, at different stages of exposure to magnesium sulphate contamination, are reviewed. This includes the measurements of density of solid particles, bulk density and the pore size distribution. Also, the evolution of microstructure, which was recorded at selected intervals, is discussed. The main results of the current study, which deal with the assessment of mechanical properties and quantification of the degradation laws, viz. eqs. (3), are presented in Section 3.2.

3.1. Physical and microstructural properties of materials

Table 1 gives the information on the density of solids as well as the bulk density for both constituent materials, i.e. bricks and cement mortar. It is evident that the particle density gradually decreases, while the bulk density marginally increases within the considered number of cycles. This might be attributed to the fact that the crystallization in pore space increases the mass of dry sample while, at these relatively early stages of degradation, the volume change due to formation of microcracks is still not very pronounced.

Table 1. Evolution of density of constituents during exposure to contamination.

	Brick		**Mortar**	
Cycle #	Density of soilds [g/cm^3]	Bulk density [g/cm^3]	Density of soilds [g/cm^3]	Bulk density [g/cm^3]
0	2.61	1.82	2.72	2.09
5	2.50	2.00	2.64	2.19
10	2.44	2.10	2.60	2.26
15	2.41	2.16	2.58	2.28
20	2.40	2.18	2.58	2.29

The quantitative measurements of pore size distribution in brick and mortar samples are provided in Figs. 3-4 and Tables 2-3. The results indicate that, prior to exposure to contamination, the dominant pore size in bricks (for over 80% of population) was in the range 100-10,000 nm. The second largest population (over 10%), were pores with a diameter of 10,000-20,000 nm. In case of mortar, the prevailing pore size was in the range of 50-2,500 nm for approx. 75% of population. Saturation with magnesium sulphate caused a change in porosity structure towards smaller pores. After 20 cycles of exposure, the dominant pore size in bricks was less than 5,000 nm (for over 90% of population) while for mortar, over 70% of pores were in the range of 50 nm 2500 nm.

As pointed out in ref. [42], micropores with size ranging from 100 to 10000 nm represent the population that has a dominant influence on shaping and facilitating the transport and crystallization process. This was the case in the present study as well. As a result, the salt precipitation significantly reduced the population of larger pores in favor of smaller ones. In fact, in case of brick material, the largest pores nearly disappeared after 20 cycles of exposure. In mortar, the dominant pore size shifted towards smaller pores with a diameter in the range of 100 nm. In general, a pore size below 100 nm is associated with the presence of gel pores characteristic of cement binders (C-S-H). These pores fill very slowly and the crystallization process begins there only after reaching a critical supersaturation of the salt solution in larger pores [43].

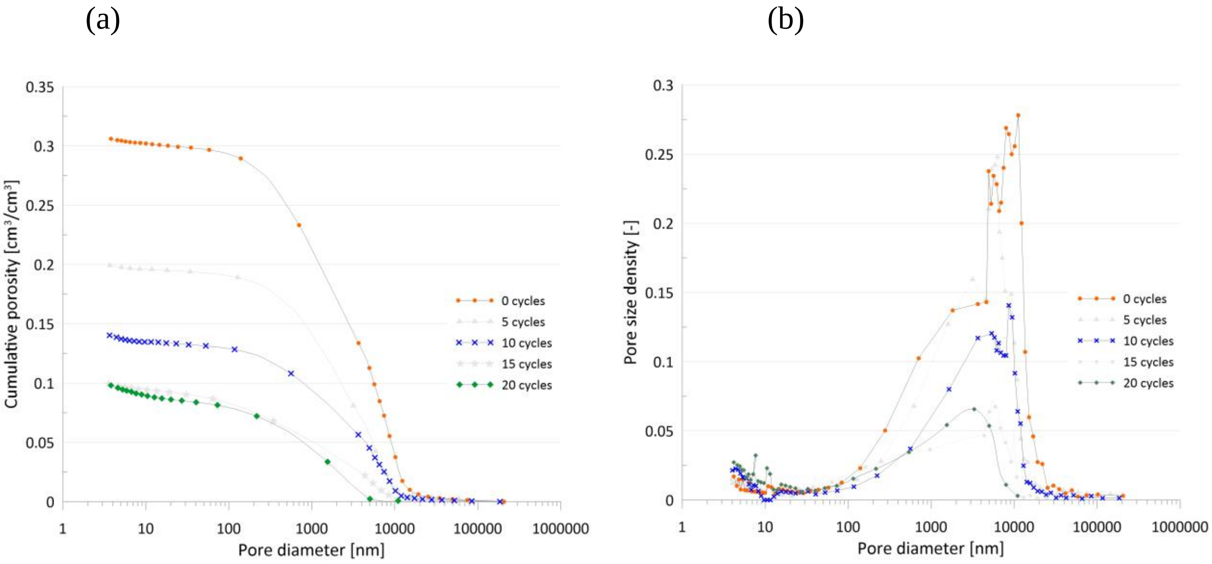

Fig. 3. (a) Cumulative and (b) population curves of pore volume in brick samples at different stages of exposure to contamination.

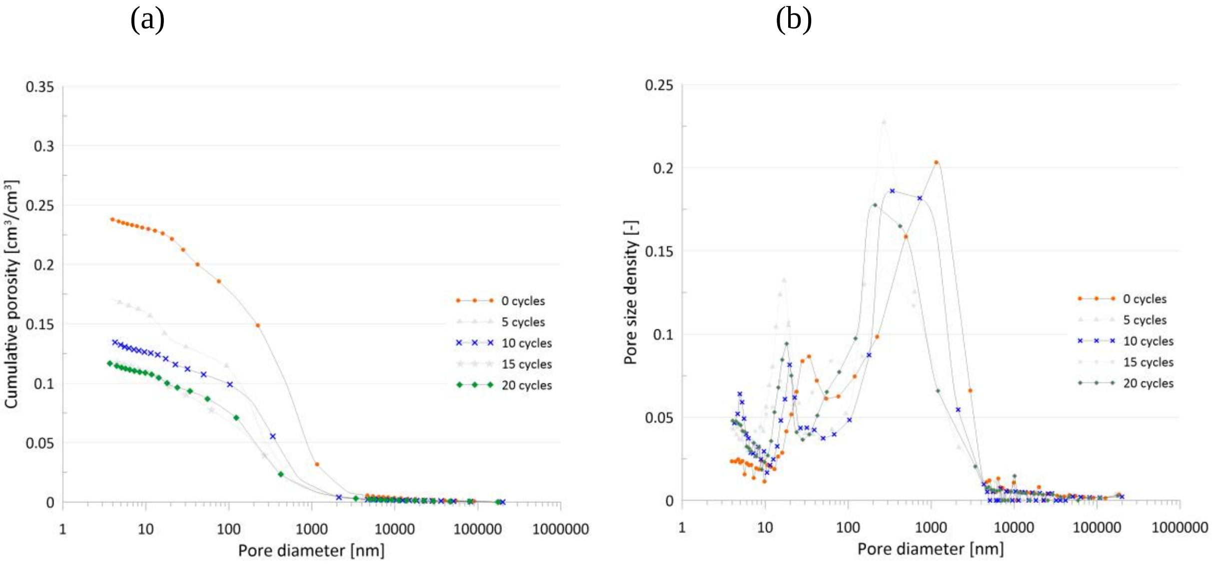

Fig. 4. (a) Cumulative and (b) population curves of pore volume in mortar samples at different stages of exposure to contamination.

Table 2. Pore size distribution in brick samples.

Pore diameter [nm]	0 cycles	5 cycles	10 cycles	15 cycles	20 cycles
<100	4.5 %	6.4 %	7.9 %	18.8 %	18.6 %
100-5000	59.7 %	60.8 %	61.4 %	62.6 %	79.0 %
5000-10000	22.0 %	21.0 %	23.2 %	15.9 %	2.0 %
10000-20000	12.0 %	9.3 %	5.9 %	1.2 %	0.4 %
>20000	1.8 %	2.5 %	1.6 %	1.5 %	0.0 %
Open porosity	30.6 %	19.9 %	14.0 %	10.2 %	9.7 %

Table 3. Pore size distribution in mortar samples.

Pore diameter [nm]	0 cycles	5 cycles	10 cycles	15 cycles	20 cycles
<50	17.5 %	20.2 %	22.1 %	22.9 %	23.8 %
50-500	55.1 %	55.4 %	53.4 %	54.3 %	62.9 %
500-2500	19.2 %	18.1 %	20.1 %	19.9 %	10.7 %
2500-10000	6.8 %	5.1 %	3.2 %	1.5 %	1.2 %
>10000	1.4 %	1.2 %	1.2 %	1.4 %	1.4 %
Open porosity	23.9 %	17.2 %	13.6 %	12.0 %	11.7 %

Apparently, the degree of material degradation is largely affected by the number of exposure cycles. The crystallization induced damage was observed on the surfaces of the samples as well as in the pore space. Fig.5 shows the images of the interior of brick samples at the magnification of 50x and 150x. The images were taken before and after a long-term exposure to contamination. In this case, the crystals of magnesium sulfate are clearly visible along the crack as well as inside the pores.

Some representative images of microstructure of brick and mortar samples at the magnification ranging from 100x to 1500x are provided in Figs. 6-7. Note that SEM images in Fig.6 show the presence of microcracks as well as the salt crystals inside the pores. At the same time, SEM images in Fig 7 show the presence of both elements, viz. S and Mg, that indicates the location of magnesium sulphate crystals. Clearly, the onset and propagation of microcracks has an impact not only on mechanical, but also physical and petrographic properties [44], including intra-granular microtexture [45].

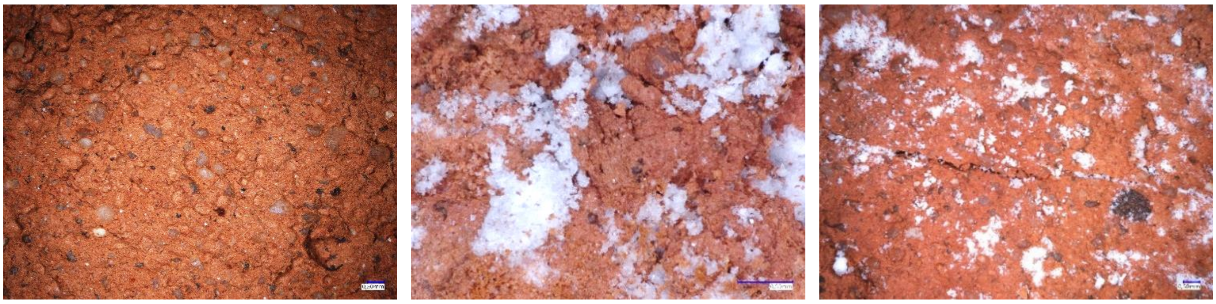

Fig. 5. The images of brick sample obtained from an optical microscope at the magnification of 50x, 150x and 50x. The images taken after 0, 15 and 20 cycles of exposure; larger cracks and salt crystals are visible.

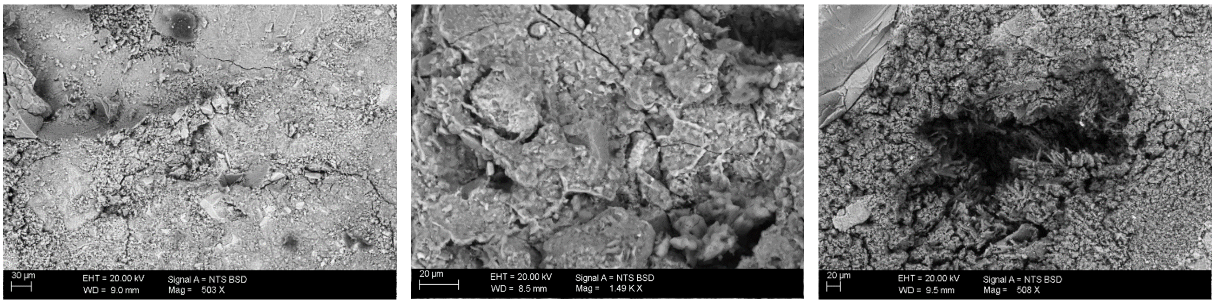

Fig.6. SEM images of microstructure taken after 15 cycles of exposure. Left: mortar sample at magnification of 500x; middle and right: brick samples at magnification of 1500x and 500x, respectively. Note: microcracks are visible in both materials; in the last figure - salt crystals are visible.

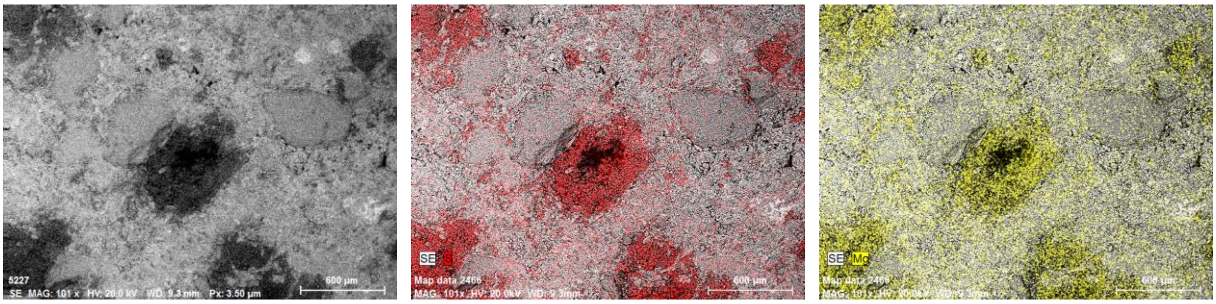

Fig.7. SEM images of microstructure of a brick sample at the magnification of 100x. The two figures on the right show mapping of selected elements; the presence of S and Mg indicates the location of magnesium sulphate crystals. Images taken after 15 cycles.

3.2. *Results and interpretation of mechanical tests*

(i) Impact of salt crystallization on the mechanical properties of bricks

As mentioned earlier, the brick samples were subjected to a total of 20 cycles of saturation with $MgSO_4$ solution and drying. During this process the mass changes were recorded every 24 hrs. Fig. 8a shows the evolution of mass during the first two cycles. It is seen that stationary conditions were reached after approx. 48 hrs of saturation and 120 hrs of drying. In subsequent cycles (Fig. 8b), the rate of mass accumulation, which was associated with precipitation of salt crystals in the pore space, progressively decreased. After approx. 10 cycles, crystalline deposits of salt were visible on the surface of the specimen (efflorescence). At the same time, the material underwent internal damage as a result of crystal growth in the pore space (sub-florescence). The latter is evidenced through the meso/microstructural imaging as discussed in the previous section (cf. Figs. 5-7).

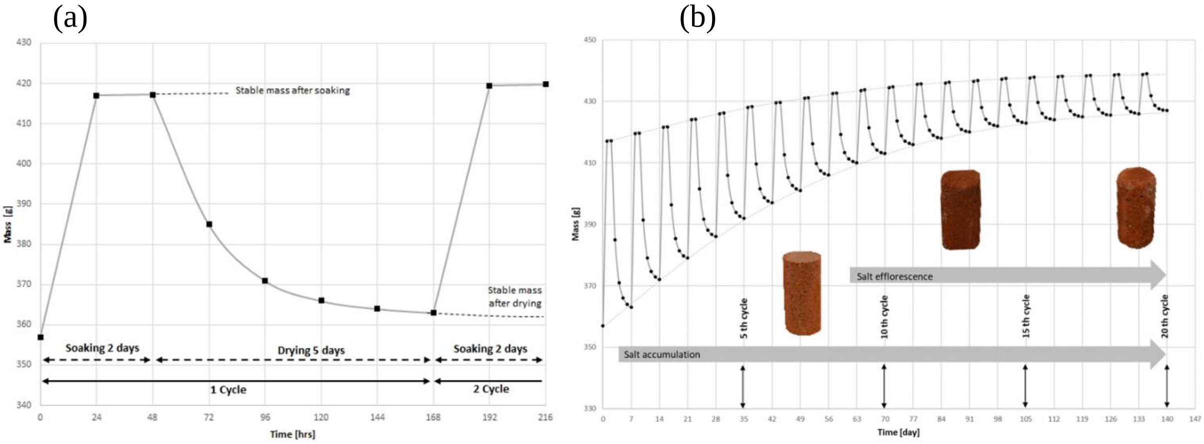

Fig. 8. (a) Time history of sample saturation and drying; (b) evolution of mass.

The results of unconfined compression tests, at different stages of salt crystals accumulation, are presented in Fig. 9a. As mentioned earlier, a minimum of 3 samples were tested after every 5 cycles and the grey area shown in this figure gives the range of experimental scatter. It is evident that the strength of the material, as well as its initial stiffness, significantly increase during the first 10 cycles. Subsequently, a progressive degradation of mechanical properties takes place and after 20 cycles both the strength and the tangential stiffness are markedly reduced compared to the referential state.

The supplementary figure, i.e. Fig. 9b, shows the variation of ultimate strength with the number of cycles. The strength varies within the range of approx. 12-26 MPa. Here, the dataset is approximated using a third-degree polynomial; however, higher-order polynomial functions may also be employed, if required. It should be noted that the distribution of strength is presented here using a dual horizontal scale that correlates the cycle numbers with the corresponding values of the *volume fraction of salt crystallized within the pore space* (S_c). The latter was estimated from the measurements of the volume of solids V_s , obtained from the gas pycnometer readings (cf. Section 3.1), using the relation

$$S_{\boldsymbol{c}} = \frac{(M - M_0)/\rho_s}{n\,V} \quad ; \qquad n = \frac{V - V_s}{V} \tag{4}$$

Here, n is the porosity, M_0 is the referential mass of the dry sample, M is the mass after each drying cycle, ρ_s is the density of salt and V is the sample volume. Apparently, other more elaborate techniques are available for the assessment of the value of $S_{\boldsymbol{c}}$**.** Those include tests for the content of salts that are soluble in water as well as tests for quantitative evaluation of elemental composition expressed as percentage by weight (e.g., X-ray fluorescence analysis).

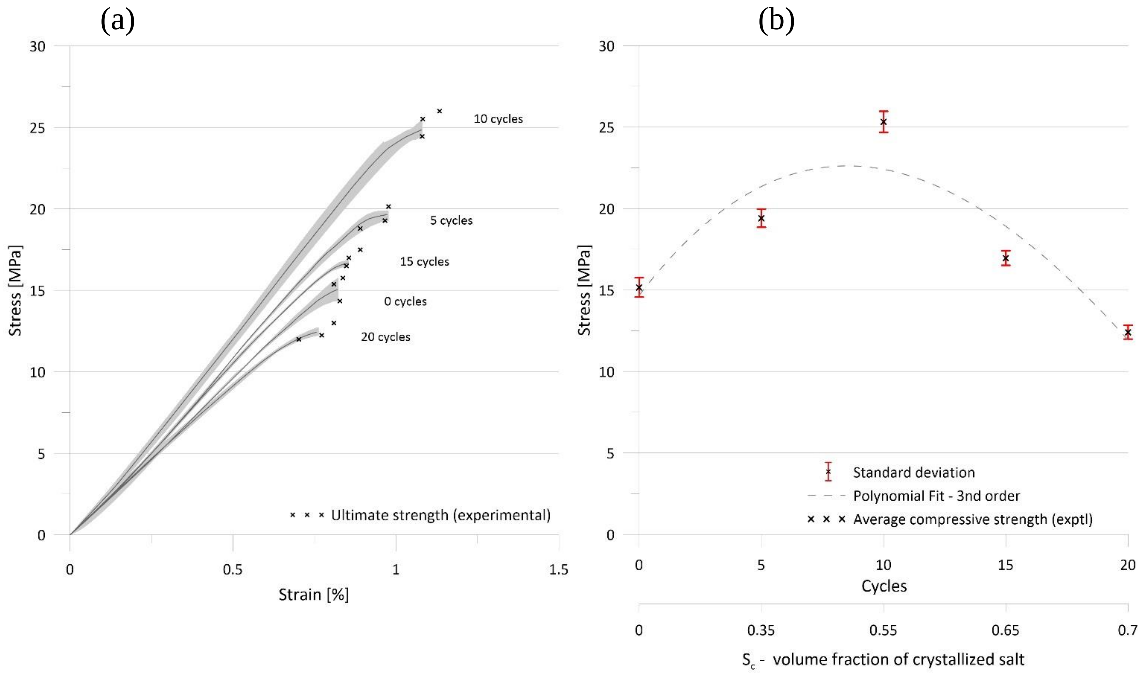

Fig. 9. (a) Average stress-strain characteristics for bricks subjected to uniaxial compression; (b) evolution of strength during the exposure to contamination.

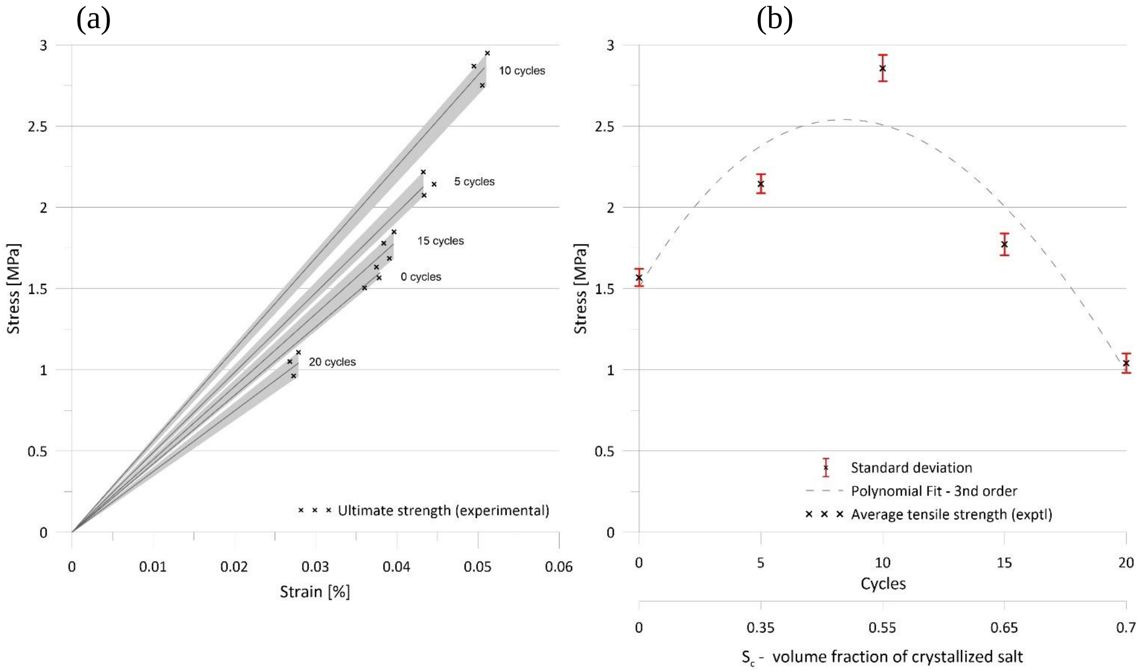

Fig. 10. (a) Average stress-strain characteristics for bricks under uniaxial tension; (b) evolution of tensile strength during the exposure to contamination.

The average stress-strain characteristics in axial tension are shown in Fig. 10. The behaviour was predominantly elastic-brittle, and all samples failed by developing a macrocrack perpendicular to the loading direction. As the tests were load-controlled no unstable strain-softening response was recorder. The qualitative trends are similar to those observed in axial compression. In particular, both the strength and stiffness increase during the first 10 cycles followed by a progressive degradation in subsequent cycles. Fig. 10b depicts the evolution of tensile strength, which is within the range of 1-3 MPa, against the number of cycles and the estimated volume fraction of crystallized salt. Once again, the dataset is approximated using a second-degree polynomial relating the strength to the number of cycles.

The specification of conditions at failure, as defined by eqs.(1)-(2), requires additional ‘triaxial’ tests performed under a prescribed confinement. Note that in ‘triaxial’ configuration the stress state is axisymmetric, i.e. $\sigma_2 = \sigma_3$, so that the stress invariants in representation (1) become

$$q = \sigma_3 - \sigma_1 \; ; \quad p = -(\sigma_1 + 2\sigma_3)/3 \; ; \quad \theta = \pm\pi/6 \tag{5}$$

As mentioned earlier, the samples were tested at the confining pressure p corresponding to approx. 50% of compressive strength and the corresponding deviatoric stress (q) vs. axial strain characteristics are provided in Fig. 11. It is evident that, the qualitative trends are similar to those depicted earlier. In the presence of confinement, the strength is higher, and it progressively degrades after 10 cycles of exposure to salt contamination. A detailed information on the value of confining pressure and the deviatoric stress intensity at failure q_f is provided in the adjacent legend.

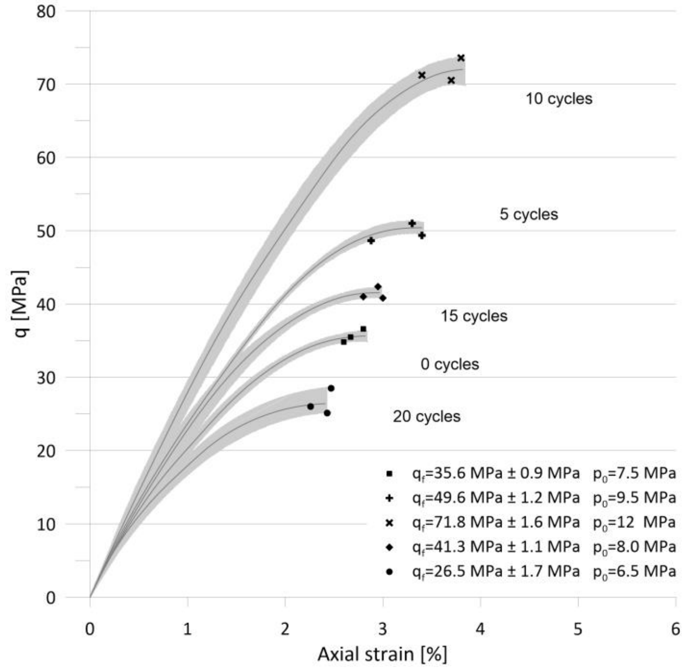

Fig. 11 . Average stress-strain characteristics for bricks in 'triaxial' tests.

In order to specify the evolution laws (3) for the basic material parameters (viz. the angle of friction ϕ and cohesion c) it is convenient to interpret the results of all tests, including uniaxial compression and tension, in the 'triaxial' (p, q) space. In this case, the functional form (1) reduces to

$$\begin{aligned} &q > 0: \quad F_1 = q - \eta_f(p + C);\; F_2 = q - 3(p + \sigma_t) \\ &q < 0: \quad F_1 = q + \tilde{\eta}_f(p + C);\; F_2 = q + 3(p + \sigma_t)/2 \end{aligned} \tag{6}$$

where $\tilde{\eta}_f = 6sin\phi/(3 + sin\phi)$. Note that in all tests conducted here, the samples were brought to failure by increasing (or decreasing in case of axial tension) the vertical stress under $\Delta\sigma_2 = \Delta\sigma_3 = 0$, so that the stress trajectory is a line with the slope of $\Delta q/\Delta p$=3.

Fig. 12a shows the 'triaxial' stress paths, together with the best-fit approximations to failure envelopes, eq.(6), for samples tested in the referential state, i.e. prior to exposure to magnesium sulphate contamination. At the same time, Fig. 12b shows the evolution of failure criterion with the number of cycles. It is noted that the Mohr-Coulomb criterion overestimates the strength under hydrostatic tension C, which is typically in the same range as σ_t, so that the approximation involving Rankine cut-off is justified here. Alternatively, the conditions at failure may be described by a quadratic approximation in the meridional (p, q) space. The details on defining such a representation are provided in ref. [41].

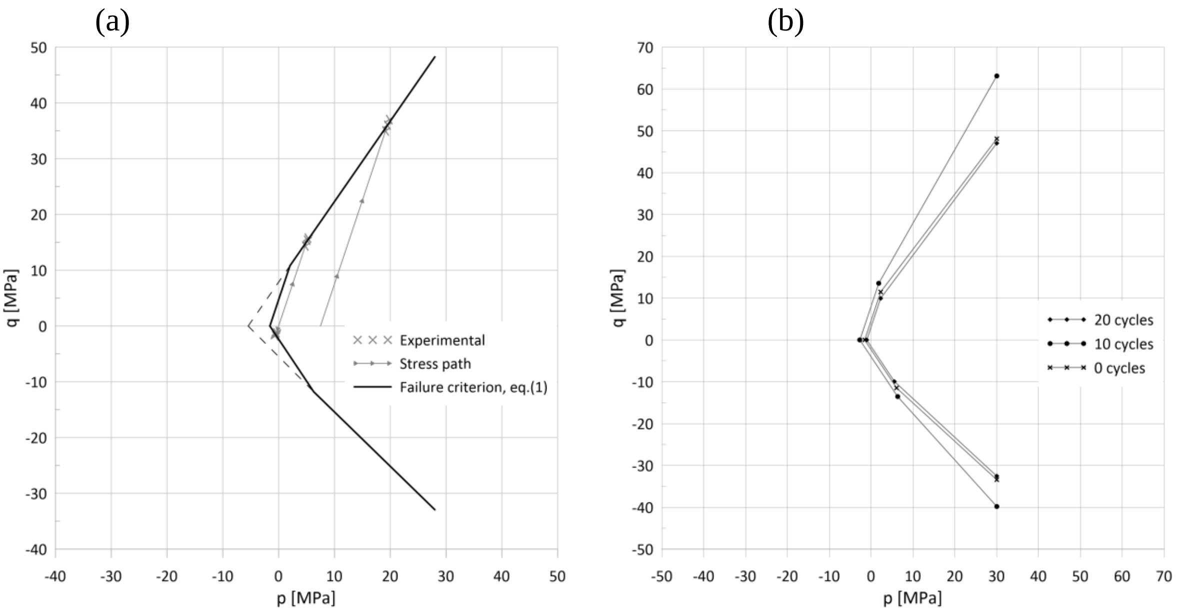

Fig. 12 . Linear best fit approximations to failure envelopes (a) in the referential state and (b) after exposure to magnesium sulphate contamination.

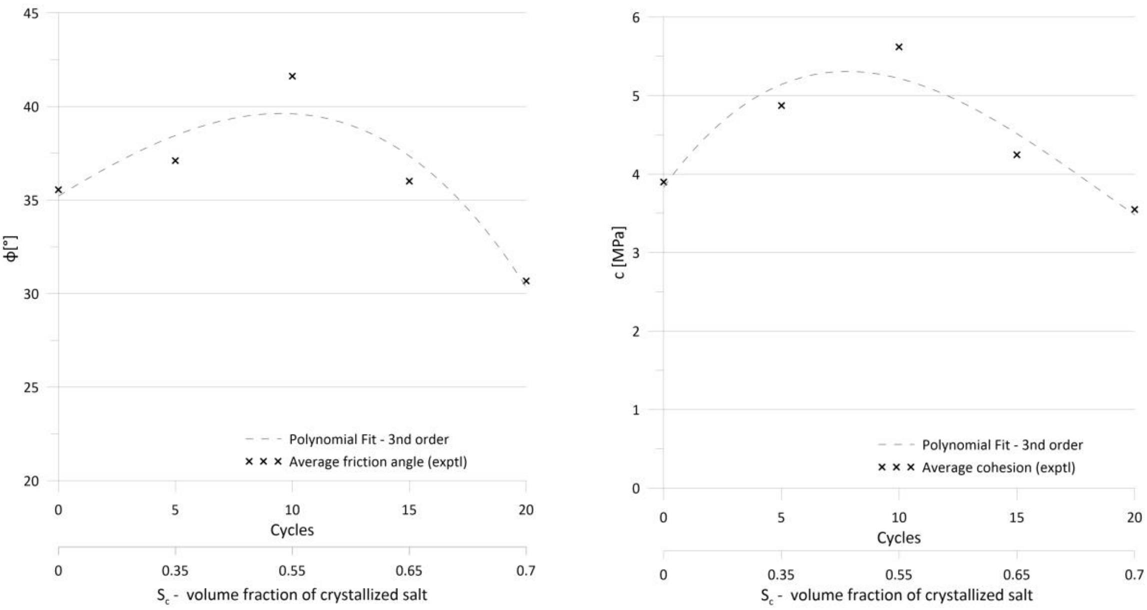

Fig. 13 . Evolution of friction angle and cohesion with the number of contamination cycles.

Given the results in Fig.12, the evolution laws for the basic strength parameters, i.e. ϕ and c, can be established. Fig. 13 shows the variation of both these parameters with the number of cycles as well as with the estimates of volume fraction of salt crystallized in pores. The friction angle varies within the range of 31^0-42^0, while the cohesion remains within the interval of 3.5-5.5 MPa. The trends in the evolution of both these parameters are similar to those in Figs. 9b and 10b. The initial increase can likely be attributed to the reduction in porosity, while the degradation is due to damage associated with crystallization pressures. Here, the best-fit approximations incorporating third degree polynomials are also provided.

The impact of salt crystallization on the elastic stiffness has been assessed by conducting a series of unloading tests at different stages of uniaxial compression. The key results are presented in Fig.14. It is noted that the linear part of average stress-strain characteristics corresponding to increasing load is not, in general, indicative of the elastic response. The unloading process results here in permanent deformations (Fig. 14a), so that the Young's moduli should be identified with the initial slope of the unloading branch. The results based on this assessment are shown in Fig. 14b, which presents the variation of the Young's modulus with the number of cycles. It is apparent that the increase in stiffness is confined to a relatively narrow range of 2300-3300 MPa, which indicates that the salt contamination process has more significant impact on the strength characteristics than on the elastic stiffness properties.

Finally, the other manifestation of damage associated with the accumulation of salt crystals in the pore space (i.e. sub-florescence) is the dilatancy of the material at the macroscale. This is addressed in Fig.15 which shows the evolution of volume change during the consecutive saturation/drying cycles. It is seen that beyond 10 cycles the samples undergo expansion with a progressively increasing rate. The expansion is nearly hydrostatic, which is evident from Fig. 15a.

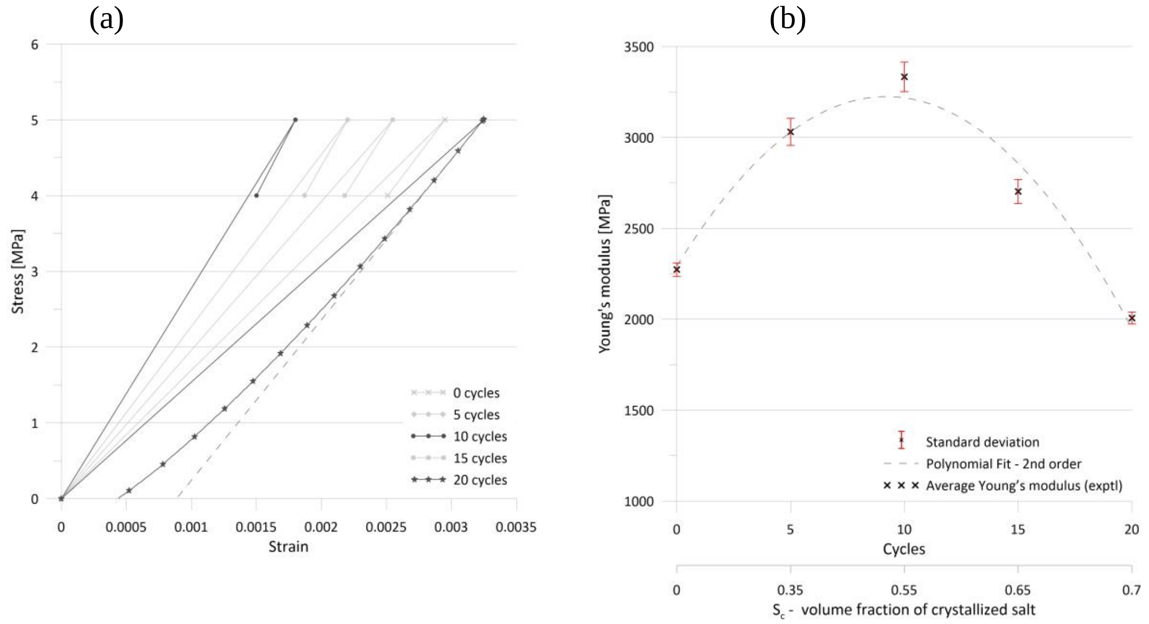

Fig. 14. (a) Unloading cycles in uniaxial compression and (b) evolution of Young's modulus during the exposure to magnesium sulphate contamination.

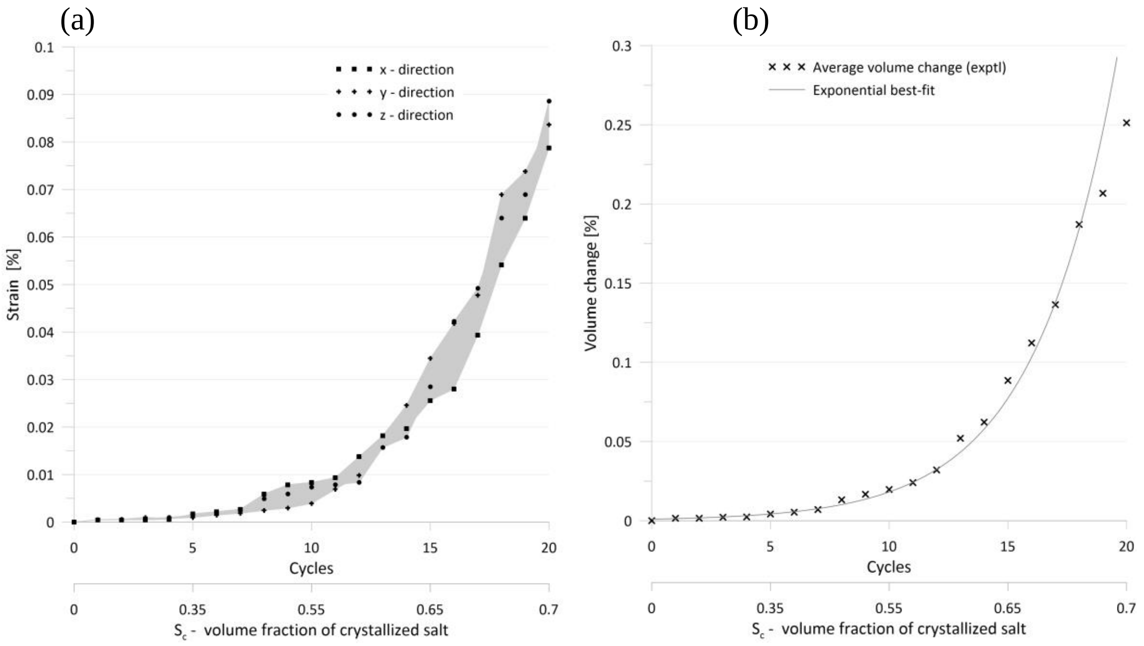

Fig. 15. Evolution of free expansion with the number of contamination cycles; (a) individual components, (b) the volume change.

(ii) *Impact of salt crystallization on the mechanical properties of mortar*

The mortar samples were subjected to the same procedure of immersion in $MgSO_4$ solution and drying as the brick specimens. The scope of mechanical tests was also similar, i.e. it included axial compression, axial tension and triaxial compression. The volume fraction of salt crystallized within the pore space was again estimated using eq.(4). The results of axial compression tests, at different stages of salt contamination, are presented in Fig. 16. Fig. 16a shows the average stress-strain characteristics, while Fig. 16b gives the corresponding evolution of compressive strength. The latter is approximated here using a third-degree polynomial. The strength varies within the range of approx. 17-41 MPa, which is higher than that for the brick material; however, the trends in its evolution are very similar. Again, after approx. 10 cycles, a progressive degradation of properties takes place, and the strength falls below that of the referential material.

The results of tests involving axial tension are presented in Fig. 17. The stress-strain characteristics (Fig. 17a) are again supplemented by variation of strength with the number of cycles and the corresponding volume fraction of crystallized salt (Fig. 17b). The failure mode was identical to that observed in bricks, i.e. the samples failed in a brittle manner by developing a tensile crack perpendicular to the direction of loading. The tensile strength is now within a range of 1.2-3.7 MPa, which is close to that for the brick material, and its evolution indicates that the onset of degradation of properties commences again after approx. 10 cycles.

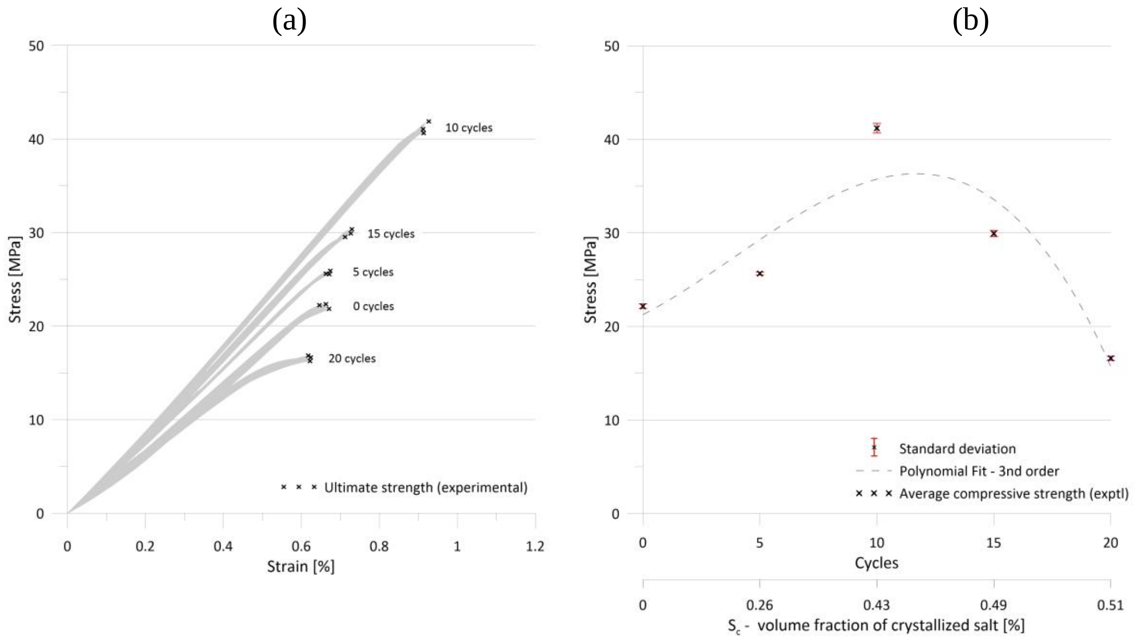

Fig. 16. (a) Average stress-strain characteristics for mortar subjected to uniaxial compression; (b) evolution of strength during the exposure to contamination.

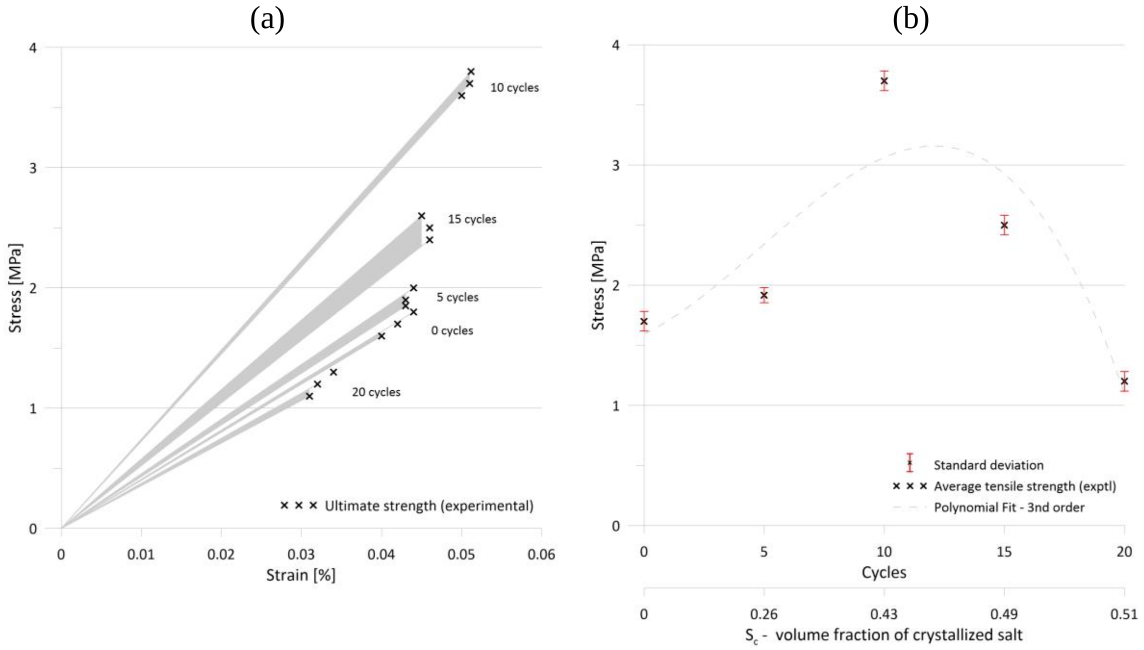

Fig. 17. (a) Average stress-strain characteristics for mortar under axial tension; (b) evolution of tensile strength during the exposure to contamination.

Given the fact that the qualitative trends in mechanical response of mortar are similar to those of the brick material, it is reasonable to assume that the failure criterion has the functional form analogous to eq. (1). In this case, the specification of material parameters entails, once again, the tests in ‘triaxial’ (*p*, *q*) configuration. Fig. 18 shows the deviatoric stress–axial strain characteristics obtained in these tests. A detailed information on the applied confining pressures and the corresponding stress intensities at failure q_f is provided in the adjacent legend.

Fig. 19 shows the best-fit approximations to failure envelopes, eq.(6), for mortar samples tested before and after the exposure to magnesium sulphate contamination (Figs. 19a and 19b, respectively). At the same time, Fig. 20 shows the variation of Mohr-Coulomb strength parameters, i.e. ϕ and *c*, with the number of cycles and the estimates of volume fraction of salt crystallized in pores. It is seen that ϕ varies within the range of 30-39^{0}, while the value of *c* remains within the interval of 5-10 MPa. Thus, compared to the brick material, mortar has a slightly lower friction angle and a higher cohesion. In spite of quantitative differences, the general trends in the evolution of both these parameters are similar to those in Figs. 13a and 13b. The initial increase in strength stems from the reduction in pore space, while the degradation is associated with damage due to crystallization pressures. Once more, a third-degree polynomial approximations relating the values of strength parameters to the number of cycles are provided.

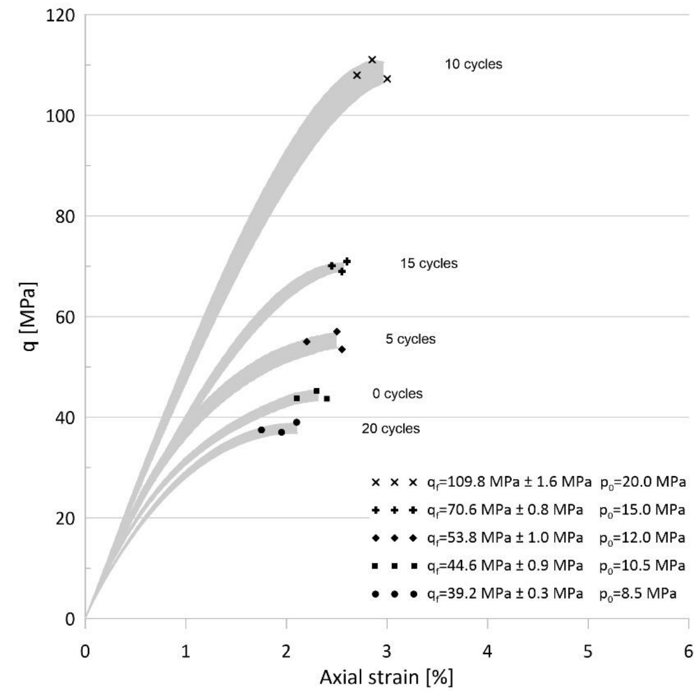

Fig. 18. Average stress-strain characteristics for mortar in ‘triaxial’ tests.

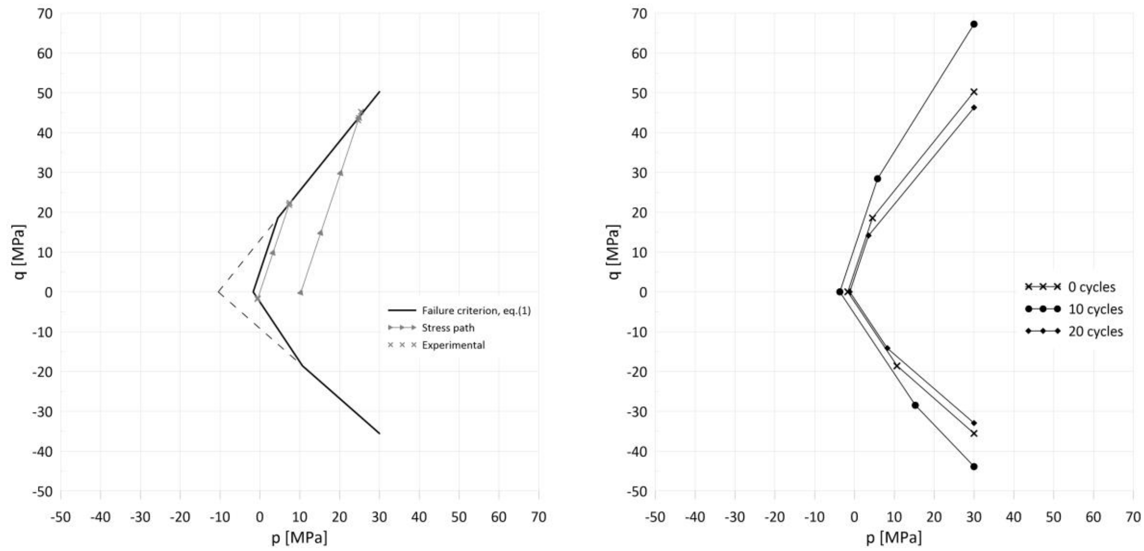
(a) (b)

Fig. 19. Failure envelopes for mortar (a) in the referential state and (b) after exposure to magnesium sulphate contamination.

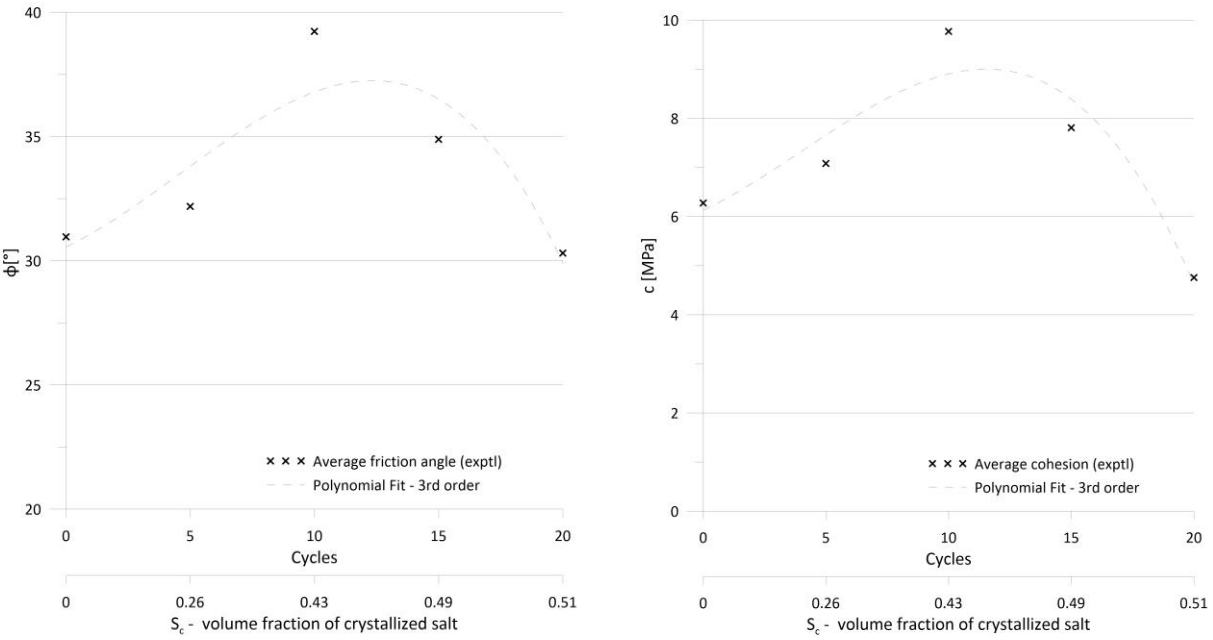

Fig. 20. Variation of friction angle and cohesion with the number of contamination cycles.

(iii) Impact of salt crystallization on the mechanical properties of brick-mortar bond

The tests on brick-mortar bond, which is the weakest link in structural masonry, involved axial tension as well as a direct shear; the latter with no confinement and with the presence of lateral load providing a prescribed normal stress, cf. Fig. 2. The primary objective was, once again, to identify the conditions and failure and the evolution of strength parameters. The failure criterion for the interface can be defined in terms of shear (τ) and the normal (σ) components of the traction vector acting on it. In this case, the functional form similar to eq.(1), which incorporates the Coulomb representation with Rankine's cut-off in the tensile regime, may be employed. Thus,

$$F = \max(F_1, F_2) = 0; \quad F_1 = |\tau| + \eta\,\sigma - c; \quad F_2 = \sigma - \sigma_t \qquad (7)$$

where $\eta = tan\phi$ and $\phi = \phi(S_c)$, $c = c(S_c)$, $\sigma_t = \sigma_t(S_c)$, i.e. the strength parameters depend on the volume fraction of salt crystallized in the pores within the region adjacent to the interface. Apparently, some non-linear approximations, e.g. a quadratic form, may be used instead of eq. (7).

The friction angle and cohesion can be identified from the results of direct shear tests. Fig.21 shows the shear 'stress-displacement' characteristics at $\sigma = 0$ and $\sigma = -0.55$ MPa (lateral load of 2 kN, Fig.2). The former results (Fig. 21a) explicitly define the evolution of cohesion, while the latter supplementary set of data (Fig. 21b) allows specification of the friction angle. The variation of both strength parameters with the number of contamination cycles is shown in Fig. 22. Again, the number of cycles can be corelated with the volume fraction of crystallized salt. It is recognized, however, that tracing the crystallization within the interface itself is somewhat ambiguous given its infinitesimal thickness. Therefore, the evolution of strength parameters is presented here in terms of volume fraction of salt precipitated in the constituents (in this case, in brick material). It is seen that cohesion c varies within the range of 0.8-1.7 MPa, while $\phi \in (27-35^0)$. Thus, compared to both the bricks and mortar, the strength is significantly lower. The same conclusion is evident from the results of axial tension, which are presented in Fig. 23. The failure has again a brittle nature and the tensile strength is now reduced to the range 0.6-1.1 MPa, which clearly indicates that the interface is the weakest constituent in the masonry system.

Given the results of the experimental tests, the failure envelopes (7), and their variation in the course of salt contamination, can be identified as shown in Fig. 24. The general trends are consistent with the earlier findings. At initial stages of the sub-florescence process, the brick-mortar bond gains strength, while the subsequent damage induced by development of crystallization pressures leads to degradation of strength properties, and thus a contraction of the failure surface.

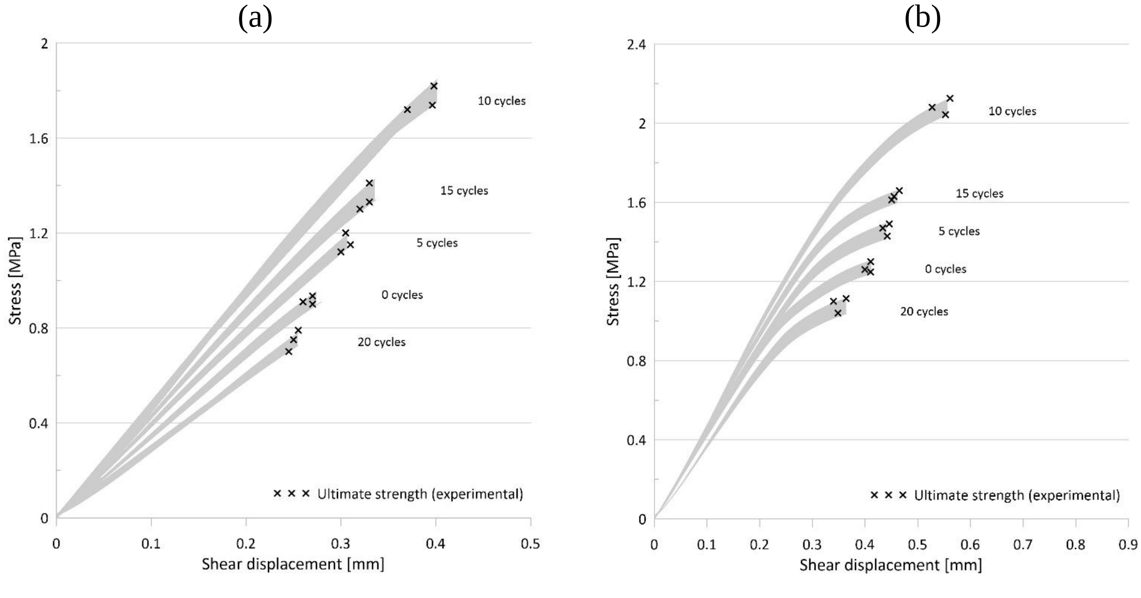

Fig. 21. Results of direct shear tests on brick-mortar bond; shear stress – displacement characteristics; (a) at no confinement, (b) at σ=-0.55 MPa.

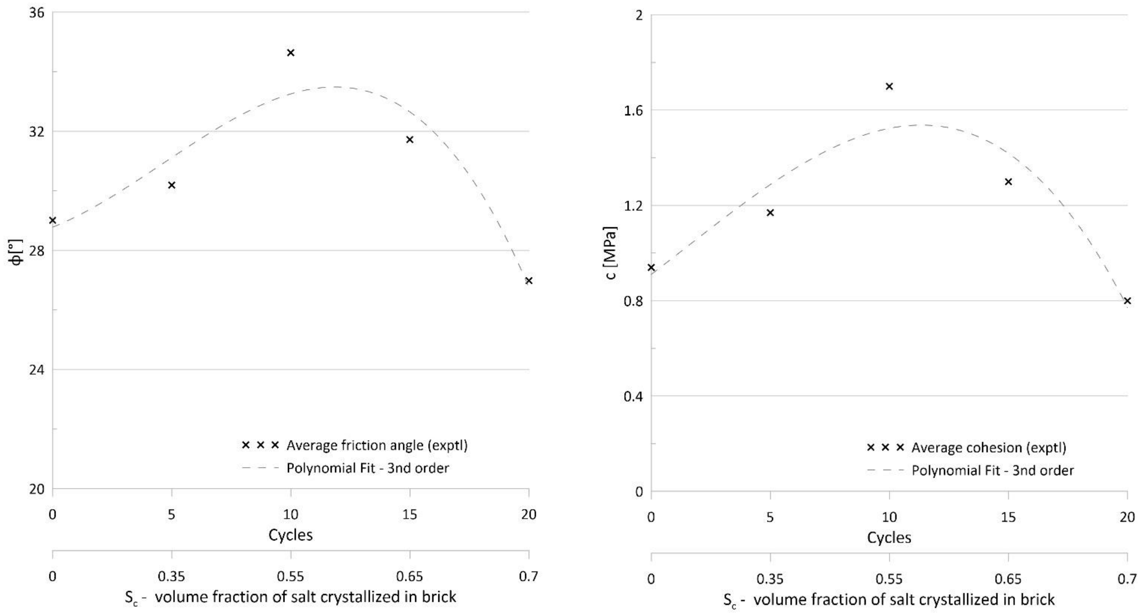

Fig. 22. Variation of friction angle and cohesion for brick-mortar bond with the number of contamination cycles.

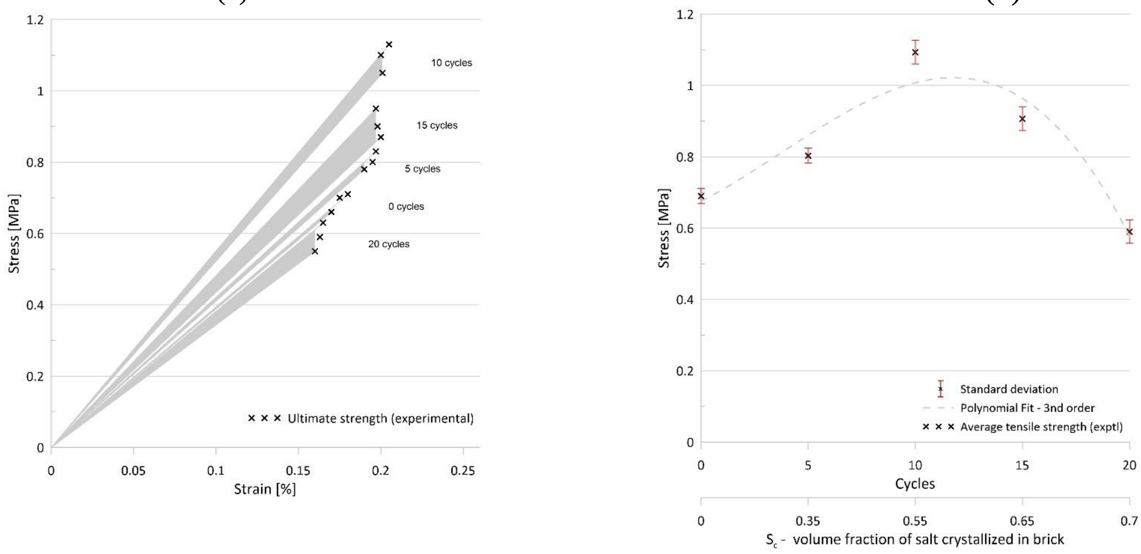
(a)

(b)

Fig. 23. (a) Average tensile stress-strain characteristics for brick-mortar bond; (b) variation of tensile strength with the number of contamination cycles.

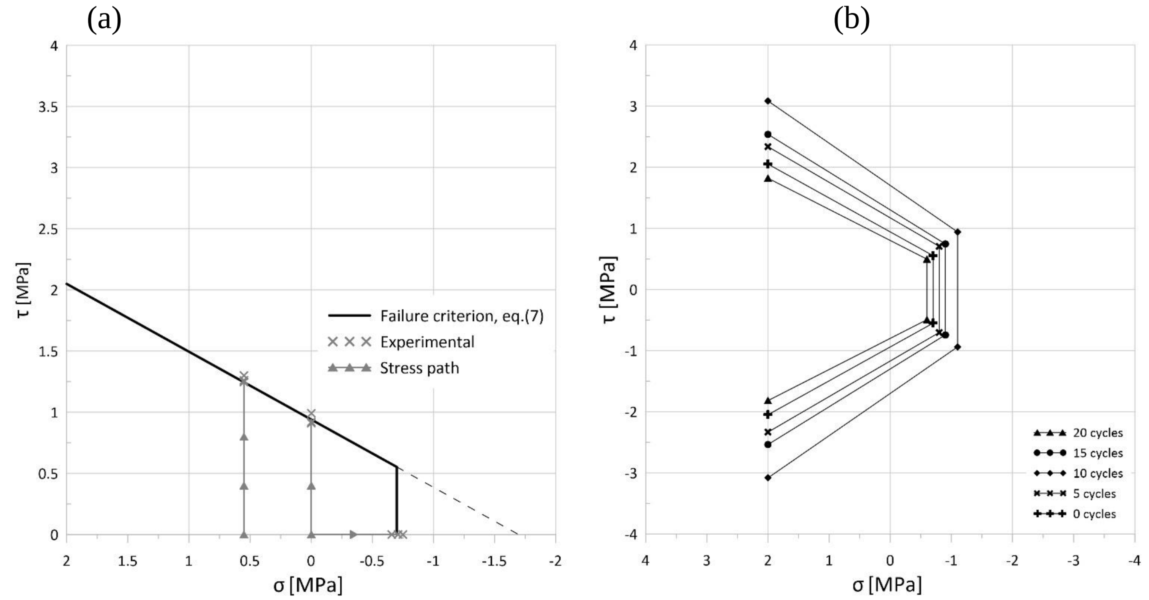

Fig. 24. Failure envelopes for brick-mortar bond (a) in the referential state and (b) after exposure to magnesium sulphate contamination.

4. Numerical analysis

Let us examine now the implications of incorporating the evolution laws (3) in the formulation of constitutive relations. Consider the constituent materials to be elastoplastic and focus on the effect of variation of *strength* (rather than deformation) parameters, which seems to be dominant in the course of crystallization process (cf. Fig. 14). In this case, the additivity of elastic and plastic strain rates can be expressed as

$$\dot{\varepsilon}_{ij} = \dot{\varepsilon}_{ij}^{e} + \dot{\varepsilon}_{ij}^{p} = C_{ijkl}^{e}\,\dot{\sigma}_{kl} + \dot{\varepsilon}_{ij}^{p}\,; \qquad \dot{\varepsilon}_{ij}^{p} = \dot{\lambda}\,\frac{\partial G}{\partial \sigma_{ij}} \tag{8}$$

Here, C_{ijkl}^{e} is the elastic compliance operator, $\dot{\lambda}$ is the plastic multiplier and G is the plastic potential function. In the presence of salt precipitation, the yield function f depends explicitly on the volume fraction of crystallized salt (S_c**).** Thus, for an active loading process there is $f(\sigma_{ij}\,, \dot{\varepsilon}_{ij}^{p},\ S_c) = 0$, so that the consistency condition becomes

$$\dot{f} = \frac{\partial f}{\partial \sigma_{ij}}\,\dot{\sigma}_{ij} + \frac{\partial f}{\partial \varepsilon_{ij}^{p}}\,\dot{\varepsilon}_{ij}^{p} + \frac{\partial f}{\partial S_{\boldsymbol{c}}}\,\dot{S}_{\boldsymbol{c}} = 0 \tag{9}$$

Substituting the flow rule, eq.(8), into eq. (9) and solving for the plastic multiplier, one obtains

$$\dot{\lambda} = \frac{1}{h}\left(\frac{\partial f}{\partial \sigma_{ij}}\,\dot{\sigma}_{ij} + \frac{\partial f}{\partial S_{\boldsymbol{c}}}\,\dot{S}_{\boldsymbol{c}}\right)\; ; \quad h = -\frac{\partial f}{\partial \varepsilon_{ij}^{p}}\,\frac{\partial G}{\partial \sigma_{ij}} \tag{10}$$

Thus, the constitutive relation can be expressed in a general form

$$\dot{\varepsilon}_{ij} = \left(C_{ijkl}^{e} + \frac{1}{h}\frac{\partial f}{\partial \sigma_{ij}}\,\frac{\partial G}{\partial \sigma_{ij}}\right)\dot{\sigma}_{kl} + \frac{1}{h}\frac{\partial f}{\partial S_{\boldsymbol{c}}}\,\frac{\partial G}{\partial \sigma_{ij}}\;\dot{S}_{c} \tag{11}$$

Note that the second term in the expression above represents the contribution from evolution of material properties triggered by the crystallization process.

In order to illustrate the performance of the above formulation, let us employ the framework of deviatoric hardening [41]. In this case, the yield surface may be assumed in the form consistent with representation (1), i.e.

$$f = q - \eta g(\theta)(p + C); \quad \eta = \eta_f\,\frac{\zeta\,\kappa}{A + \kappa}\; ; \quad d\kappa = \left(\frac{2}{3}\; de_{ij}^{p}\, de_{ij}^{p}\right)^{1/2} \tag{12}$$

where e_{ij}^{p} is the plastic strain deviator, $\eta_f = \eta_f(S_c)$, and A, ζ are the material parameters. Note that, according to the hardening rule in eq.(12), $\kappa \to \infty$ results in $\eta \to \zeta\eta_f$, where $\zeta > 1$. The constant ζ is employed here to define the transition to strain localization, which is assumed to occur at $\eta = \eta_f$. The latter equality is satisfied for $f = F_1$, so that the conditions at failure are consistent with Mohr-Coulomb criterion (1). In general, however, the inception of localization may be considered as a bifurcation problem [46].

Finally, the plastic potential function may be defined as

$$G = q + \eta_c g(\theta)(p + C)\; ln\;\frac{(p + C)}{p_0} \tag{13}$$

where η_c is the dilatancy coefficient defined as $\eta_c = \alpha\eta_f$ and α is a material constant. The rationale for choosing this particular form stems from the fact that it accounts for a smooth transition from compaction to dilatancy prior to failure (cf. ref. [47]), which is typical for both brick material and mortar.

The deviatoric hardening framework, as defined above, is illustrated here by simulating the mechanical response of brick samples in axial compression, followed by a creep resulting from the evolution of volume fraction of crystallized salt. For the uniaxial compression, the basic strength parameters, i.e. ϕ and c, were identified from the experimental data reported in Fig. 13. The elastic properties were assumed as constant; the Young's was assigned a value of 2500

MPa (cf. Fig. 14), while the Poisson's ratio was taken as 0.25. In the elastoplastic range, the parameter ζ was assigned the value of 1.2 and the corresponding value of A=0.002 was then estimated by a trial-and-error to best-fit the stress-strain characteristic in the referential state (i.e. prior to salt contamination). Again, given the focus of this study, it was assumed that A is a constant, i.e. is not significantly affected by the volume fraction of crystallized salt.

The results of numerical simulations are presented in Figs. 25-27. Fig. 25 shows the simulations of uniaxial compression tests after 0, 10 and 20 cycles of saturation/drying, which corresponds to S_c= 0, 0.55 and 0.7, respectively. The transition to strain localization, which is set to occur at $\eta = \eta_f$, is indicated schematically by a broken line. Note that no volume change characteristics are provided here, as these were not recorded in the experiments. The numerical results are, in general, consistent with the tests data (Fig. 9).

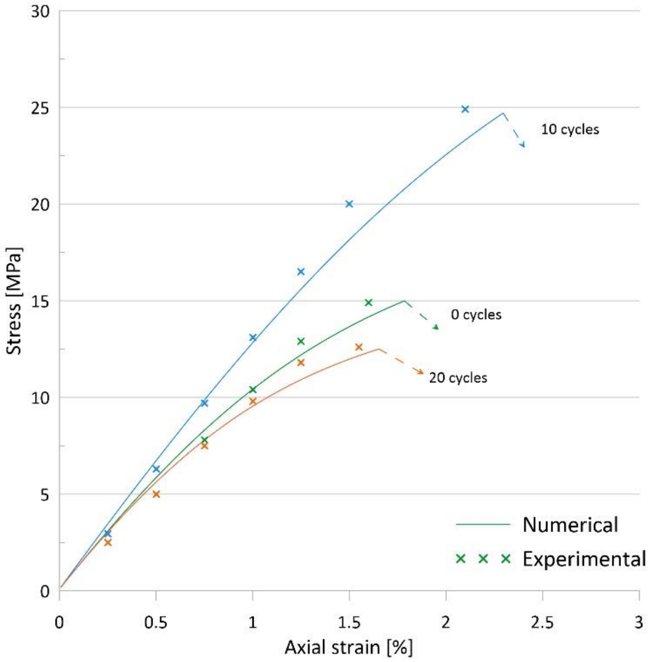

Fig. 25. Simulations of axial compression tests at different stages of the exposure to contamination.

The subsequent figures, i.e. Figs. 26-27, provide the results of numerical analysis incorporating the evolution laws (3). The analysis deals with the mechanical equivalent of a series of creep tests. The strength characteristics, $\phi = \phi(S_c)$ and $c = c(S_c)$, have been approximated here using the second-degree polynomials, as shown in Fig. 26, for which the coefficients of approximation are

$$b_1 = 0.90,\ b_2 = -1.38,\ c_1 = 2.31,\ c_2 = -3.27$$

Apparently, the quadratic form is not very accurate and higher order terms are, in general, required. The latter, however, is not feasible here in view of a limited experimental data. Note that the third-order approximation is physically not admissible as in this case eq. (3) is not a monotonically increasing function prior to the onset of degradation.

In the current example, a brick specimen, with initial concentration of precipitated salt of S_c=0.35, was loaded up to a prescribed stress intensity (10, 15 and 20 MPa, respectively) and subsequently experienced a progressive increase in salt contamination under a sustained axial load. The example is heuristic in nature as no specific time-history of salt transport is followed, it gives however an insight into the mechanical effects of crystallization. As seen from Fig. 27a, the sample at axial stress of 20 MPa experienced a localized failure ($\eta \rightarrow \eta_f$) at S_c of approx. 0.54, i.e. soon after the imposed increase in the volume fraction of precipitated salt. The loss of stability was triggered by a time-dependent degradation of strength properties as stipulated by the quadratic approximation employed (viz. Fig. 26). A qualitatively similar response can be observed for sample tested at axial stress of 15 MPa; however, the onset of failure occurs now at a higher value of S_c (approx. 0.68). Clearly, by lowering the creep stress intensity further (cf. 10MPa), the loss of stability is delayed beyond S_c=0.7.

Fig. 27b shows the evolution of the yield/ failure surfaces resulting from the salt contamination at the constant axial load of 15 MPa. The stress state is located on the yield surface, which is initially inside the domain enclosed by the failure envelope. As the volume fraction of crystallized salt S_c increases, the values of strength parameters decrease. As a result, both the yield and the failure surfaces evolve, with the latter gradually approaching the current stress state. At the onset of localization, the stress state remains on the updated yield surface which now overlaps with the degraded failure envelope. The evolution of both surfaces is accompanied by generation of irreversible (plastic) deformation that stems from the second term in the constitutive relation (13).

The examples given here, although very preliminary, provide some degree of confidence in the ability of this approach to describe the qualitative trends in the response of masonry materials to the continuing salt contamination process.

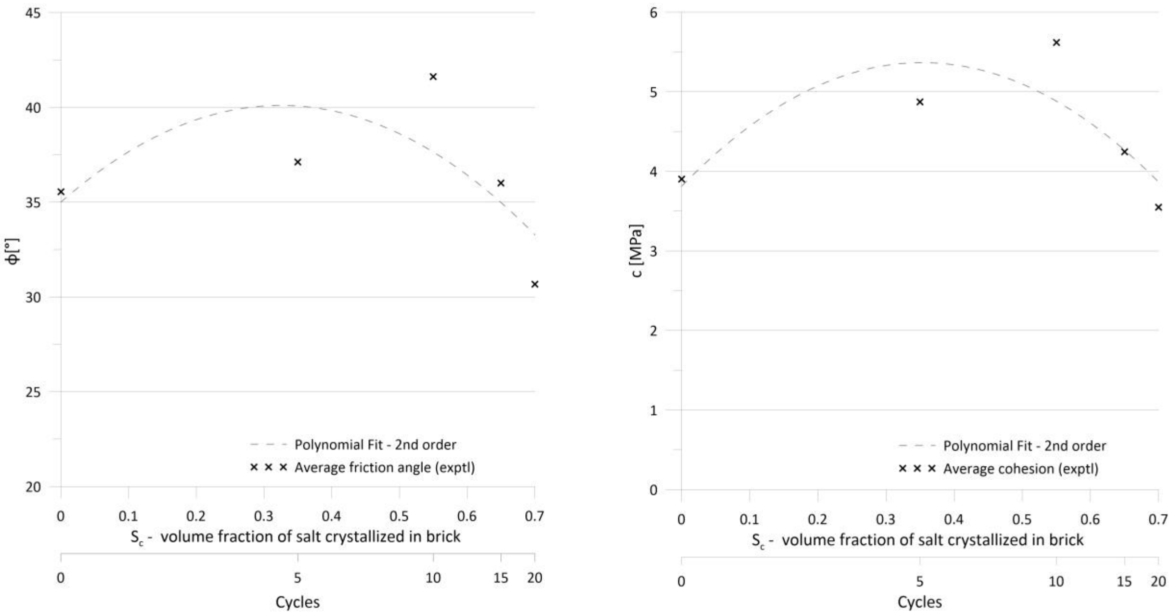

Fig. 26. Evolution of strength parameters with volume fraction of precipitated salt; quadratic approximation based on eq.(3).

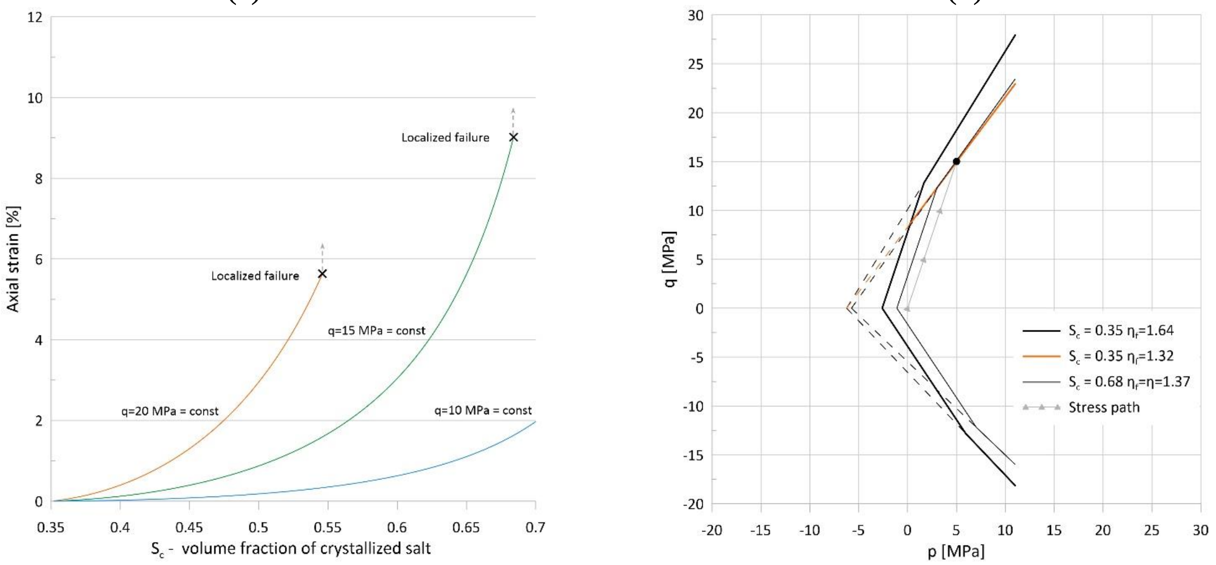

Fig. 27. (a) Build up of axial strain with increase in salt contamination at a constant axial load of q=10, 15 and 20 MPa; (b) the corresponding evolution of the yield/ failure surfaces at axial load of 15 MPa.

5. Final remarks

In the work reported here, a comprehensive experimental program has been carried out examining the impact of salt crystallization on the evolution of mechanical properties of the components of structural masonry. The tests were conducted on samples of ceramic bricks, cement mortar and samples containing the brick-mortar interface, all contaminated with aqueous solution of magnesium sulfate. This salt has a high ability to fill pores during exposure and is aggressive, which triggers a visible degradation of mechanical properties. Apparently, other types of salts could have been used. This, however, would likely have no direct impact on the primary qualitative findings; in particular, the functional form of the failure criteria and the nature of the governing constitutive relations.

The material properties were assessed after every 5 consecutive cycles of saturation in $MgSO_4$ solution and drying. The scope of investigation included specification of physical properties (viz. density of solids, pore size distribution), microstructural imaging and mechanical testing. The latter included axial compression, axial tension and triaxial compression on brick as well as mortar samples, together with the direct shear and axial tension tests on the brick-mortar bond. The primary objective was to propose and justify (based on the provided experimental evidence) a set of inelastic constitutive relations accounting for salt crystallization process. In that sense, the mechanical component was central in this pursuit.

For both brick and mortar, the conditions at failure at the continuum level were approximated using the the Mohr-Coulomb representation with Rankine's cut-off in the tensile regime. The functional form of these criteria incorporated evolution laws which related the basic strength parameters to the degree of pore saturation with precipitated salt (i.e. volume of crystallized salt per volume of voids). The kinetics of interaction was described by a polynomial form and the coefficients of approximation were identified through an appropriate interpretation of the experimental data in the 'triaxial' (p, q) space. It was demonstrated that, in case of $MgSO_4$, the third-order polynomial gave a fairly accurate representation of the evolution of friction angle and cohesion. The authors believe that for other types of salts the basic trends, as depicted in Figs. 13 and 20, would be similar, so that the functional form (3) will be adequate. However, the quantitative aspects will be affected. In particular, for some salt systems the enhancement of strength at early stages of crystallization may be marginal and the rate of degradation may also be less pronounced.

For the brick-mortar bond, the failure criterion was formulated in terms of the components of the traction vector acting along the interface. Again, the Coulomb representation with Rankine's cut-off was employed and the strength parameters were correlated with the volume fraction of salt crystallized within the region adjacent to the interface. As mentioned earlier, the specification of S_c within the interface whose thickness is infinitesimal, poses difficulties. Therefore, in actual engineering applications, it may be simpler to phrase the evolution laws in terms of volume fraction of salt precipitated in the brick material alone (cf. Fig.22). This is particularly relevant in the context of formulations that employ a constitutive law with embedded discontinuity (cf. refs. [47-48]). In this case, the brick-mortar interface, which represents the weakest link in the masonry panel, is perceived as being embedded in the adjacent intact medium (i.e. bricks).

The experimental component of this research has been supplemented by a numerical study that examined the implications of incorporating the evolutions laws in the functional form of the failure criteria. In particular, an elastoplastic formulation has been discussed, in which the yield function was assumed to depend on the accumulated plastic distortions as well as the volume fraction of crystallized salt. In this case, the consistency condition led to an additional time-dependent term appearing in the enhanced form of the constitutive relation. The framework was illustrated by some simple numerical examples assessing the mechanical response under sustained load in the presence of continuing salt contamination process. It is noted, however, that the analysis of the impact of salt crystallization in actual masonry structures requires, in addition to specification of mechanical laws, a proper coupled hydro-thermo-mechanical analysis that accounts for the transport of water and salt in the form of gas, solid and liquid, as well as the phase transition between them.

References

1. A.E. Charola, C. Blauer, Salts in masonry: an overview of the problem, RBM 21 (2015) 119-135.
2. P.C. Hewlett, Lea's chemistry of cement and concrete, Butterworth-Heinemann, 4th ed. Oxford, 1998.
3. A. Arnold, Determination of mineral salts from monuments, Stud. Conserv. 29 (1984) 129-138.

4. A. Zalooli, M. Khamehchiyan, M. R. Nikudel, Durability assessment of Gerdoi and red travertines from Azarshahr, East Azerbaijan province, Iran, Bull. Eng. Geol. Environ. 78 (2019) 1683-1695.
5. O.J. Coussy, Deformation and stress from in-pore drying-induced crystallization of salt, J. Mech. Phys. Solids 54 (2006) 1517-1547.
6. M. Steiger, Crystal growth in porous materials – I: The crystallization pressure of large crystals, J. Cryst. Growth 282 (2005) 455-469.
7. G.W. Scherer, Stress from crystallization of salt, Cem. Concr. Res. 29(2004) 1613-1624
8. L.A. Rijners, H.P. Huinink, L. Pel, K. Kopinga, Experimental evidence of crystallization pressure inside porous media, Phys. Rev. Lett. 94 (2005) 075503.
9. D. Yang, J. Luo, The damage of concrete under flexural loading and salt solution, Constr. Building Mat. 36 (2012) 129-134.
10. C. Gentilini, E. Franzoni, S. Bandini, L. Nobile, Effect of salt crystallization on the shear behaviour of masonry walls: An experimental study, Constr. Building Mat. 37 (2012) 181-189.
11. B. Lubelli, R. Van Hees, C. Groot, The role of sea salt in the occurrence of different damage mechanisms and decay patterns on brick masonry, Constr. Building Mat. 18 (2004) 119-124.
12. S. Yu, C.T. Oguchi, Role of pore size distribution in salt uptake, damage, and predicting salt susceptibility of eight types of Japanese building stones, Eng. Geol. 115 (2010) 1757-1773.
13. M. Angeli, J.P. Bigas, D. Banavente, R. Hebert, C. David, Salt crystallization in pores: quantification and estimation of damage, Environ. Geol. 52 (2007) 205-213.
14. R.M. Espinosa, L. Franke, G. Deckelmann, Phase changes of salts in porous materials: crystallization, hydration and deliquescence, Constr. Building Mat. 22 (2008) 181-189.
15. J.R. Flatt, Salt damage in porous materials: how high supersaturations are generated, J. Cryst. Growth 242 (2002) 435–454.
16. M. Steiger, Crystal growth in porous materials. II: Influence of crystal size on the crystallization pressure, J. Cryst. Growth. 282 (2005) 470–481.

17. R.M. Espinosa-Marzal, G.W. Scherer, Advances in understanding damage by salt crystallization, Acc. Chem. Res. 43(2010) 897-905.
18. A.E. Charola, Salts in the deterioration of porous materials: An overview, J. Amer. Inst. Conservat. 39 (2000) 327-343.
19. L. Grementieri, Modeling and analysis of mechanical effects induced by salt crystallization in porous building materials: A two-scale approach, Ph.D. Dissertation, University of Bologna (2017).
20. J. Desarnaud, H. Derluyn, L. Molari, D. de Miranda, V. Cnudde, N. Shahidzaheh, Drying of salt contaminated porous media: Effect of primary and secondary contamination, J. Appl. Phys. 118(2015) 114901.
21. J. Desarnaud, F. Bertrand, N. Shahidzaheh-Bonn, Impact of the kinetics of salt crystallization on stone damage during rewetting/drying and humidity cycling, J. Appl. Mech. 80 (2013) 020911.
22. H. Derulyn, Salt transport and crystallization in porous limestone: neutron-X-ray imaging and poromechanical modeling, Ph.D. Dissertation, ETH Zurich (2012).
23. G.F. Andriani, N. Walsh, The effects of wetting and drying and marine salt crystallization on calcarenite rocks used as building material in historic monuments, Golog. Soc, London Special Publ. 271 (2007) 179-188.
24. Q. Sun, Y. Zhang, Combined effects of salt, cyclic wetting and drying cycles on the physical and mechanical properties of sandstone, Eng. Geol. 248 (2019) 70-79.
25. T. Stryszewska, M. Dudek. Selection of method of chemical analysis in measuring the salinity of mineral materials, Materials 13 (2020) 559.
26. M.Y. Celik, A. Aygun, The effect of salt crystallization on degradation of volcanic building stones by sodium sulfates and sodium chlorides, Bull. Eng. Geol. Environ. 78 (2019) 3509-3529.
27. C. Gentilini, A.M. D’Altri, M. Amato, P. Zanotti, F. Favaro, S. de Miranda, Salt attack effects on the shear behaviour of masonry: preliminary results of an experimental campaign, Key Eng. Mat. 747 (2017) 512-517.

28. E. Franzoni, C. Gentilini, G. Graziani, S. Bandini, Towards the assessment of shear behaviour of masonry in on-site conditions: A study on dry and salt/water conditioned brick masonry triplets, Constr. Building Mat. 65 (2014) 405-416.
29. G. Cardani, M.R. Valluzzi, M. Panizza, P. Girardello, L. Binda, Influence of salt crystallization on composites-to-masonry bond evaluated on site by pull-off tests, Key Eng. Mat. 624 (2014) 338-345.
30. E.I. Nadelman, K.E. Kurtis, The durability of Portland-limestone cement-based materials to physical salt attack, Cem. Concr. Res. 125 (2019) 105859.
31. D. Ergenç, J. Feijoo, Rafael Fort, Mónica Alvarez de Buergo. Effects of potassium ferrocyanide used for desalination on lime composite performances in different curing regimes, Constr. Building Mat. 259 (2020) 120409.
32. M. Bassi, E. Sassoni, E. Franzoni, Experimental Study on an Innovative Biopolymeric Treatment Against Salt Deterioration of Materials in Cultural Heritage. Front. Mater. 8 (2021) 583112.
33. R.W. Lewis, B.A. Schrefler, The finite element method in the static and dynamic deformation and consolidation of porous media, Wiley, Chichester, 1998.
34. T. Krejci, J. Kruis, M. Sejnoha, T. Koudelka, Numerical analysis of coupled heat and moisture transport in masonry, Comput. Math. with Appl. 74 (2017) 229-248.
35. G. Castellazzi, S. de Miranda, G. Formica, L. Molari, F. Ubertini, Coupled hygro-mechanical multiscale analysis of masonry walls, Eng. Struct. 84 (2015) 266-278.
36. F. Tariku, K. Kumaran, P. Fazio, Transient model for coupled heat, air and moisture transfer through multilayered porous media, Int. J. Heat Mass Transf. 53 (2010) 3035-3044.
37. G. Castellazzi, A D'Altri, S. de Miranda, H. Emami, L. Molari, F. Ubertini, A staggered multiphysics framework for salt crystallization-induced damage in porous building materials. Constr. Building Mat. 304 (2021) 124486.
38. H. Derluyn, P. Moonen J. Carmeliet, Deformation and damage due to drying-induced salt crystallization in porous limestone, J. Mech. Phys. Solids 63 (2014) 242-255.

39. M. Koniorczyk, D. Gawin, Numerical modeling of salt transport and precipitation in non-isothermal partially saturated porous media considering kinetics of salt phase changes, Transp. Porous Med. 87 (2011) 57-76.

40. A. Nicoli, Modeling and numerical simulation of salt transport and phase transition in unsaturated porous materials, Ph.D. Dissertation, Syracuse University, ProQuest Dissertation Publishing (2008) 3323075.

41. S. Pietruszczak, Fundamentals of plasticity in Geomechanics, CRC Press/Balkema, Leiden/London/ New York, 2010.

42. S. Yu, C.T. Oguchi, Role of pore size distribution in salt uptake, damage, and predicting salt susceptibility of eight types of Japanese building stones, Eng. Geol. 3 (2010) 226-236.

43. C. Rodriguez-Navarro, E. Doehne, Salt weathering: Influence of evaporation rate, supersaturation and crystallization pattern, Earth Surf. Process. Landf. 24 (1999) 191–209.

44. A. Zalooli, M. Khamehchiyan, M.R. Nikudel, D.M. Freire-Lista, R. Fort, S. Ghasemi, Artificial microcracking of granites subjected to salt crystallization aging test, Bull. Eng. Geol. Environ. 79 (2020) 5499-5515.

45. P. López-Arce, M.J. Varas-Muriel, B. Fernández-Revuelta, M.Á. De Buergo, R. Fort, C. Pérez-Soba, Artificial weathering of Spanish granites subjected to salt crystallization tests: surface roughness quantification, Catena 83 (2010) 170-185.

46. J.W. Rudnicki, J.R. Rice, Conditions for the localization of deformation in pressure-sensitive dilatant materials, J. Mech. Phys. Solids 23 (1975) 371-394.

47. S. Pietruszczak, On homogeneous and localized deformation in water-infiltrated soils, Int. J. Damage Mech. 8 (1999) 233-253.

48. K. Koocheki, S. Pietruszczak, E. Haghighat, A computational framework for meso and macroscale analysis of structural masonry, Int. J. Solids Struct. 236-237 (2022) 111342.

Chapter 5

Conclusions and future work

This chapter provides some final remarks on the conducted research and suggestions for potential future work. Given the format of this thesis, some overlap with the introductory sections and the articles included in Chapters 2-4 is unavoidable. Since the papers also incorporate detailed discussion regarding the advantages and limitations of the proposed methodologies, the present chapter deals with a broader overview of the current work.

This thesis was focused on development and implementation of constitutive relations that describe the mechanical and hydraulic response of cohesive-frictional materials, both naturally occurring (sedimentary and crystalline rocks) as well as construction materials (i.e., components of structural masonry). The scope of research was broad and interdisciplinary, as it dealt with the notions of anisotropy, presence of discontinuities, fracture sealing/healing, and the chemical degradation of properties triggered by salt crystallization. The primary areas of application of this work include Civil as well as Environmental Engineering.

Chapter 2 was devoted to modelling of mechanical response of sedimentary rocks, i.e. Carpathian flysch. The geological structure of this flysch makes it very susceptible to landslides. Therefore, the conducted research is particularly relevant to assessment of stability of slopes and underground structures (e.g., tunnels) that are constructed in this rock formation. The primary difficulty in estimating the conditions at failure is the fact that the strength properties depend not only on the orientation of bedding planes but also on the volume fractions of constituents. The latter involve alternating marine deposits of claystone and sandstones with varying thickness. Evidently, conducting a large-scale tests on this type of rock formation is not feasible. Therefore, the proposed methodology was based on generating the data through a set of numerical simulations at the mesoscale, which require only the information on the properties of constituents. The latter are isotropic within themselves, so that they can be identified directly from standard material tests.

The formulation proposed in this work employed a similar functional form of failure criteria at both meso and macroscales, the latter enhanced by incorporating the effects of anisotropy as well as the volume fraction of constituents. The mesoscale FE simulations were based on an incremental elastic-perfectly plastic analysis. In this case, an alternative way to assess the ultimate load would be to invoke the finite element limit analysis. Both these approaches, however, have limitations as they do not account for the onset and propagation of localized failure which may occur in both compression and tension regimes.

It should also be pointed out that the proposed methodology is fairly general and can be applied to other multi-layered composites. The present work, however, incorporates an assumption of a perfect bonding between the constituents. Although in case of flysch the interfacial properties do not play a critical role in the evolution of damage, for some composites made from two or more constituents with significantly different physical properties, delamination may be the primary failure mechanism and needs to be considered.

Further research in this area needs to focus on a more comprehensive assessment of accuracy of the proposed criterion and its implementation to analysis of practical geotechnical problems. This requires development of a constitutive relation that will address the evolution of deformation process at the macroscale. While in tension regime, the behaviour may be considered as elastic- brittle, in compression range an inelastic framework should be employed. In both cases, the notion of the onset and propagation of localized damage needs to be accounted for.

Chapter 3 dealt primarily with crystalline rocks which contain naturally occurring faults/fractures. The presence of these discontinuities significantly affects both the hydraulic and mechanical properties at the macroscale. Fractures are the predominant pathways for fluid, so that the flow is largely governed by the geometry of fracture network, i,e, orientation and spacing of individual fractures, and their connectivity. Similarly, the deformation mechanism at the macroscale is governed the process of localized deformation associated with the presence of fractures. In this context, an important issue is that associated with the process of self-sealing and self-healing of fractures. The intrinsic self-sealing occurs in majority of fluid-conductive rock fractures. The self-healing mechanisms, on the other hand, are typical of cementitious materials but are also present in various rock formations. Example here is a rock salt, where nearly 80% of original strength can be regained through creep of asperities.

The work reported in this thesis involved development of a general mathematical framework for the description of crack sealing/healing processes. The approach employed a constitutive law with embedded discontinuity that incorporates an internal scale parameter, which prevents a systemic sensitivity of the solution to the details of FE discretization. The kinetics of the process was defined by invoking a scalar parameter whose evolution is time-dependent and may be affected by various external agencies, such as temperature and chemical/biological environment. Apparently, the specification of this evolution law requires a micromechanical insight into the specific form of physicochemical interaction, which was beyond the scope of this work.

The self-healing process was described by employing a hypoelastic-plastic framework for the fractured zone in which the mechanical properties evolve in the course of chemo-mechanical interaction. Both, the elastic properties and the functional form of yield and plastic potential functions were assumed to be affected by the ongoing self-healing and the respective criteria governing an active loading /unloading process were formulated. The upscaling to the level of a referential volume was performed by invoking an embedded discontinuity approach. The effect of self-healing was embedded in the evolution law for the hydraulic properties within the fracture region. The proposed approach incorporated a spectral decomposition of the fracture transmissivity operator and related its evolution to the variable governing the kinetics of the process.

It should be noted that the research outlined in this chapter was largely preliminary and focused on proposing a general methodology for describing the mechanical/hydraulic effects of self-healing and self-sealing processes. The illustrative examples were largely heuristic and did not involve the coupled conditions. In this context, the future work should deal with two major aspects. The first one, is the quantification of the evolution law for the kinetic of the self-healing/sealing process which, as mentioned earlier, must be focused on a specific mechanism, and involve the micromechanical considerations. The other aspect is the incorporation of the framework that explicitly describes the hydro-mechanical coupling and its implementation in a boundary value problem that could serve as a benchmark.

Chapter 4 was devoted to the issue of degradation of mechanical properties in construction materials experiencing an environmental damage. The main focus was on *structural masonry* and its individual components subjected to an ongoing process of crystallization of salt within the pores (i.e., subflorescence). Salt crystallization is a major cause of structural damage in existing structures including the historic monuments. In recent years considerable advances have been made in explaining the fundamental mechanisms responsible for salt damage. As a result, new methods of treatment have been proposed that address the cause of the problem rather than dealing with the symptoms. Even though the progress is evident, many challenges still remain, particularly in understanding complex interactions between salts and the mechanism of crack initiation and growth. Also, there has been no attempt to explicitly couple the phenomenon of salt transport and crystallization with reliable constitutive relations that describe the evolution of damage at the continuum level.

The main focus in this thesis was on performing a carefully designed experimental program which allowed an explicit identification of the evolution laws governing the conditions at failure in individual components of masonry, i.e. brick material, mortar and the brick-mortar bond. The scope of this investigation was quite broad, as it included physical and microstructural measurements in addition to a series of mechanical tests, the latter including axial compression/tension, triaxial compression as well as direct shear tests on samples at different stages of contamination with magnesium sulfate. Overall, over 150 samples were prepared and tested. A unique feature of this investigation was an attempt to formulate and quantify the evolution laws relating the primary strength variables to the volume fraction of salt crystallized within the pore space.

The kinetics of interaction was described by a polynomial form and the coefficients of approximation were identified through an appropriate interpretation of the experimental data in the 'triaxial' space. It was demonstrated that, in case of $MgSO_4$, the third-order polynomial gave a fairly accurate representation of the time-dependent variation of key strength parameters. In addition to these studies, the evolution laws for degradation of stiffness and continuing dilation with the number of contamination cycles were also formulated.

Finally, the work examined the implications of incorporating the proposed evolution laws in the formulation of governing constitutive relations. In particular, an elastoplastic strain-hardening framework was outlined incorporating the volume fraction of crystallized salt as in independent parameter. In this case, the consistency condition led to an additional time-dependent term appearing in the enhanced form of the constitutive law. Again, some heuristic numerical examples were provided examining the response under sustain load in the presence of ongoing subflorescence.

Apparently, the assessment of impact of salt crystallization in actual masonry structures requires, in addition to specification of mechanical laws, a proper coupled hydro-thermo-mechanical analysis. This is quite challenging, as such an analysis should account for the transport of water and salt in the form of gas, solid and liquid, as well as the phase transition between them. Thus, the follow-up research needs to focus on this specific aspect.

In summary, it needs to be pointed out again that the main conceptual contributions in this thesis are contained in Chapters 2-4. The study presented in Chapter 2 incorporates the functional form of an anisotropic failure criterion developed in earlier work (i.e. ref. [19] of Chapter 2). This criterion was extended here to incorporate the effect of volume fraction of constituents. In addition, a novel procedure for identification of approximation coefficients describing the spatial distribution of strength parameters in relation to microstructure orientation, has been proposed. The constitutive relations developed in Chapter 3 represent an original approach that has not been published previously. This pertains to the mathematical description of both self-sealing and self-healing process. Finally, in Chapter 4, an original and comprehensive experimental program was conducted that allowed to formulate the evolution laws governing the conditions at failure in all primary constituents of masonry (including the brick-mortar bond) during the salt crystallization process. These evolution laws were integrated with a new plasticity formulation that incorporated the degree of pore saturation with precipitated salt as an additional internal variable.

Appendix: Authors' statement

Article #1: On specification of conditions at failure in interbedded sedimentary rock mass (P. Przecherski and S. Pietruszczak)

I confirm the details of collaboration as stated in section on 'Co-Authorship' (p.6)

Article #2: On hydro-mechanical response of self-healing and self-sealing fractured geomaterials (S. Pietruszczak and P. Przecherski)

I confirm the details of collaboration as stated in section on 'Co-Authorship' (p.6)

Article #3: Impact of salt crystallization on the mechanical properties of structural masonry: an experimental and numerical study (S. Pietruszczak, P. Przecherski and T. Stryszewska)

I confirm the details of collaboration as stated in section on 'Co-Authorship' (p.6)